DEPARTAMENTO DE FÍSICA APLICADA
UNIVERSIDAD AUTÓNOMA DE MADRID

D O C T O R A L T H E S I S

New Trends in Cement Systems: Interface with TiN Thin Films and Modification with Titania Nanoparticles

Thesis submitted by **Elena Cerro Prada**

to obtain the degree of

Doctor in Physics

from the Universidad Autónoma de Madrid

Madrid, January 2013

Acknowledgements

El presente trabajo de investigación ha sido realizado en el Departamento de Física Aplicada de la Universidad Autónoma de Madrid, bajo la dirección de los Profesores Dr. Miguel Manso Silván y Dr. Vicente Torres Costa.

Quiero expresar mi más sincero agradecimiento a los Profesores Dr. Miguel Manso Silván y Dr. Vicente Torres Costa por las enseñanzas, consejos y entusiasmo durante todo el proceso de elaboración de esta Tesis. Gracias Miguel y Vicente; no tengo palabras para expresaros mi inmensa gratitud por vuestro increíble apoyo; gracias por creer en mi y por animarme a seguir, especialmente en los momentos más difíciles.

Quiero expresar mi agradecimiento de forma muy especial al Profesor Honorario del Departamento de Física Aplicada de la Universidad Autónoma de Madrid, Dr. José Manuel Martínez-Duart, por su inestimable consejo y entusiasmo, por acogerme en su grupo de Investigación, por su cariñoso apoyo. Gracias, José Manuel. Gracias también a mis compañeros del laboratorio del departamento de Física Aplicada de la Facultad de Ciencias de la UAM, Dario, Elena, Luís, Jacobo, Gonzalo, Esther.. por llenar mis estancias en el laboratorio con momentos divertidos y con caramelos, siempre a mano, para endulzar las interminables tomas de datos.

Mi agradecimiento también al Catedrático de Física de la Escuela de Obras Públicas de la Universidad Politécnica de Madrid, el Dr. Luis B. López Vázquez, por haberme animado a emprender este trabajo. También quiero mencionar a mis compañeros de la Escuela de Ingeniería Técnica de Obra Públicas, no los nombro porque son muchos y no quisiera dejarme a nadie, gracias a todos ellos por interesarse por mi progreso y animarme cada día. Pero sobretodo quiero nombrar, con especial cariño, a mis queridas Charo y Rosa; por guiar mi camino tantas veces y por vuestro maravilloso apoyo, nunca podré agradeceros suficiente lo que habéis hecho por mi.

Esta tesis no habría sido posible sin la colaboración de muchas personas que, dedicándome parte de su tiempo, han colaborado con sus enseñanzas y experiencia en

muchos de los aspectos desarrollados en este trabajo. Nombro especialmente a la Dra. Pilar Herrero por su inestimable colaboración en los estudios de microscopía TEM que, gracias a ella, han supuesto una parte importante de esta investigación. Gracias, querida Pilar. Y por supuesto gracias querido Jesús, por esos momentos tan agradables durante los exámenes con el SEM, ha sido un honor contar con tu inestimable ayuda.

Mi especial agradecimiento a aquellas personas que, conscientemente, han dedicado parte de su tiempo a comprenderme, ayudarme, hacerme sentir bien, preocuparse por mi y, sobretodo, a hacerme sonreir; porque han contribuido a hacerme feliz y a enfrentarme con fuerza al trabajo diario. Mis queridas amigas Maria Jesús, Julia, Ana, Antonia, Eva V, Eva M, Macarena, Carmen, Eva B... gracias a todas por vuestra amistad, por formar parte de mi vida, por vuestra confianza y vuestro cariño. En este párrafo también estás tú, querido Dario, gracias.

Thank you, my dear friend Ian, for you amazing support during the worst moments, even being thousand kilometers apart, it looked like you have been by my side in every second. Thank you for proof-reading this thesis, and for all those comments... but over all thank you for being my friend. Thank you so much, dearest Ian.

Y qué voy a decir de mi fantástica familia, no podría ser más afortunada por tenerles a todos ellos..... mi magnífico padre, y mi querida madre... que nos dejó para siempre antes de que yo emprediera este camino; te echo de menos, Mamá, nunca dejarás de estar en mi corazón. Gracias a mis hermamos y hermanas, a todos gracias por quererme y apoyarme hasta la saciedad.

Y sobretodo... SOBRETODO gracias a mis dos hijas, Irene y Lidia: sois lo más importante de mi vida, el apoyo más incondicional que jamás he tenido y que siempre tendré, lo sé. Ha sido muy complicado compaginar este trabajo con mi dedicación a vosotras, mis adoradas nenas, pero sabéis tan bien como yo que ha merecido la pena todo el esfuerzo. Irene y Lidia: sois mi vida.

A mi querida madre

The most beautiful thing we can experience is the mysterious.

It is the source of all true art and all science.

He to whom this emotion is a stranger,

who can no longer pause to wonder and stand rapt in awe,

is as good as dead: his eyes are closed.

Albert Einstein (1879-1955)

Abstract

This doctoral thesis has two objetives: the first investigation is dedicated to the evaluation of TiN thin films as a protection barrier against corrosion of reinforced steel in concrete. To achieve this goal, TiN thin films were prepared by using the magnetron sputtering deposition method. Characterization of the TiN-cement interface was performed by advanced experimental techniques such a XRD, XPS, TGA/TG, SEM and HRTEM. The corrosion parameters of the TiN were studied and its dependence on the cement phases was analysed. The cement paste nanostructure at the interface was investigated focusing on the so-formed C-S-H gel. The interface TiN/cement has shown excellent corrosion resistance against chloride ingress. The cement paste in contact with TiN develops adhesion phases which enrich the passive layer and therefore provide further protection to the whole structure.

Secondly, we aim to evaluate the feasibility of the application of heterogeneous photocatalysis for the elimination of pollulants from air by modifying cement paste nanostructure with TiO_2 nanoparticles prepared by sol-gel. In this work, TiO_2 nanoparticles were was synthesized by using the sol-gel technology and inserted in the cement paste matrix from the first stage of hydration. Characterization of the prepared TiO_2-modified cement was performed. The photocatalytic activity and its dependence on the TiO_2 concentration was studied. The cement paste nanostructure after modification was analysed in order to understand the properties of the new material. The results show that TiO_2 provide the cement system not only with photocatalytic activity but also promote the formation of C-S-H gel, which is, ultimately, the phase responsible for the mechanical performance of cement-based construction materials.

Keywords: Cement Paste Microstructure, Nanotechnology in Cement Systems, TiN anticorrosion films, TiO_2 induced Photocatalytic

Resumen

Esta tesis doctoral tiene dos objetivos: una primera investigación se ocupa de evaluar la utilización de láminas delgadas de TiN como barreras físicas de protección contra los procesos de corrosión, via cloruros, de las armaduras de hormigón armado. Para ello, láminas delgadas de TiN han sido preparadas mediante deposición por pulverización catódica reactiva. La interfaz entre TiN y la pasta de cemento ha sido caracterizada, tanto en la intercara cemento como en la intercara TiN, mediante las siguientes técnicas experimentales avanzadas: XRD, TGA/TG, XPS, SEM y HRTEM. Los parámetros de corrosión de las láminas de TiN se han estudiado, así como su dependencia con las fases de cemento formadas en la interfaz. Los resultados han demostrado que la interfaz TiN/cemento posee excelente resistencia a la corrosión. Elcemento hidratado en la interfaz forma fases de adhesión que favorecen la formación de la capa pasiva, y por tanto proporcionan protección físico/química ante la presencia de cloruros corrosivos.

La segunda investigación versa en la aplicación de la fotocatálisis heterogénea para la eliminación de contaminantes atmosféricos, a partir de la modificación de la nanoestructura de la pasta de cemento con nanopartículas de TiO_2 sintetizadas por sol-gel. Nanopartículas de TiO_2 han sido preparadas mediante sol-gel e insertadas en la pasta de cemento a través del agua de hidratación. El sistema TiO_2/cemento ha sido caracterizado con XRD, TGA/TG y SEM. La actividad fotocatalítica y su dependencia con la concentración de TiO_2 ha sido estudiada. Los resultados han demostrado que nanopartículas de TiO_2 embebidas en la matriz de cemento, no sólo proporcionan propiedades fotocatalíticas al sistema, sino además inducen la formación de gel C-S-H el cual, en última instancia, es el responsable de las propiedades estructurales de los materiales de construcción con base cemento.

Palabras clave: Microestructura de la pasta de cemento, nanotecnología en materiales base cemento, anticorrosión con láminas delgadas de TiN, fotocatálisis inducida por TiO_2

Table of Contents

List of Figures

List of Tables

CHAPTER 1

Introduction

1.1 Brief Historical Preamble

Researching on materials science is part of a continuum stretching back to the beginnings of human life on earth. The urge to innovate - to seek improvements in our material environment, to profit from those improvements, and most importantly: to survive - have their origins thousands of years ago. Early humans were by necessity materials explorers, constantly testing and improving upon what they found at hand.

Cement is one of the world most ancient materials. We have inherited it from ancient times and without it our present civilization would truly not be the same. The remarkable properties of cement are evidenced in the Roman brickwork: the surprinsing hardness of the mortar in walls of Roman Coliseum has puzzled many engineers, and has sometimes led to the assumption that some secret was possessed by the workmen which is now lost. However, a comparison of the analysis of the mortar with the descriptions of the method by ancient authors gives no ground for such a supposition.

During the Middle Ages, the art of preparing mortar was lost, and it was not until the scientific spirit of inquiry revived, that the secret of hydraulic cement - cement that will harden under water - was rediscovered. In 1756, repeated structural failure of the Eddystone Lighthouse off the coast of Cornwall, England, led John Smeaton, a British engineer, to conduct experiments with mortars in both fresh and salt water. These tests led to the discovery that cement made from limestone containing a considerable proportion of clay would harden under water. Making use of this discovery, he

rebuilt the Eddystone Lighthouse in 1759. It stood for 126 years before replacement was necessary.

Before Portland cement was discovered and for some years after its discovery, large quantities of natural cement were used. Natural cement was produced by burning a naturally occurring mixture of lime and clay. Because the ingredients of natural cement were mixed by nature, its properties varied as widely as the natural resources from which it was made. In 1824, Joseph Aspdin, a bricklayer from Leeds, England, patented a way of making a hydraulic cement which he called *Portland* cement because, once set, it had a colour similar to the white-grey limestone found on the Isle of Portland in Dorset, England. Aspdin's method, still in use today, consists of the careful preparation of calcareous (limestone) and clayey materials, composed mainly of calcium, silicon, iron and aliminium. Once mixed, the minerals are finely ground, sprayed with water and baked to temperatures of up to 1,450°C. At these temperatures, the minerals melt and their constituents undergo phase changes, resulting in the formation of new chemical compounds.

The result of the calcination, called *clinker*, is quickly stabilized by cooling and is then mixed with a certain amount of calcium sulphate (*gypsum*), along with other additional components depending on the type of cement being produced. In this way, a fine powder (with nodules never exceeding 45 μm in diameter) is obtained. Today, nearly 200 years after its discovery, there are about 1,500 cement factories around the world producing Portland cement. In 2010, more than 61 million tons of cement were produced worldwide (from U.S. Geological Survey, Mineral Commodity Summaries, January 2011).

1.2 Cement System

1.2.1 Clinker: the anhidrous material

Even though the practice of using cement-like materials dates back thousands of years, the understanding of cement's chemical and physical properties - from the study and investigation of its microstructure - is relatively recent. Portland cement is a complex system made up of a series of impure chemical compounds that come mainly from clinker: the result of the process of *clinkerisation* (calcination at temperatures of around 1,450°C, cooling and subsequent grinding) of primary materials such as limestones, clays and iron oxides. The primary chemical phases that compose Portland cement are CaO, SiO_2, Al_2O_3, Fe_2O_3, besides SO_3 - from gypsum - and some small amounts of oxides, such as MgO, KO and Na_2O. During clinkering, these phases combine to form others that constitute cement. For example, calcium oxide and silicon dioxide combine to form a modified form of tricalcium silicate, also known as alite, which is the most important phase in cement. The other major phases present in cement are belite, aluminate and ferrite phases (Table 1.1). The phases are not present in their pure form and contain ionic substitutions in their crystalline structures. Calcium sulphate is added to the clinker before grinding. Although typically referred to as gypsum, other forms of calcium sulphate may also be used.

In 1915, the manufacture of Portland cement was standardized by the NBS, National Bureau of Standards (after 1988 known as the National Institute of Standards and Technology). This in turn gave impetus to further research on the microstructure of cement clinker and, with the publication of Le Chatelier's doctoral thesis in 1905, entitled *Experimental Researches on the Constitution of Hydraulic Mortars* [Chatelier 1905], led to the recognition of the four compounds shown in Table 1.1, as the four major constituents of Portland cement clinker. Almost twenty five years later, in 1929, Bogue established a standard methodology to calculate the theoretical abundance of phases present in the clinker of cement [Bogue 1929], assuming that the main constituents of

clinker are pure with specific compositions, and should therefore be present in proportion to the weight of the clinker, as shown in Table 1.1.

Table 1.1: Typical chemical composition of the clinker of Portland Cement [Mindess et Al., (2002), Taylor (1997)]

Name	**Chemical Formula**	**Shortened Formulation**	**Porcentage Weight**
Tricalcium silicate *alite*	$3CaOSiO_2$	C_3S	50-70
Dicalcium silicate *belite*	$2CaOSiO_2$	C_2S	15-30
Tricalcium aluminate	$3CaOAl_2O_3$	C_3A	5-10
Tetracalcium aluminoferrite	$4CaOAl_2O_3Fe_2O_3$	C_4AF	5-15
Calcium sulfate dehydrate *gypsum*	$CaSO_42H_2O$	CSH_2AF	4-6

Cement reacts with water in a process called *hydration*. During hydration, the clinker compounds readily react with water giving **insoluble hydration products** which, in a cement paste (a mixture of cement powder and water) or a concrete (a cement paste containing sand and aggregate filler), gradually replace the water in the spaces between the cement grains and aggregate particles. This eventually provides a matrix that effectively binds the composite mass together. The reaction products, called *hydrates*, are responsible for strength development and they give cement its binding properties. In the following sections, the hydration of cement, the development of its microstructure and its reaction kinetics are discussed in more detail.

1.2.2 Cement paste: the hydrated material

While the cement powder, clinker, is a material eager for water in that it reacts immediately with it to form the cement paste, this new hydrated material, once it has set, forms a compound with totally the opposite properties: the hardened cement does not react with water at all; and it is this propertie that explains the existence of various research lines on the cement microstructure: while numerous studies are based on the analysis of clinker, other works focus on the study of the hydrated constituents, or

cement paste. This thesis carries out an investigation of the hydrated material: cement paste formed by Portland cement powder and water. Therefore, the hydration process and the formation of hydrated products will be further discussed in the following section.

1.2.2.1 Hydration of Portland cement

Hydration of Portland cement is a sequence of overlapping chemical reactions between clinker constituents, calcium sulphate (gypsum) and water, leading to continuous cement paste stiffening and hardening. This *starching process* is a consequence of a change from a granular system in concentrated suspension to a viscoelastic skeletal solid capable of supporting applied stresses, at least for a short time, without significant deformation [Gartner 2002]. The subsequent decrease in porosity and formation of a complex elastic and brittle material is called *hardening* - a chemical-physical process which leads to the development of the ultimate mechanical properties. The hydration reactions proceed until inadequate amounts of reactants (cement components, water) and space to deposit the hydration products cause the reactions to cease.

The hardening reaction in cement paste is mainly associated with the hydration of the two calcium silicate compounds. In the anhydrous clinker of ordinary Portland cement, C_3S alite represents 50-55% of the total mass, and C_2S belite another 25-30%, which means that about 80% of the clinker mass are calcium silicates. These two phases produce the same products when reacting with water: on the one hand, a colloidal calcium silicate hydrate, also known as *C-S-H gel*, is formed, along with a solid solution crystalline of calcium hydroxide, $Ca(OH)_2$, or CH, also called *portlandite*.

Chemically, hydration is a complex dissolution-precipitation process in which the various hydration reactions proceed simultaneously at different rates influencing each other. The approach taken in this chapter is to provide an overview of the main reactions involved in the process, mainly those where alite and belite are involved. This choice is based on the previously highlighted fact that Portland cement clinker contains about

80% of alite and belite, providing both phases the bulk of the hydrated material: the C-S-H gel which constitutes about 70% of the cement paste and thus forms the main binding agent between the residual grains of cement and other crystalline products of hydration.

1.2.2.2 Hydration of alite and belite

Alite reacts with water producing calcium silicate hydrate (C-S-H) and calcium hydroxide (CH or portlandite), according to Equation (1.1):

$$C_3S + 5.3H \rightarrow C_{1.7}SH_4 + 1.3CH;\ \Delta H = -1114\ kJmol^{-1} \tag{1.1}$$

This equation is not exact as the composition of C-S-H is known to vary [Rayment 1982]. Still, $C_{1.7}SH_4$ is currently assumed to be an acceptable approximation for the product [Taylor 1993]. Portlandite (CH) is crystalline in nature and has a well-defined composition. It is known to grow either as irregular crystals or as hexagonal platelets, as it can be seen in Figure 1.1, depending on the pore-solution and cement composition [Gallucci 2007].

In Portland cement, belite also hydrates in a manner similar to alite, producing the same products, according to Equation (1.2), although belite reacts only to a small extent at early stages, and acts as a reserve for hydration at later stages [RILEM 1987].

$$C_2S + 4.3H \rightarrow C_{1.7}SH_4 + 0.3CH;\ \Delta H = -43\ kJmol^{-1} \tag{1.2}$$

Within a few hours of mixing with water, cement paste starts to gain in stiffness and strength, going from a viscous fluid to a plastic solid to finally a stiff solid. This change happens because the hydration products have a larger density than the anhydrous phases and occupy more space, filling most of the space created by the consumption of water and increasing the solid volume. In both (1.1) and (1.2) equations, two steps are involved: the rapid initial formation of gelatinous hydrate coatings around the cement

grains and, after a dormant period, the growth from these coatings of fine fibrillar C-S-H gel material into a reticulate network between the cement grains. Figures 1.1 and 1.2 show two scanning electron micrographs of Portland cement pastes prepared for the purpose of this thesis.

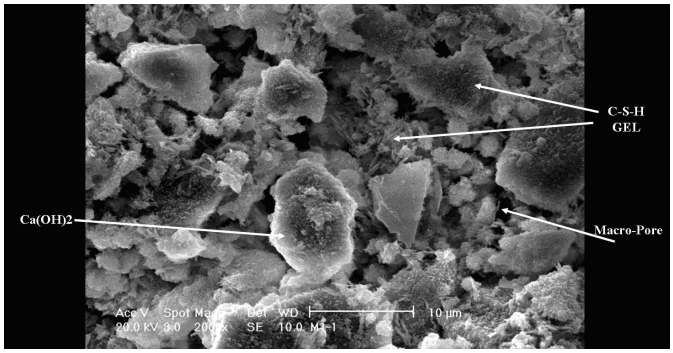

Figure 1.1: Scanning electron micrograph of hydrated Portland cement at the early stage of hydration

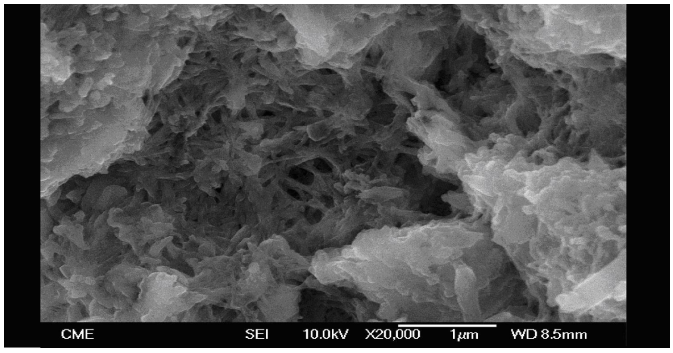

Figure 1.2: Scanning electron micrograph of fibrillar C-S-H in mature Portland cement paste

Figure 1.1 shows an early stage of hydration of the paste, where an amorphous-looking gelatinous envelope of C-S-H gel bridges the cement grains at their points of contact. *CH* portlandite can also be observed among the micro-macro porous structure of the hydrated material. Figure 1.2 corresponds to a mature paste, where C-S-H gel shows a fibrous morphology which provides a reticular network within the system. C-S-H is then considered as being responsible for the cement paste's internal skeleton, for the paste's adherence to the aggregates in the formation of mortar and concrete, and for

the strength and durability of cement-based materials.

From the above images, it is clear that the hydration of silicate phases in cement is not a conventional crystal growth problem such as is normally encountered when dealing with the separation of solids from aqueous solutions. The primary concern in understanding the microstructure of cement systems has focused on hydration process of cement and its behaviour upon heating. Such a heating process is of special relevance for us as it imposed an annealing process to the titanium-based materials which will be interacting with the cement.

1.3 Titanium Nitride

Titanium nitride (TiN) is a refractory interstitial nitride with a golden color, extreme hardness, corrosion resistance, and relatively high conductivity. Some properties of TiN compared with those of Ti, compiled from [Pierson 1996], [Oyama 1996], [Toth 1971] have been summarized in table 1.2.

Table 1.2: Several properties of TiN an Ti at ambient temperature

Property	TiN	Ti
Structure	fcc (NaCl)	hcp
Range of Composition	$TiN_{0.6-1.1}$	N.A.
Color	Golden	Grey
Density	5.40 g/cm^3	4.54 g/cm^3
Melting Point	2950°C	1940°C
Specific Heat	37.0 $J/mol \cdot K$	25.0 $J/mol \cdot K$
Thermal Conductivity	30 $Watt/m \cdot K$	13 $Watt/m \cdot K$
Thermal Expansion	$9.36 \times 10^{-6}/K$	$11 \times 10^{-6}/K$
Electrical Resistivity (bulk)	$20 \pm 10 \mu\Omega \cdot cm$	$39 \mu\Omega \cdot cm$
Vickers hardness	$21 - 24\ GPa$	$0.55 - 2.5\ GPa$
Modulus of Elasticity	$612\ GPa$	$110\ GPa$

Though several phases exist, the primary nitride phase, TiN, crystallizes in the NaCl-like structure with a lattice parameter of 4.24 Å for the stoichiometric material. The close packed structure, an fcc Ti sub-lattice with N filling the octahedral sites, is due to the relatively small size of the N atoms compared to Ti (0.74 Å versus 1.47 Å).

In order to accommodate the interstitial nitrogen, Ti must transform from a bcc or hcp structure to fcc, and N_2 must decompose to atomic nitrogen:

$$N_2 \rightleftharpoons 2N \;\; \Delta H = 943.8 KJ/mol \tag{1.3}$$

The largely metallic nature of TiN is clearly shown by the characterist metallic bounding of the transition metal nitrides (such as Ti, V, Zr, Nb, Hf, and Ta nitrides). Due to this nature, TiN exhibits high electrical and thermal conductivity, in addition to high melting temperatures, high hardness, and chemical resistance. TiN is isomorphous with TiC, TiOx and other interstitial nitrides and carbides, forming complete solid solutions [Pierson 1996].

1.4 Titanium Dioxide

Titanium is the world's fourth most abundant metal and ninth most abundant element. It was discovered in 1791 in England by Reverend William Gregor, who recognised the presence of a new element in ilmenite [Carp 2004]. Titanium is not found in its elemental state, it occurs mainly in minerals like rutile, anatase, ilmenite, leucoxene, brookite, perovskite and spene. In nature,titanium dioxide or *titania*, TiO_2, exists mainly in three types of crystal structure: rutile, anatase and brookite. Anatase and brookite transform to the rutile phase with heating as this is the most thermodynamically stable phase under ambient conditions. Both anatase and rutile have a tetragonal structure with TiO_6 octahedra sharing four edges, and two edges and two corners respectively. Several physical properties of anatase and rutile are collected in Table 1.3, from [Clark 1968], [Brown 1978], [Kim 1999], [Bendavid 2000] and [Hass 1952]. The rutile phase has a more closely packed structure with the oxigen bridge closer to each other than in anatase, giving a more densely packed structure. This structural feature gives rise to a greater chemical stability, greater hardness, higher specific gravity and higher refractive index, hence being commonly used as an opacifier.

Table 1.3: Compiled crystal structures and physiochemical properties for anatase and rutile TiO_2

Property	**Anatase**	**Rutile**
Crystal structure	tetragonal	tetragonal
Number Ti/unit cell	4	2
Lattice parameters (pm)	a = b = 378.45	a = b = 459.37
	c = 951.43	c = 295.87
Density	3.90 g/cm^3	4.25 g/cm^3
Refractive index	2.55	2.70
Electrical Resistivity	10^{14} Ω .cm	10^{14} Ω .cm
Hardness (Mohs' scale)	5.5-6	7-7.5

Electrically, titanium dioxide is a wide band gap semicondutor (3 eV for rutile and 3.2 eV for anatase), requiring photons of wavelength ≤ 383 *nm* and 403 *nm* repectively, to promote valence band electrons. Excited electrons and the consequent valence band holes are free to migrate within the crystal giving rise to electrical conductivity - the electrons having the greatest contribution [Cotton 1988].

1.5 General Scope of this Thesis: Aims and Objetives

The current doctoral project aim has been to improve to the fundamental knowledge on the nature of hydrated cement paste and C-S-H upon modification with titanium-based materials. Several issues in cement and concrete science were identified based on the review of relevant literature, which merited further research. These debated topics were found to be mainly concerned with the nanostructure of the C-S-H, the primary binding agent in hydrated cement systems. These discussions in the cement research community are partially due to the fact that the C-S-H produced in the hydration of Portland cement is a nearly amorphous material, contains impurities and exhibits a wide range of stoichiometries. On the other hand, lab-prepared titanium-based nanostructures (TiN thin film and TiO_2 nanoparticles) have been proposed as interacting agents to better understand the nanostructure of the C-S-H in hardened cement paste. The current work utilizes several novel experimental methods in order to

elucidate some of the new aspects of the nature of C-S-H after modification, in relation to that of the C-S-H formed in the hydrated Portland cement. The main objective of this thesis is to provide novel structures which might improve the performance of cement-based materials. The specific objectives of the current PhD thesis are summarized for each chapter as follows.

Chapter 1

To provide a background regarding the topic of this doctoral thesis and to address the aims and objectives.

Chapter 2

To identify the current debated issues related to the nanostructure and structural properties of cement-based materials upon modification with titanium-based nanostructures. The most relevant applications and research perspectives are also presented.

Chapter 3

To choose appropriate experimental tools in order to study the identified issues in chapter 2. Details of the experimental procedure and apparatus used throughout this work are provided. Sample preparation methodologies as well as thin film deposition techniques are also described in this chapter.

Chapter 4

To investigate the structures developed in the cement side of the interface between cement paste and TiN thin film. The chapter presents the experimental work carried out on specimens of cement paste deposited onto TiN films exposed to different temperatures. Structural characterization is carried out by X-ray Diffractometry (XRD) and Thermogravimetric Analysis (TGA/TD). Morphological characterization is performed by using Scanning Electronic Microscopy (SEM). The microstructure of the interface and outlayer is described. The results include characterization of cement hydration products at the interface under different curing temperatures.

Chapter 5

To investigate the TiN side of the interface between Cement Paste and TiN Thin Film. The chapter presents the experimental study of the interface between cement paste and TiN films, treated at different temperatures.Structural characterization is made by XRD, TGA/TD and X-ray Photoelectron Spectroscopy (XPS). Morphological characterization is performed by using SEM and High Resolution Transmission Electronic Microscopy (HRTEM) by means of cross-section measurements. To analyse the role of TiN thin film for anticorrosive protection systems in reinforcing steel, corrosion tests are described and performed in the samples by using potentiodynamic measurements.

Chapter 6

To identify the fundamental nature of the interactions between the hydrating cement phases and nano-sized TiO_2 structures. The effects of the addition of titania nanoparticles in the cement matrix is presented in the chapter, focusing on the environmental-friendly contributions of TiO_2 photocatalysis to cement paste. The experimental study consists in the preparation of cement paste specimens with different concentrations of TiO_2 nanoparticles. The samples are characterized morphologically by SEM. Structural characterization is made by XRD. Photocatalytic activity is analyzed by a tailor-made setup detailed in Chapter 3, and the influence of these interactions on novel composite properties such as photocatalic behavior.

Chapter 7

To provide a general discussion and summarize the main conclusions of each chapter presented in the thesis. This last chapter also contains future perspectives that give this research work further continuation.

CHAPTER 2

Literature Review

The scope of this literature review is neccesarily broad, and includes inorganic chemistry, materials science, physics and civil engineering because of the multidisciplinary nature of this thesis. C-S-H, as the principal component of the hydration of Portland cement, has been the topic of significant research over the past century. An understanding of the nature of this hydration product at the nano-scale is essential for the strategic modification of conventional systems and the development of new materials with enhanced properties. An attempt has been made in this chapter to summarize some of the general research studies pertaining to the main objectives of the current thesis. A more specific literature review will be provided in the introduction section of the next chapters relevant to each individual topic.

2.1 Nanostructure of C-S-H

C-S-H gel is the principle product of Portland cement hydration. The structure of this calcium silicate hydrate as it is formed during the hydration of Portland Cement, has been object of extensive study. However, knowledge of the atomic structure of this chemical phase is still undetailed. The chemical formulas for the C-S-H product in the equations (1.1) and (1.2), are approximate as the CaO/SiO_2 ratio of the C-S-H varies within the same paste. Moreover, the molar proportion of H_2O in C-S-H can not be easily determined due to the lack of a comprehensive definition for the state of water in C-S-H. Scanning electron micrograph of the products formed in hydrated

Portland cement is shown in Figure 2.1. C-S-H forms up to about 60% of the hydration products in hardened cement paste and is primarily responsible for some of its principal properties such as strength, shrinkage, and durability.

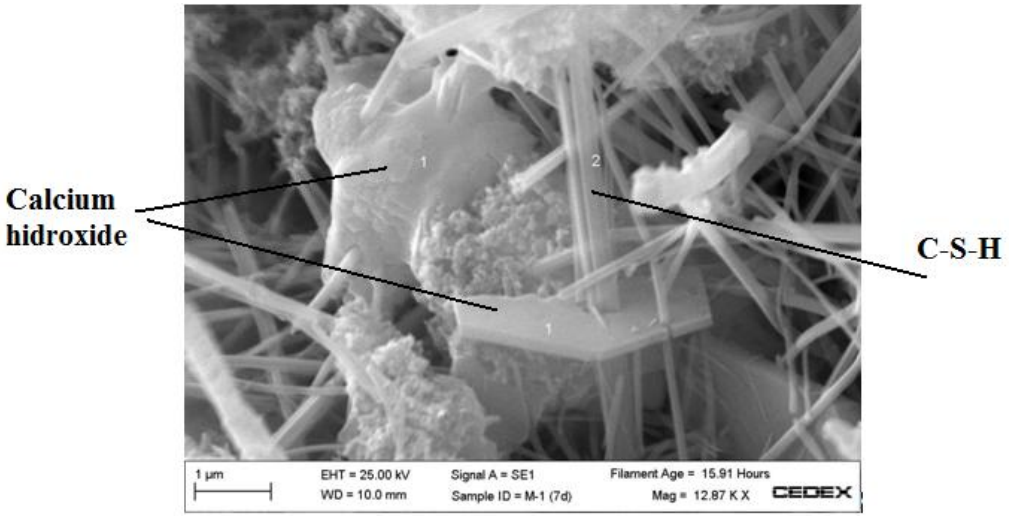

Figure 2.1: Scanning electron microscope image of the two main Portland cement hydration products: $Ca(OH)_2$, *portlandite*, and C-S-H.

2.1.1 Characteristics of C-S-H

The undefined and variable crystalline nature of C-S-H in cement systems, as well as the incorporation of other elements such as aluminum into its structure, are some of the barriers in the physical and chemical characterization of C-S-H. These have often been the main causes of discrepancy in the research results and a major source of discussion. The following sections provide a brief review of some of the research work relevant to this doctoral thesis.

2.1.1.1 C/S ratio

An important stoichiometric parameter that defines a C-S-H phase is the molar ratio of CaO to SiO_2 in its structure (C/S ratio). It is possible to calculate the C/S ratio

of the C-S-H produced in the hydration of calcium silicates by determining the content of calcium hydroxide [Ramachandran 1979] and unreacted materials using analytical methods such as thermogravimetric analysis or quantitative X-ray diffraction. The C/S ratio in calcium silicate hydrates usually covers a range from 0.7 to 2.0 with an average value of 1.75 in hydrated Portland cement [Richardson 1999].

Taylor clasified C-S-H systems into C-S-H (I) and C-S-H (II), respectively, for C/S ratios below and above the dividing value of 1.5 [Taylor 1997], [Taylor 1950]. However, not many researchers were able to produce the C-S-H (II). It was shown that a C/S ratio of 1.5 is generally a maximum value in the hydrate unless extreme reaction conditions are applied [Greenberg 1954]. Nonat suggested a categorization of C-S-H systems into three types: C-S-H(α) for C/S<1.0, C-S-H(β) for 1<C/S<1.5 and C-S-H(γ) for C/S>1.5 [Nonat 1994]. The most significant changes that occur in the structure of C-S-H with decreasing C/S ratio are an increase in the mean length of the silicate chains and the distance between C-S-H layers. These characteristics have been shown to affect the physico-chemical behavior of C-S-H [Taylor 1997].

2.1.2 State of water in C-S-H

A minimum amount of water is required for the hydration reaction of Portland cement to complete and provide a reasonable workability of concrete. Excess mixing water leads to a high porosity cement paste microstructure. Hence, moist conditions after the setting of the cement paste are required for the hardening of the hydrated cement and controlling issues such as shrinkage. The presence of water in the pore structure also facilitates the ionic movement and transport of aggressive chemicals into the concrete, which might deal to corrosion of the reinforced steel. Water and concrete form a very sophisticated “love/hate” relationship [Neville 2000].

The classification of the state of water in cement paste is generally based on the location where it is held and the nature of its bonding with the solid structure. The latter is a function of energy required to remove that water [Mehta 2006]. Although several

investigations have attempted to separate various forms of water in the cement paste and even in the more crystalline forms of C-S-H systems, the dividing line for the states of water is still not very clear [Feldman 1971].

Apart from the water vapor in the pores, it is suggested that water can exist in various forms e.g. capillary water (in voids larger than 5 nm), adsorbed water (held by hydrogen bonds on the surface of the hydrated particles) and interlayer water [Pellenq 2008]. The strongly held debate about the later water that is associated with the nanostructure of C-S-H still continues [Jennings 2008b], [Beaudoin 2008]. In this debate, it was also suggested that the C-S-H lamellae are held together by an electrostatic force [Jennings 2008a]. In this configuration, the interlamellar space is filled with quasi-immobile water molecules and calcium ions that are bonded to the C-S-H layer by partially covalent bonds.

2.1.3 Relation of C-S-H with crystalline phases

There are more than 45 known calcium (alumino) silicate hydrates of interest to cement chemists [Richardson 2008]. It was again Taylor, in the early 1950's, who claimed that the short-range order structure of C-S-H can be related to the structure of crystalline compounds with a silicate-chain repeat distance of 0.73 *nm* in one direction [Taylor 1992]. Among various calcium silicates, tobermorite and jennite appear to provide more structural similarities with the C-S-H gel in hydrated Portland cement. Both of these minerals have a layered structure and can be synthesized. Jennite is a rare mineral and is relatively difficult to synthetise, but various forms of the tobermorite are available and can be easily produced; 0.93, 1.1 and 1.4 nm tobermorite (the prefix denotes the distance between the layers (d002 basal spacing).

The structure of tobermorite was first described by Megaw and Kelsey [Megaw 1956]. They showed that this substance was closely related to the C-S-H (I) [Taylor 1997]. The crystal structure of 1.1 nm tobermorite was resolved by Hamid [Hamid 1981], and more recently the crystal structure of 1.4 nm tobermorite has also

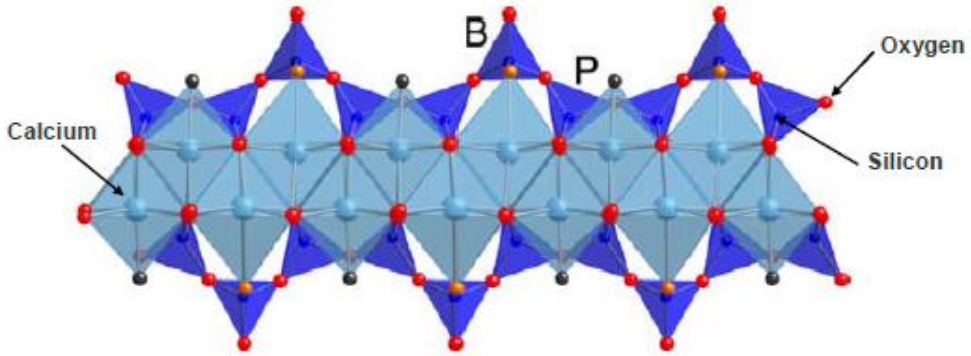

Figure 2.2: A schematic drawing of a tobermorite layer

been resolved [Bonaccorsiw 2005]. A tobermorite layer is formed from a sheet of calcium oxide flanked on both sides by silicate tetrahedra, as schematically shown in Figure 2.2, from [Richardson 2008].

In the above figure, the tobermorite layer features a main Ca-O layer with silicate tetrahedra attached on both sides. The directly connected silicate tetrahedron is called paired (P) and the silicate tetrahedron connecting two paired tetrahedra is called a bridging tetrahedron (B). The C-S-H in hydrated Portland cement is considered akin to tobermorite although it is lacking some of the bridging tetrahedra. The C-S-H in cement paste is therefore commonly referred to as a defect tobermorite structure. A stacking of these layers with mainly water molecules and calcium ions in between forms a typical C-S-H agglomerate.

2.1.4 Models for the nanostructure of C-S-H

Any model for the C-S-H systems should be able to account for the experimentally observed physical and chemical characteristics of this material at variable stoichiometries and environmental conditions. The proposed models in the literature can be differentiated in two categories:

- **Structural models**, are concerned with the structural implications and those that

mainly deal with the composition of the C-S-H. The structure-based models were introduced earlier in the cement research and are generally based on the surface area and adsorption-desorption data.

- **Composition-based models**, were developed later and advanced through the improvement and invention of experimental methods such as nuclear magnetic resonance spectroscopy.

For the purpose of this thesis, deeper details and understanding on composition-based models are not required. However, some experimental results obtained throughout this doctoral project might provide insights into the validity of one of the most important structure-based models suggested, whose features are discussed in the following section.

2.1.4.1 Colloidal Model

Among the many different structural models suggested for C-S-H [Richardson 2008], the colloidal models proposed by Jennings [Jennings 2008b] succesfully explain various bulk properties of C-S-H found in hydrated cement pastes. The basic of this models is the existence of a < 5 *nm* diameter building block. These basic units pack together to form the microstructure of C-S-H, as shown in Figure 2.3, (from [Jennings 2000]).

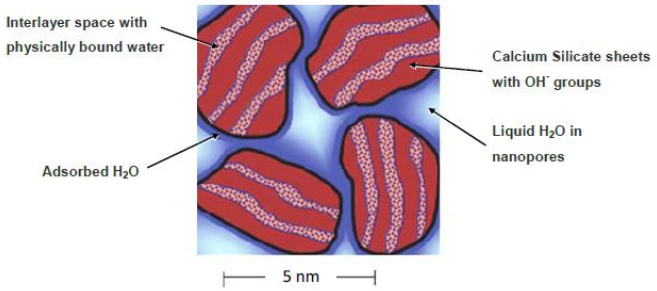

Figure 2.3: A schematic representation of the nanostructure of C-S-H

This model is based on the first structural model for the nearly amorphous structure of hardened Portland cement paste, developed by Powers and Brownyard and known as P-B model [Powers 1947]. Their classic set of experiments in the 1940's, primarily based on mass change measurements at varying humidity and temperature, was aimed at clarifying the role of water within the structure of the cement paste. In the P-B model, water can be present in two forms; evaporable (that is water lost under D-drying conditions over the vapour pressure of dry ice at 79°C) and non-evaporable (the remaining water that can be removed by heating up to 1000°C). The evaporable water was also categorized as "gel water" (about four monolayers of water on the surface of the gels) and "capillary water". Feldman and Sereda presented their model in 1968 [Feldman 1968] and was further explained in 1970 in a comparison with previous models [Feldman 1971]. Their evidence led to the concept of a layered model for C-S-H gel and a structural role was assigned to the water in the interlayer region. Feldman's later work on the diffusion of helium into C-S-H gel at various humidity conditions provided additional evidence for the layered nature of the C-S-H gel.

Assuming the validity of these proven concepts explained in previous models, the main concerns were regarding the nature of bonding between solid particles and the mechanism of water penetration between the particles. Jennings and co-workers have conducted extensive work on various properties of C-S-H gel such as density and porosity measurements as well as mass-change isotherms, based on which structural models were proposed for the C-S-H [Tennis 2000], [Allen 2000]. They suggest that the density of C-S-H is 2.604 g/cm^3 and its chemical formula is

$$(CaO)_{1.7}(SiO_2)(H_2O)_{1.8} \tag{2.1}$$

These results were obtained using small-angle neutron and X-ray scattering data with the assumption that the water (H_2O) in the C-S-H can be fully exchanged with heavy water (D_2O) after 24 hours of immersion.

Despite the complexity of the process of cement hydration, it is acceptable to

approximate the rates of the reactions involved by Avrami [Avrami 1939] equations of the form

$$\alpha_i = 1 - e^{a_i(t-b_i)^{c_i}} \tag{2.2}$$

where α_i is the degree of hydration of compound i at time t (in days). The constants a_i, b_i, and c_i have been determined empirically for a specific Portland cement [Dalziel 1986] [Taylor 1987] and are used as an approximation for other Portland cements. According to Taylor, the constants to be used in equation (2.2) are resumed in Table 2.1

Phase (i)	a	b	c
C_3S	0.25	0.90	0.70
C_2S	0.46	0	0.12
C_3A	0.28	0.90	0.77
C_4AF	0.26	0.60	0.55

Table 2.1: Constants used in the Avrami equation for calculation the rate of reaction of Portland cement reactants

Another important issue discussed in Tennis and Jennings' model is the calculation of the quantity of the various phases present in the cement microstructure at any given time. Hence, given the composition of the cement and the water:cement ratio, the percentage of capillary porosity, V_{cp}, is calculated as follows:

$$V_{cp} = V_w - \sum_i (V_p - V_r) \tag{2.3}$$

where V_w is the initial volume percent of water, V_p is the volume percent of hydration product, V_r is the volume percent of reactant, and the summation is over all reactions, i. The volume of gel porosity is included in the volume of C-S-H. According to this formula, the relative volumes of each of the phases in a typical Portland cement paste can be calculated and plotted as a function of the degree of hydration of the paste, as shown in Figure 2.4, from [Tennis 2000]

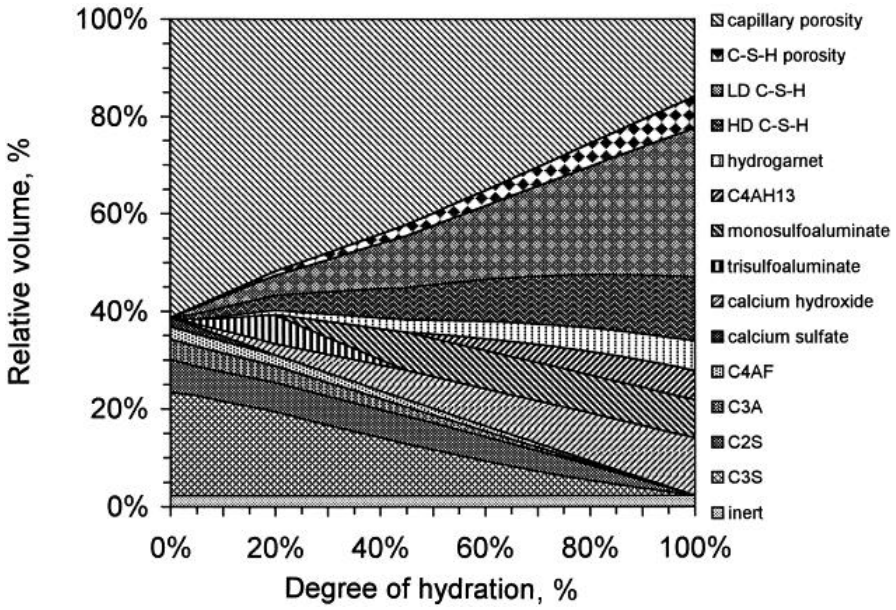

Figure 2.4: Relative volume of each of the phases (as predicted by the Tennis and Jennings′ model) as a function of the degree of hydration. The plot was obtained for a paste with water:cement ratio of 0.50, and 55% C_3S, 18% C_2S, 10% C_3A, and 8% C_4AF, an average Type I cement composition

The main concepts of the structural model outlined in this review, are considered to be relevant for discussing and understanding the results produced from this doctoral thesis.

2.2 Nanotechnology in Civil Engineering

The extension of nanotechnology to the applications in material science has already demonstrated its potential in the area of construction materials including traditional materials such as polymers, structural steel and concrete. Nanotechnology in civil engineering can be defined in the context of materials and structures as the synthesis, design and modification of materials with dimensions in the range of 1 to 100 nm. This new technology has the potential to significantly modify the intricate hydration mechanism of the cement-based materials and the properties of hardened concrete, allowing one to more precisely control and modify the mechanical behaviour of existing

systems or to tailor the performance of novel construction materials.

While it has been applied to many scientific and technological fields for more than a decade, it is only in the last few years that the possibility of using nanotechnology to improve the functionality of construction materials has been seriously contemplated. The application of nanotechnology has been slowed down by the intrinsically conservative nature of the construction industry. However, the use of revolutionary nanotechnology techniques in the development of new systems of construction material quality controls, in methods of diagnosing and repairing structures and even in the development of new advanced, "tailor-made" materials is now a reality [Sanchez 2000]. Figure 2.5 shows that there has been a considerable increase in the research on the nanotechnology of cement and concrete during the past few years. It seems that the key to resolve many of the debated topics in cement science lies at the nano-level. Table 2.2 summarises some ongoing applications of nanomaterials in the construction industry, addressing high performance structural materials and the corresponding expected enhancement, from [Lee 2009].

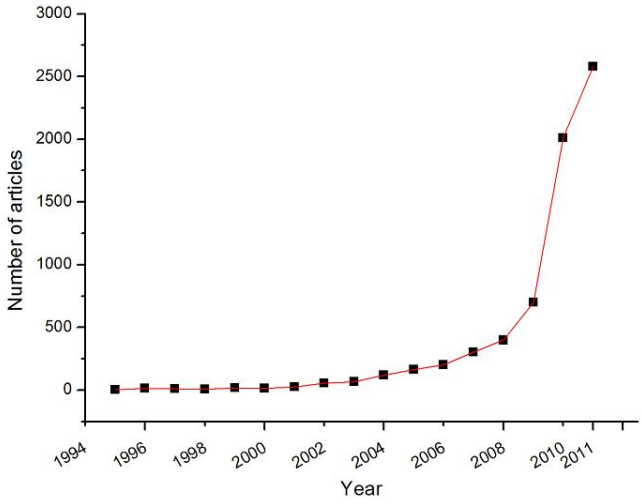

Figure 2.5: Number of articles containing cement+concrete+nanotechnology in the fields of chemistry, materials science, engineering and physics (source: google scholar, accessed February 2012)

Recently, many of the incoming applications for nanotechnology in construc-

Table 2.2: Selected Nanomaterials Applications in Structural Materials

Construction Material	Nanomaterial	Expectation	Reference
CONCRETE	Carbon Nanotubes SiO_2 Fe_2O_3	Reinforcement Crack Hindrance	[Li 2004] [Sobolev 2005]
STEEL	Copper Nanoparticles	Weld Ability Corrosion Resistance	[Ge 2008]
CEMENT	Carbon Nanotubes Polypropylene Nanofilter TiO_2	Strength Fire Resistance Self-cleaning	[Makar 2005]

tion, focus on new standards to achieve a sustainable development, that is, the ability to comtemplate today's needs without deteriorating the resources of the future. Since construction is one of the industries that requires the most energy and environmental resources and it is imperative to investigate how to develop and use cementitious materials in a sustainable way, respecting the enviroment and our existing natural resources. Therefore, one of the main aims of this doctoral thesis is to apply nanotechnology and its potential to a more environmentally friendly use of cement.

2.3 Chloride-Induced Corrosion on Reinforcing Steel

Focusing now on one of the main structural materials, reinforced concrete is a macroscopic heterogeneous composite material, aggregated at different structural levels. Hence, multiphase interfaces are involved in concrete structure and cement paste (concrete) behaviour. The steel reinforcement is embedded (on the meso-level, generally relevant to mm dimensions) in supposedly homogeneous bulk. Cement paste and aggregate particles, along with air pores and macropores dispersed in the cement paste matrix. Portlandite maintains the pH of the cement paste at a high level, between 12 and 13, and thus acts as an "alkaline reserve" and keeps the cement derivative safe from electrochemical corrosion. However, the capillary pore structure of concrete

is generally assumed to have significant relevance to permeability and other transport phenomena, facilitating chloride penetration and further corrosion of reinforcement in concrete. Chloride-induced reinforcing steel corrosion is by far the most common durability problem in reinforced concrete structures (see Figure 2.6).

Chlorides penetrate concrete through absorption, diffusion, electromigration, thermal migration and hydrostatic pressure, with diffusion being the dominant transport mechanism in marine environnments [Claisse 2005]. After initiation of the corrosion process, the accumulation of corrosion products (iron oxides and hydroxides), occupying a volume several times larger than that of the original material, leads to internal stresses that result in cracking and spalling of the concrete cover.

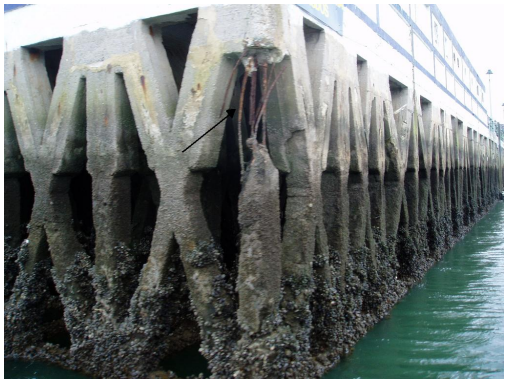

Figure 2.6: Chloride corrosion of steel rebar in a concrete pile causing delamination that results in spalling. Image taken in Guecho port, Vizcaya, Spain (January 2011)

A wide range of techniques have been reported in the literature that may be suitably employed for corrosion protection of steel in concrete structures, thus lengthening the reinforcement service life. Among them, the use of corrosion monitoring techniques [Shamsad 2003], corrosion inhibitors [Tritthart 2003], [Ormellese 2006], [Mammoliti 1999], [Soylev 2007], new compositions of steels [García-Alonso 2007] and novel coating systems [Asthana 1999], show only a few valuable examples of the intense interest in this field of research. On the basis of the environment in which the steel is going to perform, physical barrier coatings appear to be the most suitable protection system against corrosion, especially in certain points within the structure that

might show higher vulnerability. The basic protection principle is to create a protective barrier around either the concrete or the steel, thus decreasing permeability, and preventing the penetration of unwanted elements into the structure, such as chlorides in marine exposures.

With concrete being a porous material, a barrier method applied onto the steel surface isolates the steel from the environment, and protects it from aggressive service conditions. A variety of corrosion resistant coatings are currently available, most of them polymers, including epoxy, and silicones. However, they have all demostrated certain weaknesses facing diffusion of water through the coating and propagation between the coating and the substrate - the presence of water nearby might provoke the breakdown of the coating protection.

Another coating technique available for increasing reinforced concrete durability consists of applying a metallic film onto the steel surface, with the aim that the material used for the film will corrode preferentially when coupled to the steel. These sacrificial coatings are typically limited to zinc and nickel-based alloys, zinc being by far the most common coating protection material - either applied by hot-dip galvanization or plating - due to its pH/corrosion rate minimum coinciding with the pH of concrete at the passivate state. However, zinc does not perform as well when chloride is present in the cementitious material, due to the the production of a non-protective amount of expansive corrosion products from the zinc layer. A number of investigations have been carried out for developing new durable coatings as protective barriers against corrosion, chemical attack and hydro-thermal variation of the reinforcing structure [Hester 2007]. For example, nickel composite coatings containing carbon nanotubes have been proposed[Chen 2005], which act as physical barrier to the corrosion process by filling in crevices, gaps and microholes on the surface of the nickel coating.

2.3.1 Titanium nitride (TiN) coatings for corrosion resistance

TiN and other related transition metal nitrides, such as TiAlN and TiCN, find technological use in a wide range of applications. The bond structure in these transition metal nitrides is predominantly covalent, which provides the material with high hardness, excellent wear resistance and chemical inertness. The interest in thin films of metal nitrides is growing rapidly for such diverse applications as selective transmission coatings on architectural glass [Gordon 1997] [Xiaoxuan 2010], solar thermal applications [Yuste 2011] and diffusion barriers in integrated circuits [Suni 1985]. Furthermore, due to its intrinsically excellent tribological properties, titanium nitride films are commonly used as wear resistant coatings on machinery, steel cutting tools [Mitsuo 2000], [Mitsuo 2002], as well as corrosion and abrasion resistant layers [Martin-Palma 2003]. In addition, TiN is not cytotoxic and may be used in biomedical materials owing to its bio-compatibility and hydrophilicity [Manso-Silvan 2002].

TiN appears a promising material to be used for barrier coatings in reinforcing steel. TiN exhibits excellent corrosion resistance and a strength-to-weight ratio comparable with steel [Jindal 1999]. The reduction of maintance and repair expenses justify its higher initial cost. Most of today's wear applications, such as cutting tools, fully use TiN as protective barriers against corrosion. For the deposition techniques of thin films in the range of 1000 Å thickness, sputtering is feasible in a controllable manner for both compound and elemental targets (the source of the coating material). Adhesion is good and can be further improved by sputter cleaning the substrate or by bias sputtering. Large equipment is readily available and sputtering has become a highly automated process.

This doctoral thesis includes a detailed investigation of the interface between cement paste and sputter deposited TiN films for potential novel applications in corrosion protection of reinforcing steel.

2.4 Incorporating Nanomaterials into Cement

Innovation of the advanced materials with superior characteristics that can improve durability of structures and address sustainability issues has always been of interest to the construction industry. Nanomaterials and nanocomposites with unique physical and chemical properties are being increasingly used by this industry to enable novel applications. Several studies have been conducted with the aim of modifying the existing materials at the nano-scale, tailoring nano-sized materials for the specific applications or blending nano-sized materials with the existing cementitious materials. Carbon nanotubes, for example, have been shown to form strong bonds with cement paste and can result in micro-crack bridging [Makar 2005]. In addition the nanotubes may act as nucleating agents for C-S-H formation. Howard, who also worked on the use of carbon nanotubes (CNT) with cement paste, investigated nano-sized silica addition into cement paste and its effects on the mechanical behaviour [Howald 2008]. Vera-Agullo studied the addition of several nanomaterials to concrete, showing a reinforcement in the compression strength of up to 40% when adding nanosilica to the cement paste in mortar [Vera-Agullo 2009]. Beside nanocomposites, most current applications of nanotechnology are limited to the use of first generation passive nanomaterials which include titanium dioxide. In the following section, the addition of titania nanoparticles to the cement matrix, a relatively new and promising field in cement science, is reviewed.

2.4.1 Mechanism of photocatalysis

The term *photocatalysis* implies that light is acting as a catalyst in a reaction which is not likely to happen otherwise. However, the word photocatalysis is most often used to describe the process that semiconductor materials such as TiO_2 undergo when irradiated by light of a certain wavelength. Photocatalysis implies photon assisted generation of catalytically active species.

If a semiconductor, say TiO_2, absorbs photons of energy higher than its band gap

(Figure 2.7) then electrons are excited from the valence band to maintain electroneutrality. The hole and electron are mobile, and can be either trapped as Ti^{3+} and O^{-} defect sites in the TiO_2 lattice, or they can recombine, dissipating energy. Alternatively, the charge carriers can migrate to the surface where they may participate in surface redox reactions. The valence band of titanium dioxide is composed of 2p electrons, and the conduction band of 3d electrons. The band gap energy is 3.2 eV and 3.02 eV for anatase and rutile morphologies respectively, requiring photons of wavelength less than 384 nm and and 410 nm to excite electrons across the band gap.

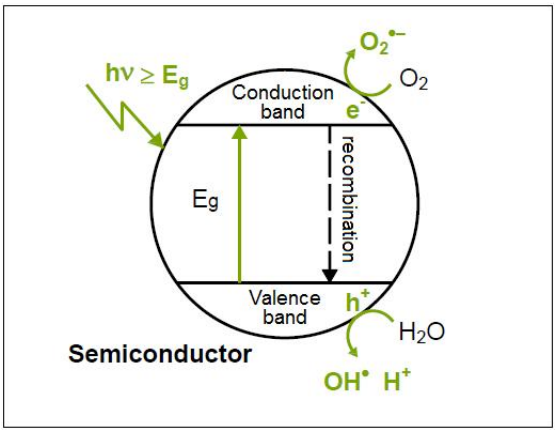

Figure 2.7: Photocatalytic splitting of water: photoexcitation of an electron from the semiconductor valence band to the conduction band, leaving a positive hole in the valence band.

The energy level at the top of the valence band determines the oxidising ability of the holes and the energy level at the bottom of the conduction band the reducing ability of the electrons. These energy levels are termed flat band potentials (V_{FB}). Thermodinamically, the valence band holes can *oxidise* adsorbed couples photochemically if they have more negative redox potentials than the V_{FB} of the valence band. Similarly, the conduction band electrons can *reduce* absorbed couples if they have more positive potentials than the V_{FB} of the conduction band.

2.4.1.1 Photocatalytic degradation of pollutants

Since the beginning of the 20th century, TiO_2 rutile type has been used as a pigment for paintings, cosmetics and others. The practical and potencial applications of pigmentary and nano-sized titanium dioxide are vast, it is in widespread use in sunscreens [Weir 2012], wood coatings [Allen 2000], printing inks [Arin 2011] among other applications. Only since 1972, when the work of Fujishima and Honda on the photocatalytic splitting of water using titanium dioxide electrodes (anatase type), was it made possible to use its photocatalytic properties for other goals. [Fujishima 1972]. Their work ignited a revolution in the world of semiconductor research with Frank and Bard going on to demonstrate titanium dioxide's unique properties for environmental remediation through the reduction of CN^- in water [Frank 1977], and Pruden using TiO_2 for the mineralisation of organic pollutants [Pruden 1983]. Since then, there has been considerable research into the use of titanium dioxide as a photocatalyst for environmental remediation for detoxification/disinfection or general cleaning, to degrade chemicals or biological organisms, such as in [Dominguez 1998].

The first applications of TiO_2 as photocatalysts in the construction industry were intended to obtain an automatic cleaning process for buildings facades (self-cleaning), especially for materials based on white cement. In this sense, the self-cleaning activity of cementitious materials loaded with TiO_2 has been evaluated through laboratory tests using organic dyes as pollutant models. In most of the cases, the photocatalytic activity has been stimulated by using different lamp types containing long wavelength UV rays.

In the presence of air or oxygen, UV-irradiated TiO_2 is capable of reducing many organic contaminants completely. The activation of TiO_2 by UV light can be written as:

$$TiO_2 + h\nu \longrightarrow h^+ + e^- \tag{2.4}$$

As shown in Figure 2.7, the oxidative and reductive reactions are expressed as oxidative reaction:

$$OH^- + h^+ \longrightarrow OH\bullet \tag{2.5}$$

reductive reaction:

$$O_2 + e^- \longrightarrow O_2^- \tag{2.6}$$

In the degradation of organic compounds, the hydroxyl radical ($OH\bullet$) which comes from the oxidation of adsorbed water or adsorbed OH^-, is the primary oxidant; and the presence of oxygen can prevent the recombination of hole-electron pairs. The final products of reactions are CO_2 and H_2O:

$$OH\bullet + pollulant + O_2 \longrightarrow products(CO_2, H_2O, etc) \tag{2.7}$$

In 1996, the first laboratory experiments regarding the self-cleaning properties of cementitious materials containing TiO_2 were reported. These tests were developed for designing the mix composition of the cementitious material for the church Dives in misericordia (Rome, Italy). From those experiments, a new cement type called TX Millennium resulted [Cassar 2003]. Using an aerograph technique, white cement disks containing 5% of titanium dioxide (Degussa P-25) were impregnated with phenantroquinone (yellow dye). A solar simulator composed by 4 lamps of 400 W ($\lambda >> 290\ nm$) was used to activate the TiO_2 photocatalysis and the reflectance (%) was used to follow the photodegradation of the dye. Only 8 hours were required to obtain almost complete recovering of the colour of the white cement disks (see Figure 2.8 from [Maury 2010].

Despite these proven functional characteristics, such as self-cleaning, antimicrobial properties as well as the degradation of a range of organic (e.g. volatile organic compounds) and inorganic pollutants (e.g. NO_x and SO_2), technical aspects such as UV radiation acquiring, are still a limitation for the large scale application of this light-driven technology is required [Maury-Ramirez 2011]. In addition, the photocatalysis mechanism of TiO_2 has certain limitations that hinder the development of commercial applications. For example, the large band gap of TiO_2, the electron-hole recombination process and deactivation of TiO_2 by partially oxidised intermediates block that occupy active catalytic sites on the photocatalyst. Additionally, it is still not clear

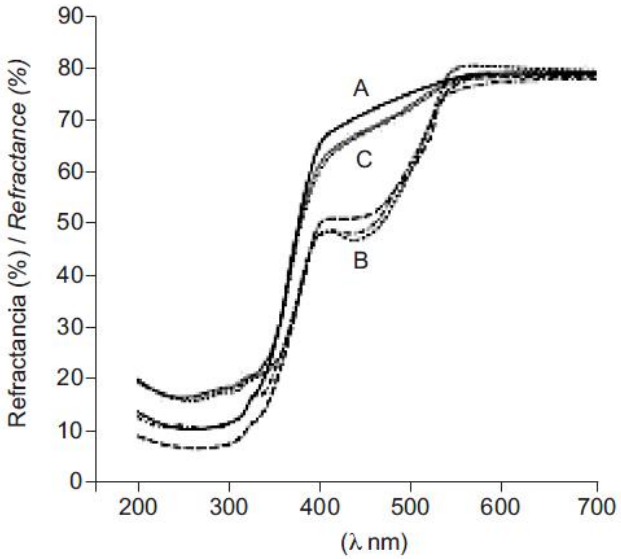

Figure 2.8: Time evolution of the reflectance spectra of TiO_2 enbedded in white cement samples in which phenanthroquinone was applied [Cassar 2003]. (A) Original clean surface, (B) surface after deposition of phenanthroquinone (dashed line), (C) Surface after 8 h irradiation (dotted curves under curve A).

what the most efficient way is to incorporate TiO_2 photocatalysts in the cementitious materials. In this sense, the choice of TiO_2 nanoparticles synthesis technique can be a key factor in determining the effectiveness of the photocatalyst.

This research focuses on sol-gel processing techniques to produce TiO_2 nanoparticles in order to provide some new insights into the use of sol-gel method for the incorporation of TiO_2 into the cement matrix.

2.4.2 Influence of nano-sized TiO_2 on cement hydration

Research has shown that the photocatalytic activity is superior in nano-crystalline TiO_2 and that it exhibits maximum efficiency in anastase phase compared to rutile or brookite phase [Tanaka 1991]. When added to Portland cement, it is considered to act as inert filler and is not believed to take part in the hydraulic reaction of cement. However, the modification of particle size distribution, due to chemically inert filler addition, changes the system porosity, providing additional sites for nucleation of cement hydra-

tion products. Consequently, the kinetic reactions might be catalyzed. In this sense, [Jayapalan 2009] reported an increasing effect in the rate of early age hydration proportional to the dosage of TiO_2, as well as finding that smaller particles seem to accelerate the reaction more than larger particles.

Another relevant study on the properties of cement paste with embedded TiO_2 nanoparticles, was the work of Nazari and coauthors, [Nazari 2010]. Their results show that the nano-TiO_2 blended concrete had significantly higher compressive strength than the same concrete without any addition, being 1.0% the optimal concentration of nanoparticles in the cement matrix. They elegantly explained the role of nano-TiO_2 as being responsible for accelerating C-S-H gel formation by increasing the amount of crystalline $Ca(OH)_2$ in the early stage of hydration. This in turn led to an increase in the fluxural strength of concrete.

The effect of nanoparticles of anatase powder on early-age hydration kinetics of tricalcium silicate (alite) was extensily investigated by Lee and Kurtis [Lee 2010]. The authors found that the addition of TiO_2 increases the degree of hydration at 12 and 24 h. In addition, the rate of hydration of 10% and 15% TiO2 pastes appears to be accelerated, while in the 5% TiO_2 paste the rate was delayed, which affects the length of the induction period as compared with the control paste. Lee and co-authors suggested that hydration products are formed on or near the surfaces of TiO_2 particles, as well as on the C_3S surface, therefore demonstrating that the addition of TiO_2 nanoparticles accelerates the early hydration by providing additional nucleation sites.

While in these and other reported studies TiO_2 particles were added as TiO_2 powder and mixed with water prior to the addition of cement, to our knowledge there has been no investigation of the microstructure and photocatalytic activity of cement pastes doped with nano-sized TiO_2 prepared by other methods, for example the sol-gel technique.

CHAPTER 3

Experimental Techniques

The experimental techniques used in the investigations are an essential part of this thesis. They are commonly known techniques in the field of science and engineering, especially in the study of materials at the micro and nano-scale. Some techniques were used to characterize the materials and to conduct the elemental analysis, while others were used to investigate certain properties of the materials. In this chapter, each experimental technique will be described with its general, where a brief background theory and capability of the technique will be illustrated. It is important to mention that often a combination of these techniques is employed in order to strengthen certain conclusions about the structure and behavior of materials since each individual technique is limited in some aspects. The experimental setup and procedure remain the same throughout the thesis, unless otherwise stated. Detailed explanation of the experimental set-up and scientific method for each part of the current work are mentioned in the relevant chapters. The details of the synthesis of TiO_2 nanoparticles by sol-gel method and thin film TiN deposition technique are, however, described here as they are referred to in their corresponding chapters.

3.1 Synthesis and Deposition Methods

3.1.1 The Sol-Gel process

3.1.1.1 General description

Sol-gel is a common chemical approach to produce high purity materials shaped as powders, thin films, fibres, monoliths and self-supported bulk structures [Keshmiri 2006], [Muggli 1998], [Walker 1995]. The sol-gel method has several advantages over other synthesis techniques such as purity, homogeneity, stoichiometric control, ease of preparation and dopants introduction, as well as the ability to produce thin film coatings or porous powders. However, sol-gel processing does not designate a unique technique, but a very broad type of procedures that centralizes around a single approach [Pierre 1998], as shown in Figure 3.1.

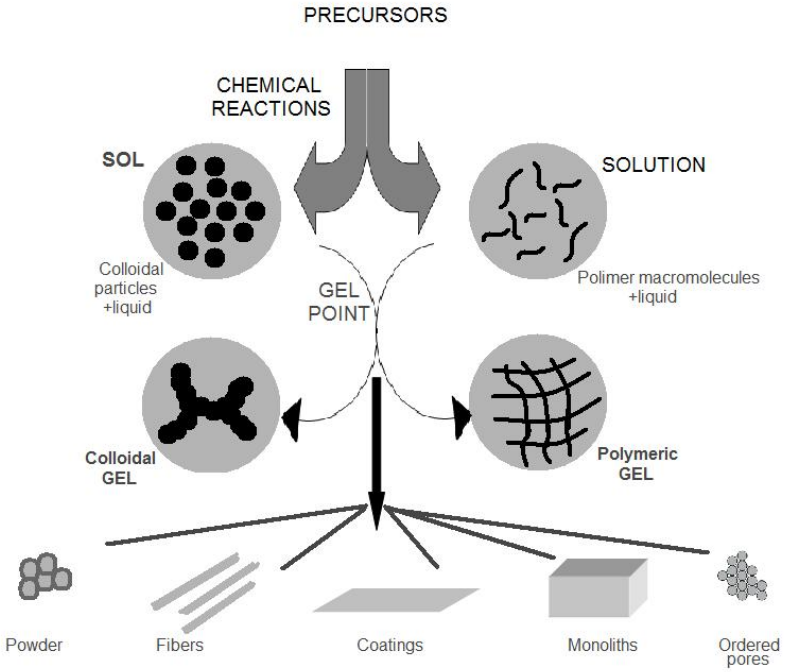

Figure 3.1: Schematic chart of Sol-Gel processing

The chemical reactant that contains the cation M present in the final inorganic sol or gel is called the *precursor*. There are two main groups of precursors for carrying

out sol-gel synthesis, the non-alkoxide route and the alkoxide route. The non-alkoxide route uses metallic salts ($TiCl_4$) as the starting material. This requires the removal of the inorganic anion to produce the required oxide (titanium dioxide). However, halides often remain in the final oxide material and are difficult to remove. The alkoxide route involves hydrolysis of a metal alkoxide, followed by condensation. Water is therefore a major reactant in order to transform the precursor into an oxide. Organic solvents, like ethanol (C_2H_5OH) are also frequently used in sol-gel processing in order to control the reaction of alkoxide precursors with water, hence to direct with more flexibility the structureof sol-gel produts.

Considering the alkoxide route for sol-gel processing, the general formula of an alkoxide is $M(OR)_n$, which indicates that they are a combination of a cation M with n alcohol groups ROH, where R is *ethyl*. An example of alkoxide-type precursor is titanium isopropoxide ($Ti(OCH(CH_3)_2)_4$). The hydrolysis/condensation reactions typically form a three dimensional polymeric structure that leads to the formation of TiO_2 colloids in the nanometer range. These reactions can be schematically represented as followed:

$$Ti(OCH(CH_3)_2)_4 + 4H_2O \rightarrow Ti(OH)_4 + 4CH(CH_3)_2OH \ \ (hydrolysis) \tag{3.1}$$

$$Ti(OH)_4 \rightarrow TiO_2xH_2O + (2-x)H_2O \ \ (condensation) \tag{3.2}$$

This sol-gel process to synthesize TiO_2 nanoparticles has been broadly reported and susscesfully utilized elsewhere [Trung 2003], [Sugimoto 2002b], [Sugimoto 2002a], [Mahshid 2007]. The alkoxide route described above is used throughout this thesis to produce TiO_2 nanoparticles for photocatalytic studies in cement matrix.

3.1.1.2 Experimental description

Titanium isopropoxide (TTIP) (97%) was purchased from Sigma-Aldrich. TTIP solution was then prepared at 0.4 M in ethanol, with a precise TTIP/water molar ratio of 0.82 and pH of 1.27 controlled with HCl. The produced sol solution was stored at room temperature for 24 h for the completion of hydrolysis/condensation reactions.

In previous work carried out in our laboratories, the TTIP solution described herein was modified with Polyethylene-glycol (PEG) within a sol-gel scheme for potential applications of bioadhesive surfaces [Vaquero 2010]. Results show a distribution of dispersed nanoparticles presenting a mean diameter size of 14 ± 7 *nm* (Figure 3.2). In the mentioned work, the addition of PEG was aimed to provide surface antifouling properties to this TiO_2-based hybrid material, not being that organic compound included in our sol-gel process. However, the same distribution of TiO_2 nanoparticles as shown in Figure 3.2 can be considered to be present in the so-prepared sol-gel TTIP solution used thoughout this doctoral project.

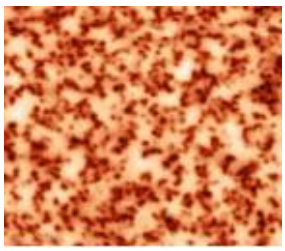

Figure 3.2: AFM phase image ($10 \times 10 \mu m^2$) of Ti-PEG-PEGd layers showing TiO_2 nanoparticles as sinthesized by sol-gel process, from [[Vaquero 2010]]

3.1.2 Magnetron sputtering

3.1.2.1 General description

Magnetron sputtering deposition technique is based on the physical and chemical reactions that take place when a gas discharge occurs within a pressure controlled gas chamber. A gas discharge is generated by applying a suficiently high potential differ-

ence between two electrodes in a gas atmosphere. The generated electric field partially breaks down the gas into ions and electrons, which can interact in different plasma processes. When besides the electric field, also a magnetic field is applied, the electrons can be used more efficiently. This kind of gas discharge is called *magnetron discharge*, and is used since the 1970's [Waits 1978] as sputter deposition device, for coating materials with a thin metallic or compound layer. In the sputter deposition process, species with a sufficient amount of energy bombard a target, which initiates a collision cascade in the target, leading to a possible release of a surface atom. This target process is called *sputtering*. The sputtered atoms pass through the plasma and can be deposited on a substrate, forming a thin film. The sputter deposition mechanism is schematically presented in Figure 3.3 (left): after bombardement of (for example) Ar^+ ions from the plasma, a collision cascade follows in the titanium target, after which a Ti atom can be sputtered. Subsequently, this Ti atom can be deposited on a substrate.

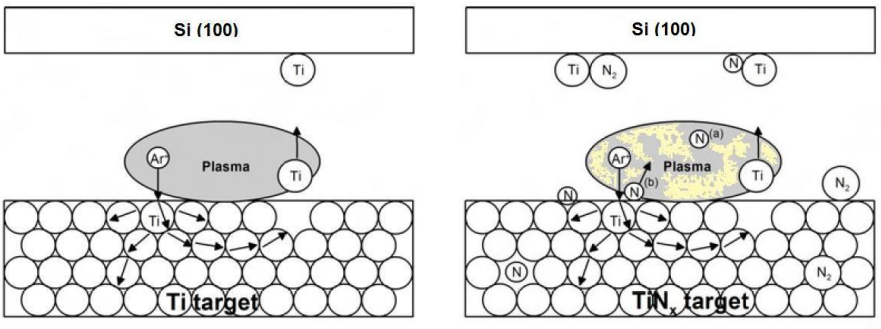

Figure 3.3: Schematic representation of the conventional (left) and reactive (right) sputter deposition process on Si (100) substrates

Charged particles with mass m, velocity v, and charge q from the plasma circulate around the magnetic field lines with magnitude B, being their Larmor radius

$$r = \frac{mv}{qB} \tag{3.3}$$

The high ion mass causes the ion Larmor radius to be very large, leading to an almost straight movement of the ions. However, electrons have a much lower mass,

which causes them to be trapped in the magnetic field. As a consequence, the electrons have longer mean free paths, and therefore a higher probability for ionizing the background gas, and hence creating ions. When these ions, accelerated by the electric field, hit the cathode target, target material can be sputtered. The enhanced ionization results in more sputtering, and allows the magnetron to operate at lower pressures (typically in the range of 0.1 to 1 Pa [Buyle 2005]) in comparison to non-magnetized sputtering discharges. Due to the lower pressure, the sputtered atoms will be less scattered on their way to the substrate. This results in a more efficient deposition.

When a reactive gas, like nitrogen or oxygen, is added to the argon background gas, atoms originating from this reactive gas or the gas molecules themselves can react with the sputtered metal atoms on the substrate to form a metal nitride or oxide layer, in a process called *reactive sputter deposition*. This process is presented schematically in Figure 3.3 (right). Ions from the reactive gas can be implanted in the target material, so that reactive gas molecules and atoms can be chemisorbed at the target surface, and chemisorbed species can be then implanted into the target [Depla 2008]. Subsequently, they react with the target atoms, to form a nitride or oxide layer, for example the TiN_x target on Figure 3.3 (right).

3.1.2.2 Experimental description

TiN coatings were prepared as previously optimized in [Manso 2001]. The magnetron sputter used was an Ion-Tech system with planar magnetrons. The thin films were obtained by reactive sputtering of high purity titanium targets (Kurt J Lesker, 99.99%) in presence of Ar and N_2, under the proportion 9/1. Depositions were performed on Si (100) substrates with a total sputtering power of 300 W and chamber pressure of 1.5×10^{-3} $mbar$. The films were then allowed to cood down in Ar atmosphere during one hour. The TiN deposition parameters are shown in Table 3.1.

Current	0.5 A
Voltage	600 V
Pressure	1.5×10^{-3} mbar
Deposition rate	400 nm/h

Table 3.1: TiN coatings deposition characterists

3.2 Specimen Preparation

3.2.1 Cement paste

A basic description of the preparation of the cement paste used throughout this doctoral project is illustrated in this section. Type CEM I 42,5 ordinary Portland cement (Type I according with ASTM C150) was supplied by Portland Valderrivas, Madrid, Spain. Chemical and phase composition of this cement are shown in Table 3.2. The cement pastes were prepared with de-ionized water, using a water/cement ratio of 0.5 by mass. The cement powder was first placed in a mixing bowl. Initially, a small amount of the mixing water was added. The mixing was conducted for a minute to remove lumps in the cement powder. The rest of the mixing water was then poured into the bowl, mixed for two more minutes, and then shaken for 30 seconds to remove any air bubbles.

Chemical Composition					
SiO_2	Al_2O_3	Fe_2O_3	CaO	MgO	SO_3
20.80	4.40	2.90	62.30	2.70	3.14
Mineralogical Composition					
	C_3S	C_2S	C_3A	C_4AF	
	50	24	11	8	
Fineness (cm^2/g): 1800					

Table 3.2: Chemical and mineralogical composition of OPC ASTM Type I(wt %)

3.3 Characterization Techniques

3.3.1 Thermogravimetric analysis

Thermogravimetric Analysis (TGA) involves monitoring the change in mass of a material as a function of temperature and time. TGA provides critical information required for the determination of properties of hydrated cement, such as degree of hydration, water content of specimen and degree of carbonation. TGA generally consists of a sensitive microbalance and a high temperature furnace as shown in Figure 3.4.

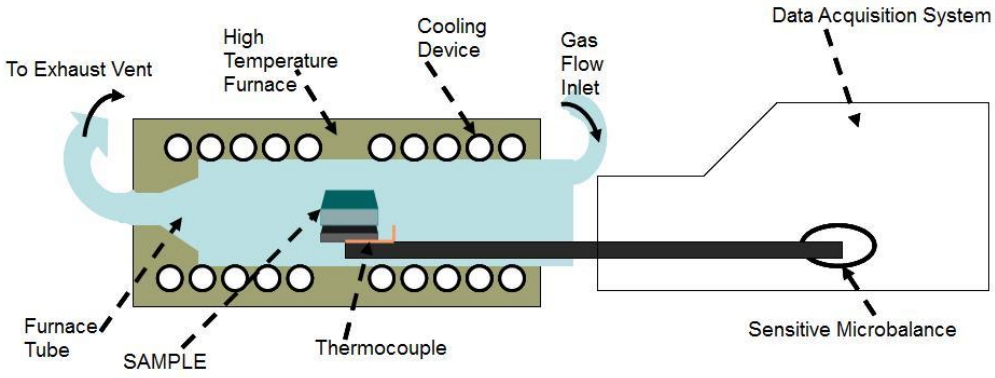

Figure 3.4: A schematic of a TGA

The specimen is placed in a platinum cup which is loaded onto a balance beam. The beam is installed to the sensitive microbalance where the data acquisition system monitors the change in mass of the specimen. A thermocouple is attached in the balance beam. The platinum cup along with the specimen, are introduced in a tube which is installed in the high temperature furnace. A cooling apparatus is embedded around the tube, so that the specimen can be subjected to desired heating rates. A gas flow inlet is attached to the furnace tube so that the test can be conducted under desired gases, which are usually air or nitrogen. The other end of the furnace tube is connected to an exhaust vent for decomposed substances from the specimen to be ventilated during the test. The TGA is typically capable of heating the specimen up to 1500°C.

A typical TGA result and its derivative curve for anhydrous Portland cement ig-

nited up to 1050°C are illustrated in Figure 3.5. A weight loss between around 90°C and 140°C corresponds to the decomposition of gypsum. A large drop in weight at around 575°C up to 725°C is a decomposition of $CaCO_3$ indicating that the cement had been carbonated remarkably during storage. A small weight loss at around 400°C is a decomposition of $Ca(OH)_2$ also indicating that the cement had been exposed to the moisture in the air during storage. The usefulness of TGA was greatly increased by introducing the derivative curve of weight change. Dehydration and decomposition of materials can be illustrated as a peak on the derivative curve and the area under the peak represents the amount of weight loss within a particular event. Further information on TGA can be found in Ramachandran [Ramachandran 1969].

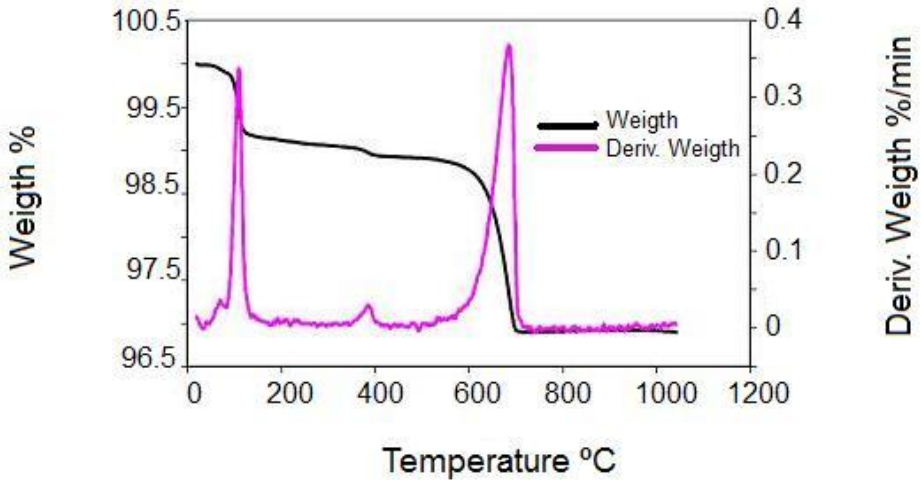

Figure 3.5: A typical TGA result and its derivative curve for anhydrous Portland cement

3.3.2 X-Ray diffractometry

One of the most important techniques to characterize cementitious materials is X-ray Diffractometry (XRD). XRD can be used to identify and characterize the crystalline

component of a material. It provides valuable information on phases, preferred crystal orientations and other structural parameters such as grain size, crystallinity, strain and crystal defects. A quantitative analysis can also be conducted if a proper experimental procedure is taken. The theory of XRD is based on the diffraction of x-rays on various structures of atoms in a crystal at certain angles of incidence as shown in Figure 3.6 and can be expressed by the Bragg's law as follows:

$$m\lambda = 2dsin\theta \tag{3.4}$$

where m is an integer, λ is the wavelength of X-rays, d is the distance between the atomic planes and θ is the angle of incidence. A wave reflecting from the second atomic plane has to travel a distance $2dsin\theta$ farther than the wave reflecting from the top planes, which is equal to $\lambda(m = 1)$. All the wave reflecting from the planes below the top planes are retarded with respect to the wave reflecting from the top plane by $m\lambda(m = 1, 2, 3, ...)$. This phenomenon is known as diffraction.

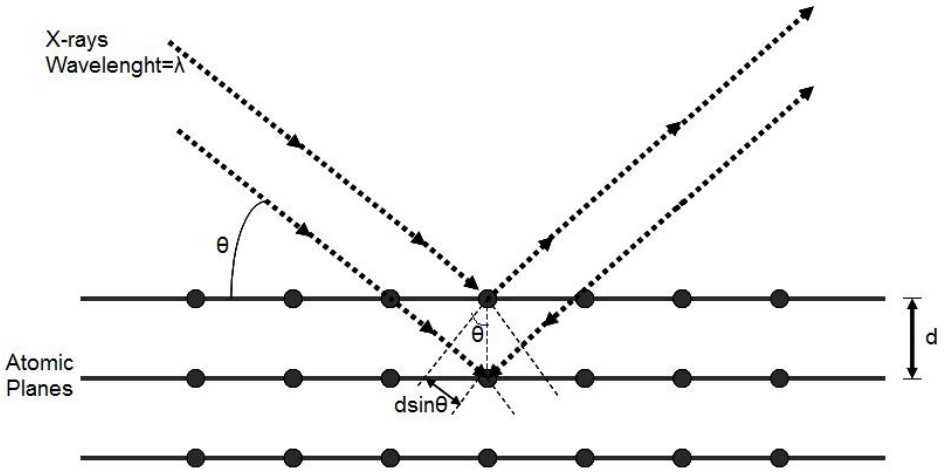

Figure 3.6: Diffraction of X-rays on the atomic planes in a crystal

A schematic of an XRD difractometer is shown in Figure 3.7. An XRD system can be slightly varied depending on the diffractometer geometry that an instrument is based on. The system shown in Figure 3.7 is based on the Bragg-Brentano geometry,

whereas other geometries such as parallel beam geometry are also available. The x-rays are emitted from an x-ray tube, travel through a divergence slit which collimates the x-rays and impinge on a specimen. The x-rays scatter from the specimen and the diffracted beams travel through a receiving slit to a detector. The unit of both x-ray tube and detector rotate about the specimen, so that the x-rays emit onto the specimen at various angles. The detector measures the x-ray intensity as a function of angle 2θ. Measurement of the x-ray intensity appears as intensity peaks and the intensity peaks for all the common substances are stored in database. In the so called specular $\theta/2\theta$ geometry samples were irradiated with monochromatic CuK_α radiation ($\lambda = 0.154\ nm$) under an incident angle θ, and the reflected intensity was measured at an angle 2θ. A typical diffractogram consists of a plot of the intensity versus the detector angle, which was typically 20-60° in 2θ used in this thesis.

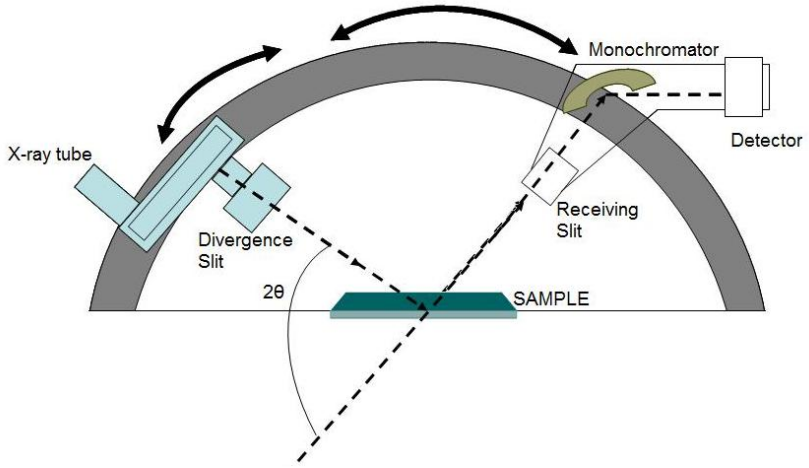

Figure 3.7: A schematic of an XRD

If the tested specimen is an unknown material, the substance can readily be identified by searching the database, especially with the recent development of well-designed software and powerful computers. XRD can also be used, for example, to determine the degree of hydration of cement, by analysing the change in the intensity peaks of $Ca(OH)_2$, which grow as hydration takes place. It is generally possible to detect the presence of a phase if there is more than 5% abundance of a specimen. The use of

XRD is however limited for amorphous materials, as opposed to crystalline materials, because of the nature of the principle behind this technique. The combination of XRD with other techniques is therefore often necessary to characterize the amorphous materials and amorphous contents in a cementitious specimen. Further information on XRD can be found in [Jenkins 1996] (1996).

3.3.3 X-ray photoelectron spectroscopy

X-ray photoelectron spectroscopy (XPS) is based on the photoelectric effect in which the interaction of an X-ray photon of sufficient energy with a solid results in the emission of an electron from its surface. The usually applied X-ray radiation ($1 - 15\ keV$) is capable to induce electron emissions not only from the outer orbitals but also from core levels of all elements of the periodic table. Upon photoionization, the emitted photoelectron leaves the atom behind in a single ionized state. This vacancy can again be filled by an Auger process giving rise to Auger lines in the spectrum or a flourescent transition. The energy scale commonly used in photoelectron spectroscopy is a binding energy scale using the Fermi energy as the reference level. The energy balance of the process is described as follows:

$$E_i^F = h\nu - E_k + \Phi_{spect} \tag{3.5}$$

where E_k is the kinetic energy of the emitted electron, E_i^F is the ionisation energy related to the Fermi level and Φ_s is the work function of the spectrometer. E_i^F is usually called as *binding energy* (B.E. or BE), although is known that Equation (3.5) describes the energy of the ionisation process.

If the sample is conductive, there is contact potential between the material and the spectrometer, allowing the Fermi level coupling equalizing between them. For low conductivity or insulating samples. a positive charge (Φ_{ch}) will build up in the sample due to the emission of electrons. Thus, the emitted electrons will have lower kinetic

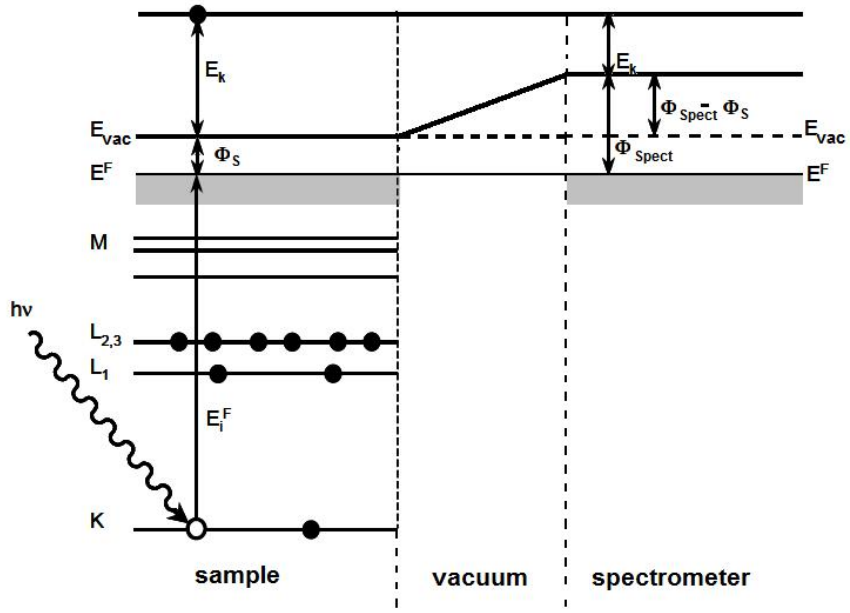

Figure 3.8: Energetics of the photoionisation process. E^F is the Fermi level, E_{vac} is the vacuum level in both sample and spectrometer, E_k is the kinetic energy of the photoelectron, Φ_{spect} is the work function of the spectrometer.

energy. This process is ilustrated in Figure 3.8. The energy balance is then expressed in the following equation, with the introduction of binding energy instead (E_i) of E_i^F:

$$E_i = h\nu - E_k - \Phi_{spect} - \Phi_{ch} \tag{3.6}$$

In order to identify correctly the spectral lines and to evaluate the chemical state by the energy shifts of the lines, it is necessary to determine their energy with $\pm 0.1 - 0.2\ eV$ accuracy. For this reason, the linearity of the energy must be calibrated and the correction for the Φ_{spect} and Φ_{ch} components must be done with similar accuracy.

3.3.4 Scanning electron microscopy

High resolution microscopes have been used more frequently as the studies of materials at the smaller scale became more common. Among other high resolution

microscopes, a scanning electron microscope (SEM) has been a leading tool to reveal and analyze the surface characterization of materials at the nano-scale. Typically, the resolution of SEM can be as high as 10 to 5 *nm* depending on several factors such as types and surface conditions of the specimens. A schematic of a SEM is illustrated in Figure 3.9.

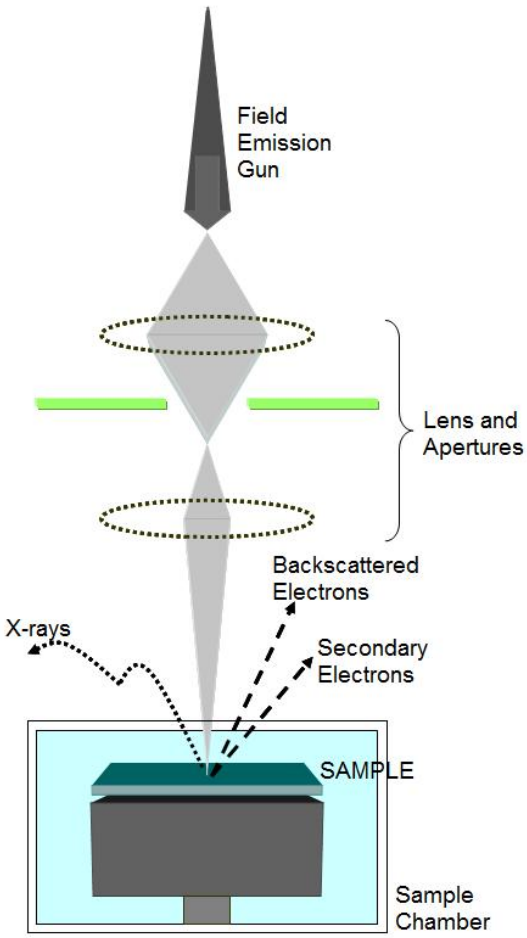

Figure 3.9: A schematic of a SEM

A beam of electrons is generated and emitted from a field emission gun located at the top. The beam travels through a series of lenses and apertures to be focused into a very fine focal point on a specimen. When the beam strikes the surface of the specimen various surface interactions occur. Secondary and backscattered electrons are collected by detectors and converted into an image of the surface. Xrays, which are

also produced from the surface interaction, can be detected by the SEM equipped with energy dispersive X-ray spectrometer. The sample chamber is under vacuum so that the electrons can be emitted and detected without an interference by any gas molecules. Further information on SEM can be found in [Goldstein 2003].

If the specimen has little conductivity, the specimen might be sputter coated with a conductive layer of gold to obtain a better SEM image, since the electrons tend to be charged up on a non-conductive material, resulting in a white streaking noise on the image. The operation of the SEM is facilitated by associated software. The accelerating voltage and the emission current, which are the important parameters for the field emission gun, were set at 20 keV.

3.3.5 Transmission electron microscopy

In Transmission Electron Microscopy (TEM) a well focused high energy beam ($100 - 400$ keV) of electrons is transmitted through an ultra thin specimen, interacting with the specimen as it passes through. A schematic of a TEM is illustrated in Figure 3.10. The electrons that are elastically scattered form the transmitted beams, which pass through the objective lens. More signals can be detected in different types of TEM, like Bremsstrahlung X-rays (EDAX) or inelastically scattered electrons (EEIS) among others. The technique exploits the very small wavelengths of high-energy electrons to probe solids at the atomic scale. An image is formed from the interaction of the electrons transmitted through the specimen; the image is magnified and focused onto an imaging device. Further information on TEM can be found in [Williams 2009].

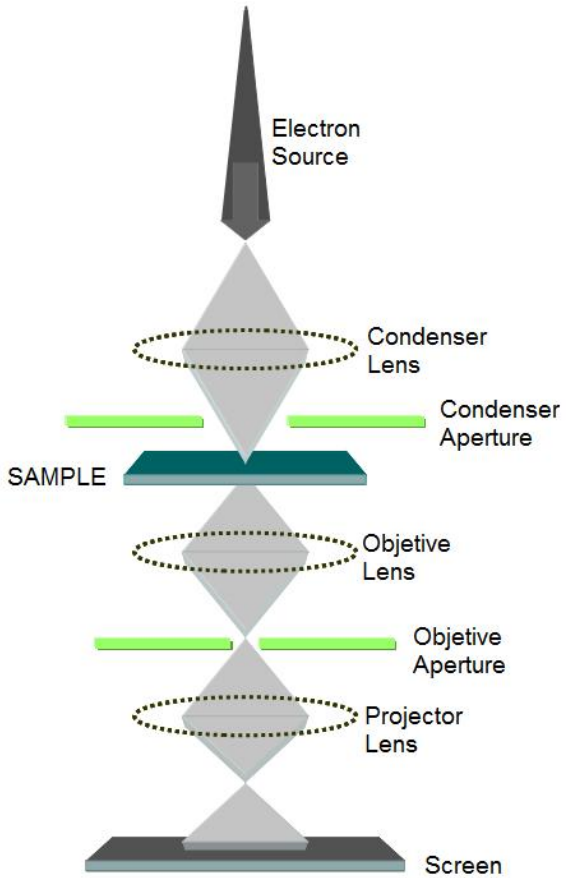

Figure 3.10: A schematic of a TEM

In TEM, the electrons in the beam are accelerated through a potential drop V, giving it a kinetic energy eV which must be equal the potential energy, thus

$$eV = \frac{m_0 v^2}{2} \tag{3.7}$$

then, for a given accelerating voltage of 200 KeV, the speed of the electrons in the beam reaches up to 80% of the speed of light.

Considering de Broglie's equation which describes the wave-particle duality, we can relate the particle momentum $m_0 v$ to its wavelength λ through Planck's constant

$$\lambda = \frac{h}{m v_0} \tag{3.8}$$

therefore, substituing for v from equation (3.7), the electron wavelength λ can be obtained as a function of the accelerating voltage V

$$\lambda = \frac{h}{(2m_0eV)^{1/2}} \tag{3.9}$$

According to this equation, the electrons wavelength can be controlled by the accelerating voltage applied. Figure 3.11 shows one of the samples prepared after ion milling, feautering a thickness less than 100 *nm* suitable for TEM observation.

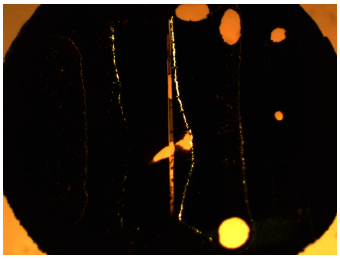

Figure 3.11: TiN/cement interface sample after ion-beam milling

3.4 Corrosion Studies

3.4.1 Polarization measurements

Corrosion mechanism has an electrochemical nature. During corrosion, two complementary processes occur over a single metallic surface anodic reaction

$$M \rightarrow M^{n^+} + ne^- \tag{3.10}$$

and cathodic reaction (in case of neutral and basic medium)

$$O_2 + 4H^+ + 2H_2O \rightarrow 4OH^- \tag{3.11}$$

The process is illustrated in Figure 3.12. When these reactions take place, the potential of materials is no longer at an equilibrium value. This deviation from equilibrium potential is called *polarization*. Electrodes can also be polarized by the application of an external voltage. The magnitude of polarization is usually measured in terms of overpotential η, which is a measure of polarization with respect to the equilibrium potential E_{eq} of an electrode. This polarization can be either anodic, when the anodic processes on the electrode are accelerated by changing the specimen potential in positive direction, or cathodic, when the cathodic processes are accelerated by moving the potential in negative direction. Overpotentials corresponding to the anodic and cathodic polarization are called *anodic* (η_a) and cathodic (η_c) overpotential, respectively. Overpotential can be expressed as follows: $\eta = E - E_{eq}$, where E is the applied potential [Wang 2006].

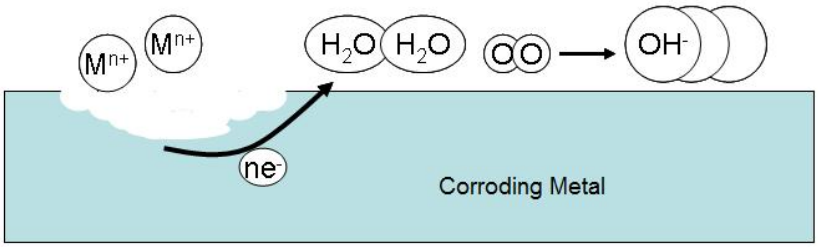

Figure 3.12: Simple model describing the electrochemical nature of corrosion processes

In a typical anodic or cathodic polarization experiment, a solution component is electrolyzed (oxidized or reduced) by placing the solution in contact with an electrode surface, and then imposing sufficiently positive or negative potential on that surface using a constant amplitude potential waveform to force electron transfer. In simple cases, the electrode surface is started at a particular potential with respect to a reference. The electrode potential is swept to a higher or lower value at a linear rate.

The electrochemical reactions of interest take place at the working electrode (WE). Electrical current at the WE due to electron transfer is termed as faradaic current. An auxiliary (AE), or 'counter' electrode is driven by a potentiostatic circuit to balance

the faradaic process at the WE with an electron transfer of opposite direction. The process at AE is typically not of interest, and in most experiments the small currents observed mean that the electrolytic products at AE have no influence on the processes at the WE.

During polarization, reduction and oxidation reactions on the surface of the metal produce a net electric current i. The sum of current density of these reactions depends on the overpotential η by the so-called Tafel equation:

$$\eta = a \pm b \log |i| \tag{3.12}$$

where b is known as Tafel slope of the anodic or cathodic potential respectively, so applied for the ± sign to be used. A plot of applied potential (or overpotential) versus logarithm of current density is called *Tafel* plot (Figure 3.13).

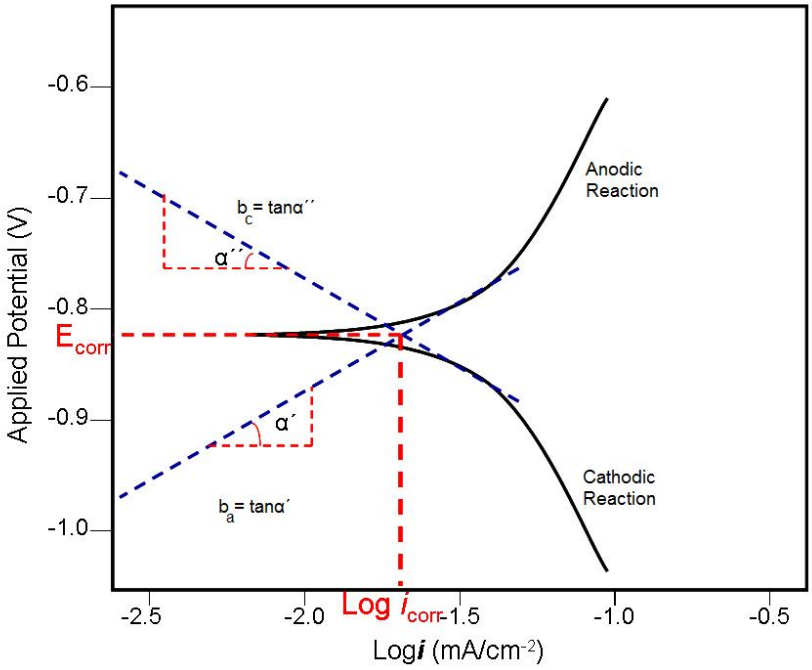

Figure 3.13: Schematic polarization curve showing Tafel extrapolation

The corrosion potential (E_{corr}) and corrosion current density (i_{corr}) can be ob-

tained by polarization measurements [Wang 2006]. The equilibrium open circuit potential (OCP) of an electrode can be considered as E_{corr}. Corresponding to E_{corr} is i_{corr} which is proportional to corrosion rate (C_R) and has inverse relation with polarization resistance (R_p) of the electrode as shown in the Stern-Geary equation

$$i_{corr} = \frac{b_a.b_c}{2.303(b_a + b_b)}.\frac{1}{R_p} \tag{3.13}$$

The values of E_{corr}, i_{corr} and Tafel slopes (anodic slope b_a and cathodic slope b_c) can be obtained by extrapolation from Tafel plots.

3.5 Photocatalytic Studies

3.5.1 Methylene blue degradation

Photocatalytic studies were carried out on selected samples. The photocatalytic activity of the materials was investigated by degrading a simulated organic pollutant (methylene blue). Methylene blue is one of the generally accepted organic pollutants for degradation studies and is used as an industrial standard (Japanese standard, JIS R 1703-2:2007).

Methylene blue was supplied by Sigma-Aldrich with 0.04% solution in water. Aqueous solution of methylene blue was prepared with deionised water up to a concentration of 72×10^{-6} M. TiO_2/cement samples were introduced in a cylindrical reaction cell used to follow the reaction solution, with a top optical window whose section area was ca. 11 cm^2, through which the suspension was irradiated. The photocurrent was measured by a specially made system composed of a chopped tungsten lamp with a monochromator (set at a wavelength of 665 nm), and a photodiode connected to a lock-in amplifier was used as detector. The UV-irradiation was provided by a high pressure 125 W deuterium lamp. The reliability of this tailor-made experimental setup can be

demonstrated by observing the Figure 3.14, where MB degradation for several samples was measured by means of transmitted photocurrent. In these plots, it can be seen that the photocurrent barely oscillates around a steady average value. All photocatalytic degradation experiments were carried out twice, and an average error of ±10% was calculated.

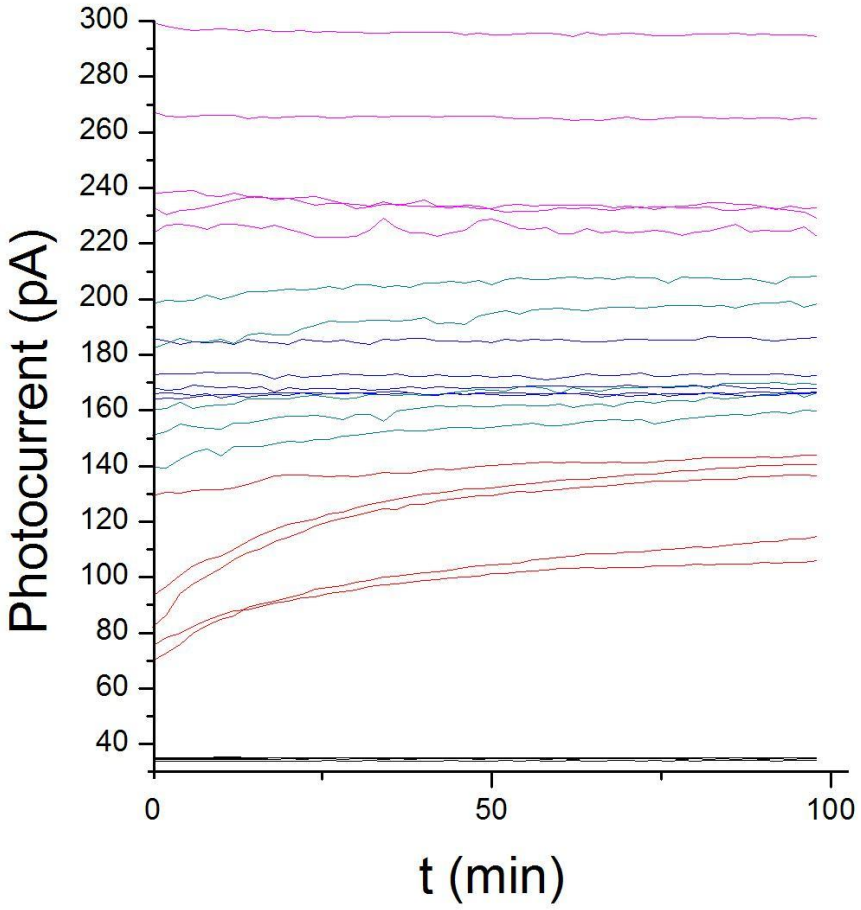

Figure 3.14: Transmitted photocurrent versus time for several samples. Measurements performed for the purpose of this thesis.

CHAPTER 4

Interface between Cement Paste and TiN Thin Film - Cement Side

---

This chapter presents an investigation on the cement side of the interface between TiN thin film and cement paste. TiN thin films prepared by magnetron sputtering have been evaluated as corrosion protective coatings for potential applications in concrete reinforcing steel. The cement side of the interface between the cement paste and the TiN thin film has been investigated at several curing temperatures by using XRD, TGA/TDG and SEM. The results show that the portlandite crystallites at the TiN-cement interface exhibit clearly preferred orientation with (001) plane parallel to the interface. The local increase in the water/cement ratio occurring at the interfacial zone promotes the formation of micrometric ettringite.

4.1 Introduction

This work presents an investigation of the interface between cement paste and sputter deposited TiN films for potential applications in corrosion protection of reinforcing steel. This reasearch focuses on the main reactions that occur with an increase of curing temperature in the cement paste and the TiN coating, as determined by a wide spectrum of techniques. In order to assess the concrete quality and its potential durability under service conditions, factors that affect microstructure, such as hydration

degree, curing temperature and characteristics of the hydration products at the interface between the cement paste and the TiN coating, are discussed.

4.2 Materials and Methods

4.2.1 Specimen preparation

TiN thin film prepared by Magnetron Sputtering as described in 3.1.2.2 and schematic in Figure 4.1, was divided into five 1 cm^2 pieces (one of them to be used as reference) and placed inside four cylindrical plastic moulds with dimensions of 23 *mm* inner diameter and 11 *mm* height. The cement paste prepared according to 3.2.1 was then cast into each mould. A schematic of the cylindrical plastic mould used for casting the cement paste is shown with dimensions in Figure 4.2, along with a photograph of one of the prepared samples.

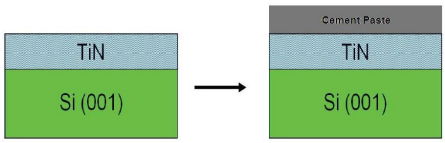

Figure 4.1: Process of TiN/Cement interface preparation

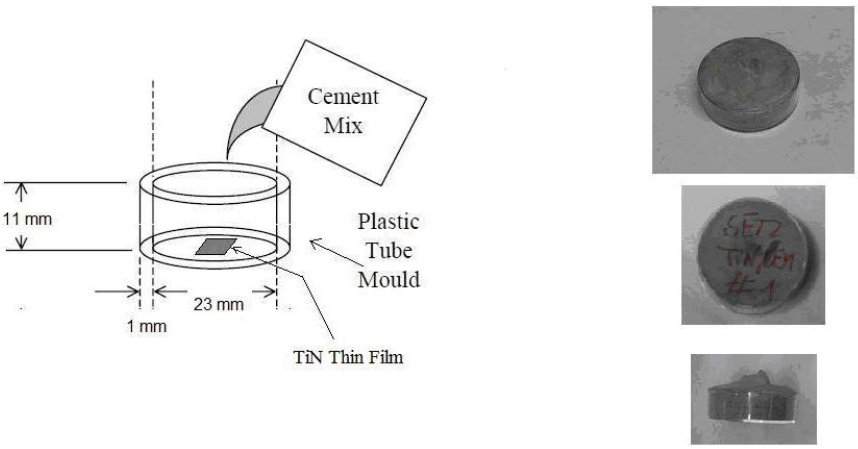

Figure 4.2: Sample for TiN/Cement interface studying

4.2.2 Curing

Cement samples were labeled with the prefix CEM(TiN) followed by the curing temperature to be applied, 20, 60, 90 and 120°C. The reference sample containing only the cement paste was labeled as CEM20. The curing conditions for sample CEM(TiN)20 and CEM20 were: 7 days in a curing chamber 20°C, relative humidity 98%). Sample CEM(TiN)60 was immediately introduced in a conventional furnace for 3 hours, at the regulated temperature of 60°C within an accuracy of ±1 °C. CEM(TiN)90 and CEM(TiN)120 were pre-cured for 24 hours and 48 hours respectevely, in the curing chamber 20°C and then introduced in turns into the furnace at their corresponding temperature for 3 hours. After the heating time, all specimens were stored in the curing chamber for 7 days.

After curing, the samples were demoulded and the thin TiN coating carefully separated from the hardened cement cylinders and labeled as TiN(cem) followed by the curing temperature. These TiN specimen will be analysed in the next chapter. The cement paste cylinders were sliced into discs with a height of approximately 2mm corresponding to the cement area which was in contact with the TiN layer. These discs were then trimmed to leave the cement paste which had been in contact with the TiN. Table 4.1 summaries the experimental conditions for the specimens.

Cement Side	Sample ID	Time prior Curing	Curing Time	Curing Temperature (°C)	Total Hydration Time
	CEM20	-	-	20	7 days
	CEM(TiN)20	-	-	20	7 days
	CEM(TiN)60	4 min	3 hours	60	7 days
	CEM(TiN)90	24 hours	3 hours	90	7 days
	CEM(TiN)120	48 hours	3 hours	120	7 days

Table 4.1: Experimental conditions for the samples prepared.

4.2.3 Characterization methods

X-Ray diffraction (XRD) was performed on the cement paste samples in a Siemens diffractometer using Cu K_α radiation in $\Theta/2\Theta$ configuration with 0.02°scan step and $6s$ integration time. The phase identification was first obtained by using the Match! Software version 1.10 together with the JCPDS database.

The TGA experiments were conducted using TA Instruments, Q500 and Q100. Prior to testing, a specimen was immersed in isopropyl alcohol for 1 day to stop hydration at a desired hydration period and it was then dried to air for 1 day to remove the isopropyl alcohol from the system. The temperature was ramped from room temperature to 900°C at 10°C/min with a 100 ml/min nitrogen gas flow. The analysis was conducted by the TA Instruments Universal Analysis V4.2E. The morphology was observed with a HITACHI S-3000N Field Emission Scanning Electron Microscope operating at 20 KeV operating voltage, and also equipped with an energy dispersive X-ray spectrometer (EDS). Both the cement paste samples and TiN specimens were gold coated before observation. TiN samples were observed in direct and cross section.

4.3 Results and Discussion

4.3.1 Phases identification

The XRD diagrams corresponding to cement paste TiN thin film interfacial zone are shown in Figure 4.3. All samples present the characteristic peaks of portlandite $Ca(OH)_2$ (JCPDS 01-076-0571) and the most intense peak of calcite $CaCO_3$ (JCPDS 04-012-8072), both with a diffraction peak intensity distribution that appears slightly modified as a function of curing temperature. The formation of calcite within the samples comes either from the CaO content of the clinker or from the reaction between $Ca(OH)_2$ and atmospheric CO_2. Samples cured at ambient temperature also present characteristic strong low-angle peak of ettringite (101) (JCPDS 00-041-1451), which

is also observed in the specimen cured at 60°, disappearing at higher temperatures. Only sample CEM(*TiN*)60 presents the characteristic peaks of gypsum (JCPDS 04-010-9409), which reveals the consequences of thermal shock causing hydration interruption in that specimen. The same fact can explain the presence of high intensity peaks in the CEM(*TiN*)60 sample corresponding to calcite, as well as some anhydrous phases - calcium and aluminate silicates - whose peaks appear within the 32-33°region, overlapping each other and therefore being difficult to differentiate.

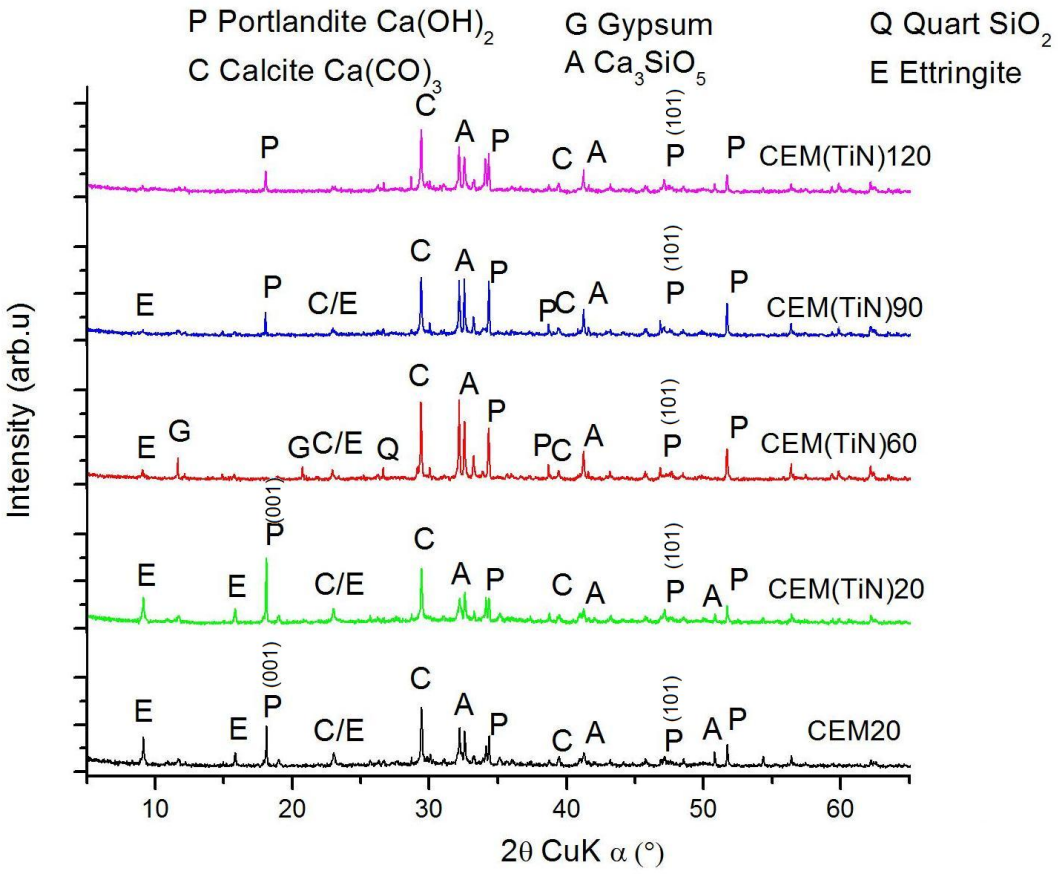

Figure 4.3: XRD diagrams corresponding to CEM20 reference and *TiN*/cement paste samples varying curing temperature

Portlandite crystals show better crystallization in samples CEM(*TiN*)20 than in the reference sample, cured without *TiN* contact, as the peak corresponding to (001) is observed to be higher in those samples. Samples cured at 60 and 90°C show high in-

tensity peaks corresponding to portlandite (110) (at 51°) and calcite (104) (30°), while CEM(TiN)120 samples show these peaks with significantly lower intensity. This confirms the previously observed fact [Castellote 2004] that upon heating up to 100°C, portlandite and calcite formation seem to be favoured. This may be explained by the precipitation caused by the loss of free water in the paste pores, as well as the additional release of Ca^{2+} coming from the decomposition of ettringite, which completely disappeared at 90°, as can be noticed in CEM(TiN)90 samples.

4.3.2 Orientation of calcium hydroxide crystals at the interface

The texture of the cement hydrates at the TiN/cement paste interface and orientation of portlandite crystals was evaluated from XRD spectra as the one shown in Figure 4.3. From a preliminary analysis of the intensities of the peaks corresponding to different crystalline planes, it is observed that in the samples cured on TiN film at 20°C, CEM(TiN)20, the peak corresponding to (001) plane presents a clearly higher intensity than the same peak in the CEM20 sample cured at identical temperature but without TiN contact. This indicates, firstly, a higher nucleation of crystalline calcium hydroxide on the surface of the TiN film, which can be attributed to a local increase of the water/cement ratio and therefore favorable migration of Ca^{2+} ions, promoting $Ca(OH)_2$ crystal formation. Secondly, the previously reported fact of preferred orientation of portlandite crystals at the aggregate/cement paste interface [Larbi 1990], seems to show evidences in the present work. The former mentioned diffraction peak for portlandite can also be observed in samples steadily cured at higher temperatures, 90 and 120°C, although less intense and broader peaks, indicating poorer density of portlandite crystals at higher temperatures. In this sense, the $Ca(OH)_2$ pattern does not strongly correspond, however, to the sample CEM(TiN)60, which underwent thermal shocking and therefore only scarced hydration products were allowed to be formed.

To quantitatively analyse the preferred orientation at the interface between cement paste and the TiN coating, the orientation index of $Ca(OH)_2$ was calculated

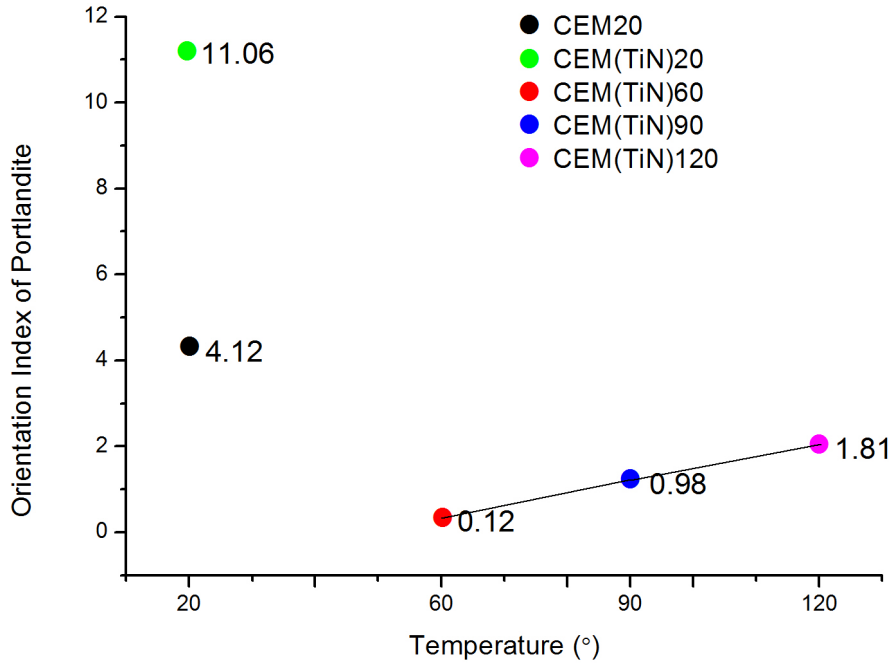

Figure 4.4: Orientation index of portlandite in the samples

for each specimen, according with the model exploited by Yue et Al. [Yue 2001] on steel/cement paste interface, already used by other authors when studying portlandite orientation factors on cementitious systems. Based on the cited work, the orientation index can be calculated from

$$I_{CH} = \frac{I_{(001)}/I_{(101)}}{0.74} \tag{4.1}$$

where $I_{CH} > 1$ indicates preferential orientation of the $Ca(OH)_2$ crystals, with their (001) planes parallel to the interface. Results are depicted in Figure 4.4, showing the plane (001) to be preferential with respect to (101) at the cement/TiN interface. This effect has been previously observed in the interfacial transition zone between the aggregate and the cement paste, where portlandite crystals tend to precipitate with a preferred orientation near the aggregate [Detwiler 1988] [Monteiro 1985]. The index of orientation reaches higher values in samples cured at ambient temperature, being remarkably

larger for the cement paste cured on TiN surface. For the samples cured at higher temperatures, it is observed that the orientation index increases with temperature.

4.3.3 Thermal analysis

In order to qualitatively evaluate the oxide passive layer formation in the coating, the calcium hydroxide content of the cement pastes was determined from the step observed in the TDG curves between 425°C and 450°C, using the procedure reported by Taylor [Taylor 1997] and Bland et al. [Bland 1990]. The results obtained from TGA/TGD for the different specimens are presented in Figure 4.5, where the mass loss(as a percentage of the weight of the sample) is depicted versus temperature.

Table 4.2 shows the relative weight loss of each sample during the main inflections detected in the corresponding DTG curves. Following the temperature ranges considered in [Alarcon-Ruiz 2005], the mean decomposition reactions occurring:

- 25-100°C: evaporation of surface absorbed water, as generally accepted, volatile water and part of bound water takes place in this range. The weight losses during this range for samples cured at ambient temperature appear to be higher than that for the rest of the samples, showing larger water content in samples not submmited to thermal treatment, as expected.

- 100-200°C: decomposition of gypsum and ettringite occurs within this range [Łatava 1975], [Paulik 1992]. Also C-S-H partial dehydration takes place at 180-200°C [Taylor 1997]. From Fig.4.5 observation, all samples present an endothermic peak at around 120°C, indicating C-S-H presence in the samples. Weight loss in samples CEM(TiN)60 is lower in this temperature range, indicating a lower presence of C-S-H due to the thermal shock and short hydration time. Among samples cured at higher temperatures, CEM(TiN)120, shows the largest weight loss within this range, which corresponds to the fact that this samples were allowed to hydrate at ambient temperature for longer time before it was introduced

in the furnace.

- 200-450°C: C-S-H gel and calcium aluminate hydrates lose their bound water and dehydration of both phases occurs [Vedalakshmi 2003]. The behaviour of the samples within this range of temperature is similar to the one shown in the previous interval; again the presence of hydrates in the pastes produces weight loss upon heating.

- 450-625°C: dehydroxylation of portlandite occurs at 460-475°C [Zelic 2002]. No more thermal induced reactions occur within this range of temperatures. Therefore, calcium hydroxide content in the samples can be analyzed from the weight loss values. Estimated portlandite content is depicted in Fig.4.6 (a). As previously observed from XRD patterns, the larger amount of $Ca(OH)_2$ in sample CEM(TiN)20 than in reference sample, has been confirmed from the TGA/TDG analyses, which suggests that the interface between cement paste and TiN favours growth and nucleation of portlandite crystals.

- 625-750°C: decomposition of calcite - calcium carbonate - takes place at around 730-740°C [Dweck 2000]. From observation of TGA/TDG diagrams, also confirmed by the XRD spectra, sample CEM(TiN)60 appears to have the largest amount of calcite, despite all samples being made of the same clinker and thus the CaO addition was identical for each one. This indicates that the gas-solid carbonation of portlandite particles seems to be catalyzed by the high water actitivy produced from the initial increase of water/cement ratio at the interface TiN/cement, along with the moderately high temperature [Montes-Hernandez 2010], in atmospheric CO_2 pressure conditions.

The degree of hydration in the cement paste interfacial zone was estimated from TGA values by the empirical calculation of chemically bound water and CO_2 desorption. It can be assumed that the degree of hydration of a cement paste is directly proportional to the amount of chemically bound water present [Guirado 1998]. The combined

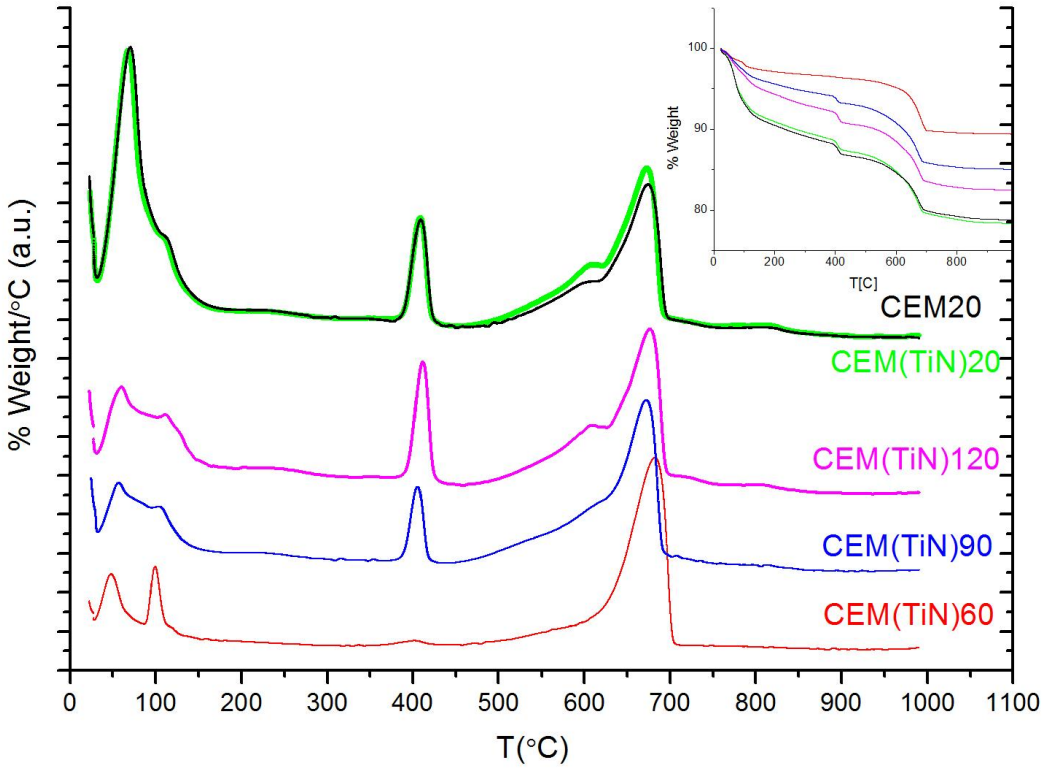

Figure 4.5: TGA/TDG diagrams corresponding to CEM20 reference and the TiN/cement paste samples cured at different temperatures

	Temperature (°C)					
Sample ID	25-100	100-200	200-450	450-625	625-750	750-1000
CEM20	6.742	2.728	3.813	2.856	4.313	0.743
CEM(TiN)20	6.432	2.586	3.729	3.427	4.615	0.864
CEM(TiN)60	1.518	1.305	0.860	1.590	5.082	0.211
CEM(TiN)90	2.786	1.628	2.470	3.214	4.397	0.511
CEM(TiN)120	3.235	2.324	3.662	3.071	4.494	0.617

Table 4.2: Relative weigth loss (%) of reference sample and TiN/cement specimens upon heating

water can be considered to be completely eliminated from the sample when heating from 105°C up to 900°C [Taylor 1997], due to the descomposition of carboaluminate hydrates and the C-S-H. At lower temperatures, typically from 30°C up to 105°C, the evaporable water is lost, and still there is a small but not significant part of bound water that escapes. In the work presented here, TGA data have been used to determine the chemically bound water from the difference between the sample weight at 105°C and its weight after heating at 900°C, minus the mass loss due to CO_2 desorption produced by the calcite decomposition, which occurs between 600°C and 800°C. The degree of hydration of the cement paste at a given hydration time t, can be calculated by the following expression [Mounanga 2004]:

$$\alpha_{TGA}(t) = \frac{(W_{105^\circ} - W_{900^\circ}) - (W_{600^\circ} - W_{800^\circ})}{W_C \frac{W_n^0}{c}} \tag{4.2}$$

where W_C is the initial anhydrous cement mass of the sample. The ratio W_n^0/c introduces the influence of the drying process used in the experiment, which varies between 0.18 and 0.26. This fraction qualitatively expresses the relation between the bound water in the cement sample when is fully hydrated, and the cement content in the sample, providing there are no air pores. This value is estimated from the mineralogical composition of cement (according with Bogue's formulae [Bogue 1929] and [Czernin 1980]), and used as $W_n^0/c = 0.2293$.

Figure 4.6 (b) depicts the calculated values for each specimen. Both samples cured at ambient temperature present a higher degree of hydration than those submitted to thermal treatment, with the higher value obtained for sample CEM(TiN)20 compared to the reference sample CEM20, cured without TiN contact. This is in fact expected, due to the local increase of water/cement ratio in the interface between cement paste and TiN film. The hydration degree for samples cured at higher temperature is smaller than samples cured at 20°C, especially for the sample submitted to thermal shock, due to the interruption induced on hydration. Nevertheless, the degree of hydration increases with

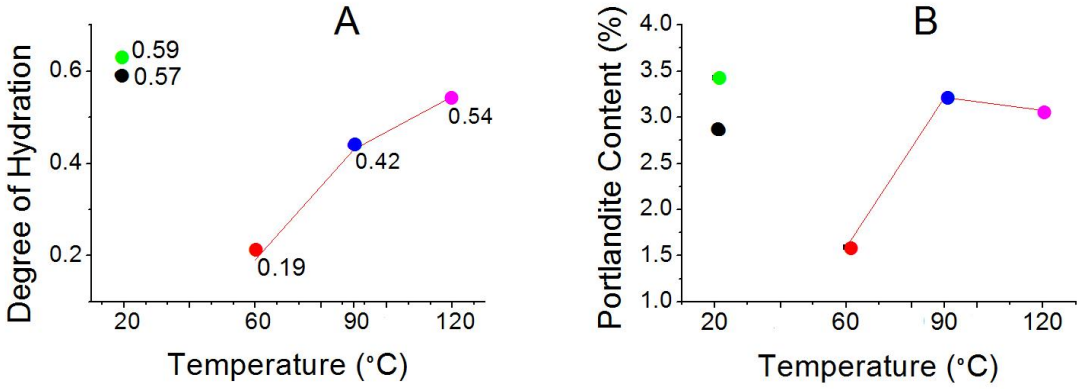

Figure 4.6: (a) Estimated portlandite content in the samples and (b) degree of hydration after 7 days curing time for each sample

an increase of temperature, as can be noticed in samples CEM(TiN)60, 90 and 120. This is in agreement with what was published elsewhere for Portland cement pastes and alternative cement systems [J.I 2003]. The lowest degree of hydration corresponds to the sample CEM(TiN)60 that underwent thermal shocking, which implies a significant and sudden decrease of the water/cement ratio.

4.3.4 SEM observations

SEM microscopy was performed on the cement paste surfaces cured in contact with the TiN thin films, providing valuable information on the morphology of the hydration products formed on the TiN interface. Figure 4.7(a) shows the microstructure of CEM20 reference sample, which corresponds to a typical middle stage of hydration: large regions of dense C-S-H gel deposited along with portlandite macrocrystals. Acicular crystals of ettringite of about 10μm-long can be distinguished among the hydration products. In Figure 4.7(b) the microstructure of CEM(TiN)20 samples can be observed. In this case fibrous C-S-H gel layers are formed interconnecing numerous portlandite micrometric crystals of plate morphology, which appear to have a preferential orientation. These observations suggest $Ca(OH)_2$ enrichment in the interface TiN/cement,

of which both X-ray diffraction and thermal analysis have provided evidence as well. Similar results were obtained by other authors from a number of studies on the interface between steel and cement paste [Zayed 1992], generally concluding that the interface is largely composed of portlandite, and therefore there is a larger amount of $Ca(OH)_2$ formed at the steel-cement interface than in the bulk cement paste. From the results presented herein, the effect of TiN-coating eventually presented on reinforced concrete is also very likely to promote this desirable passive layer formation, including the feature of containing preferentially aligned $Ca(OH)_2$ microcrystals.

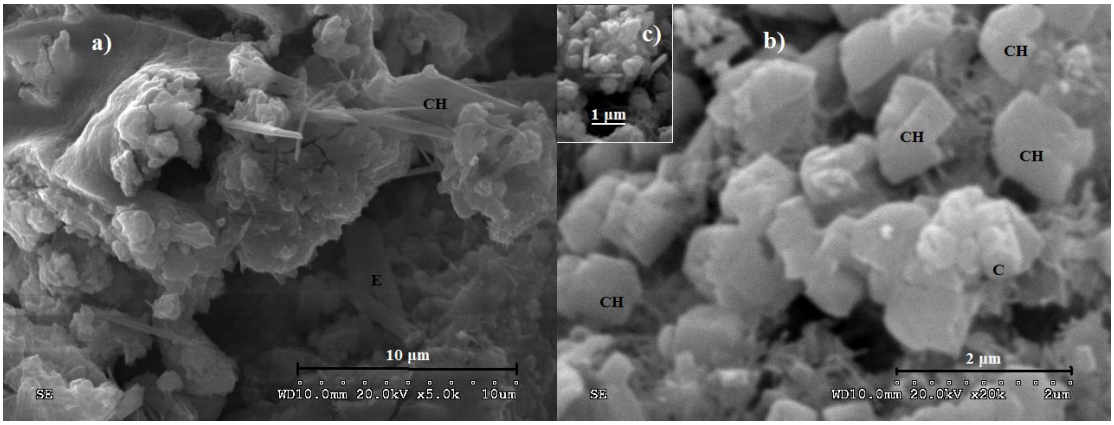

Figure 4.7: SEM micrographs of (a) CEM20 and (b) CEM(TiN)20 samples, featuring: a) dense C-S-H with portlandite crystals (CH) and acicular attringite (E), b) fibrous C-S-H, portlandites plateous (CH), calcite clusters (C) and needles of ettringite (E). (c) Detail of ettringite crystals of length $1-2\mu$ m, in samples CEM(TiN)20

Comments on ettringite morphology differences can be derived from the SEM analysis. The microstructure of CEM(TiN)20 samples includes needle-shape ettringite crystals of $1-2\mu$m length, as detailed in Figure 4.7(c), through fewer and smaller than those observed in the reference sample. This effect can be explained either by the presence of a large content of $Ca(OH)_2$, that reduces the formation and the size of the ettringite crystals [Mehta 1976]. These findings have been also detected in the interfacial zone between aggregates and cement paste, where small-sized ettringite formation have been widely observed, (being Heinz and Ludwig [Heinz 1986] the pioneers). In any case, one important factor has to be pointed out: there is no thermal treatment associa-

tion with the crystallisation of ettringite observed in Fig.4.7 (both samples were cured at low temperature), therefore the remarkably different size of the ettringite crystals in the studied samples might be held as a result from the presence of TiN coating.

4.4 Conclusions

The interface between TiN thin film and cement paste has been reported for the first time. The following remarks can be concluded regarding the cement side:

- The cement paste analysis presented here confirms that upon heating up to 100°C, portlandite and calcite formation seem to be favoured. This may be explained by the precipitation caused by the loss of free water in the paste pores, as well as the additional release of Ca^{2+} coming from the decomposition of primary ettringite.

- Portlandite crystals show better crystallization in the cement paste cured on the TiN thin film, which can be attributed to a local increase of the water/cement ratio at the interface and therefore favorable migration of Ca^{2+} ions, promoting $Ca(OH)_2$ crystal formation. Thus it can be concluded that the effect of TiN-coating on the reinforced concrete is highly likely to promote the desirable passive layer formation.

- The higher nucleation of $Ca(OH)_2$ on the surface of the TiN film, features a preferred orientation Features a preferred orientation with respect to the plane of the interface with TiN, being the plane (001) preferential with respect to (101) at the cement/TiN interface. The index of orientation was found to decrease when higher than ambient temperature was applied to cure the cement paste,which suggests that a critical temperature of anchorage release must be reached so that the crystallites can move under a frictional force related to interfacial viscosity. Further increase in temperature results in an increase of the orientation index of

portlandite crystals, which might imply that thermally activated rotation of portlandite crystallites is possible under further annealing.

- Modification of the curing temperature also affects the degree of hydration of the overall system, which increases with higher temperature. When curing temperature is 20 °C, the degree of hydration of cement in the interface with TiN is clearly larger than that of cement cured without contact with TiN, which suggests that TiN contact promotes the formation of hydration products by locally incrementing the cement/water ratio in the interfacial zone.

- SEM analysis shows that needle-shape ettringite crystals of $1 - 2\mu$m length are formed in the interface between cement and TiN, rather fewer and smaller than those observed in cement paste cured without TiN contact. This effect can be simply explained either because of the large content of $Ca(OH)_2$, that reduces the formation and the size of the ettringite crystals. There is no thermal treatment association with these reduced-sized crystallisation of ettringite observed. Therefore, this fact might only be held as a result from the presence of TiN coating.

CHAPTER 5

Interface between Cement Paste and TiN Thin Film - TiN Side

This chapter presents an investigation on the TiN side of the interface between TiN thin film and cement paste. TiN thin films prepared by magnetron sputtering have been evaluated as corrosion protective coatings for potential applications in concrete reinforcing steel. The interface between the cement paste and the TiN at several curing temperatures has been investigated by XRD, XPS, SEM and HRTEM. Cyclic Voltammetry (CV) in a chloride buffer has been applied to establish the corrosion resistance modification of the nitride coatings. Evidence of a nanocrystalline C-S-H phase has been found on the TiN coating, arranged in clusters. Electrochemical measurements reveal that TiN coatings show a superior corrosion behaviour after cement paste setting.

5.1 Introduction

This work presents an investigation of the interface between cement paste and sputter deposited TiN films for potential applications in corrosion protection of reinforcing steel. It focuses on the main reactions that occur with an increase of temperature in the cement paste and the TiN coating, as determined by a wide spectrum of techniques. The corrosion resistance of the nitride samples after cement setting is evaluated by the Tafel polarization and electrochemical cyclic voltammetry.

5.2 Materials and Methods

5.2.1 Specimen preparation

TiN films used in this work were obtained by following the method described in the previous chapter 4.2.1. Table 5.1 summaries the experimental conditions for the *TiN* specimens.

TiN Side	Sample	Heating Time	Heating Temperature (°C)
	TiN	Reference	Reference
	TiN(cem)20	-	20
	TiN(cem)60	3 hours	60
	TiN(cem)90	3 hours	90
	TiN(cem)120	3 hours	120

Table 5.1: Experimental conditions for the samples prepared.

5.2.2 Characterization methods

5.2.2.1 XRD

The diffratometrer X'Pert PRO of Panalytical was used for the XRD tests performed for this chapter. X-Ray diffraction (XRD) at grazing incidence was performed on the on *TiN* samples, with a incidence angle of 1.5°. The phase identification was first obtained by using the Match! Software version 1.10 together with the JCPDS database.

5.2.2.2 XPS

For XPS analysis specimens were mounted on the sample holder (SS-bar) using a UHV compatible (Si free) copper double side adhesive tape. All sample handling was done using nitrile powder free gloves. XPS measurements have been performed with an AXIS ULTRA Spectrometer (KRATOS Analytical, UK). Instrument calibration was performed using a clean pure Au/Cu sample and pure Ag sample (99.99%). Measured

values for electron binding energies (BE) were 84.00 ± 0.02 eV, and 932.00 ± 0.05 eV. The samples were irradiated with monochromatic $AlK\alpha$ X-rays ($h\nu$ = 1486.6 eV) using X-ray spot size of 400 × 700 m^2 and a take off angle (TOA) of 90°with respect to the sample surface. The base pressure of the instrument was better than 7×10^{-9} $Torr$ and the operating pressure better than 4×10^{-9} $Torr$. Surface charging was compensate by means of a filament (I = 1.9A, 3.6 V) inserted in a magnetic lens system and all spectra were corrected by setting the $C1s$ hydrocarbon component to 285.00 eV.

For each sample, a survey spectrum (0 − 1150 eV) - from which the surface chemical compositions (at%) were determined - was recorded at pass energy of 160 eV. In addition one set of high-resolution spectra (PE = 20 eV) was also recorded for each sample. The data were processed using the Vision2 software (Kratos, UK) ND Casa XPS v 3.16 (Casa software, UK). Sample compositions were obtained from the survey spectra after linear background subtraction and using the RSF (Relative Sensitivity Factors) included in the software derived from Scofield cross-sections. This method is estimate to give an accuracy of 10% in the measurement of elemental compositions.

5.2.2.3 SEM

The morphology was observed with a Hitachi S-3000N SEM operating at 20 KeV accelerating voltage, and also equipped with an energy dispersive X-ray spectrometer (EDS). TiN specimens were gold coated before observation. TiN samples were observed in direct and cross section.

5.2.2.4 HRTEM

Cross-sectional TiN/cement samples for transmission electron microscopy (TEM) were prepared by sectioning and fixing in a titanium frame with an araldite-graphite mixture cured at 180°C. Mechanical polishing was applied in a first step using gradual silicon carbide grits (20, 10, 5 − 10 μm particle size) until a thickness of 50 μm was reached. Finally, the samples were etched in an ion beam mill using a Balzers RES-

010 system. A JEOL JEM-3000F HRTEM operating at 300 keV accelerating voltage was used to analyse the specimens. Electron diffraction patterns were obtained by the selected area method (SAED). Image processing of the high-resolution images was carried out using Gatan Digital Micrograph and ImageJ software.

5.2.3 Corrosion measurements

Corrosion measurements were performed on the TiN samples by cyclic voltammetry experiments carried out in SP-150 potentiostat system together with EC-Lab V.10 software. Chemical cell configuration was a typical three-electrode setup. The working electrode was constituted by the specimens under study (area $\simeq$1 cm2), the counter and reference electrode being made of platinum. The current vs potential recordings, have been performed in 0.6 $M\ NaCl$ solution in a potential range between $-0.9\ V$ to $+0.9\ V$ with a scan rate of 10 mV/sec. With this method, a periodic potential change is applied in the system and the electric field intensity is swept back and forth between two fixed values, one or many times, at a constant rate, while the current is continuously measured.

5.3 Results and discussion

5.3.1 X-Ray diffraction

The XRD diagrams corresponding to TiN/Si(100) and hydrated cement/TiN/Si(100) are presented in Figure 5.1 (a). All the films present the characteristic peaks of TiN (JCPDS 38-1420) with a diffraction peak intensity distribution that was slightly modified as a function of the thermal treatment during the curing of cement. No obvious evidences of impurities such as metallic titanium, titanium oxides, other titanium nitrides, can be found in this XRD pattern.

The (200) peak presents remarkably higher intensity than the peak corresponding to the planes (111), which has also been observed in films deposited under the same magnetron sputtering conditions [Punzon-Quijorna 2011], displaying a strong preferred (200) orientation parallel to the substrate surface. The position of (200) peak is consistent with the value reported in literature, centered at 42.596°; while the peaks corresponding to the planes (111) and (220) appear to be displaced towards lower angles. The distortions in the patterns can be interpreted in terms of stress accumulation in the films, due to the significantly different thermal expansion coefficient between cement and TiN. The coeficient of thermal expansion for 7 day-cured cement is about 30-40×10^6/°C [Maruyama 2011], while TiN exhibits a value of 6.8×10^6/°C for the mentioned coefficient [C.R. 1964].

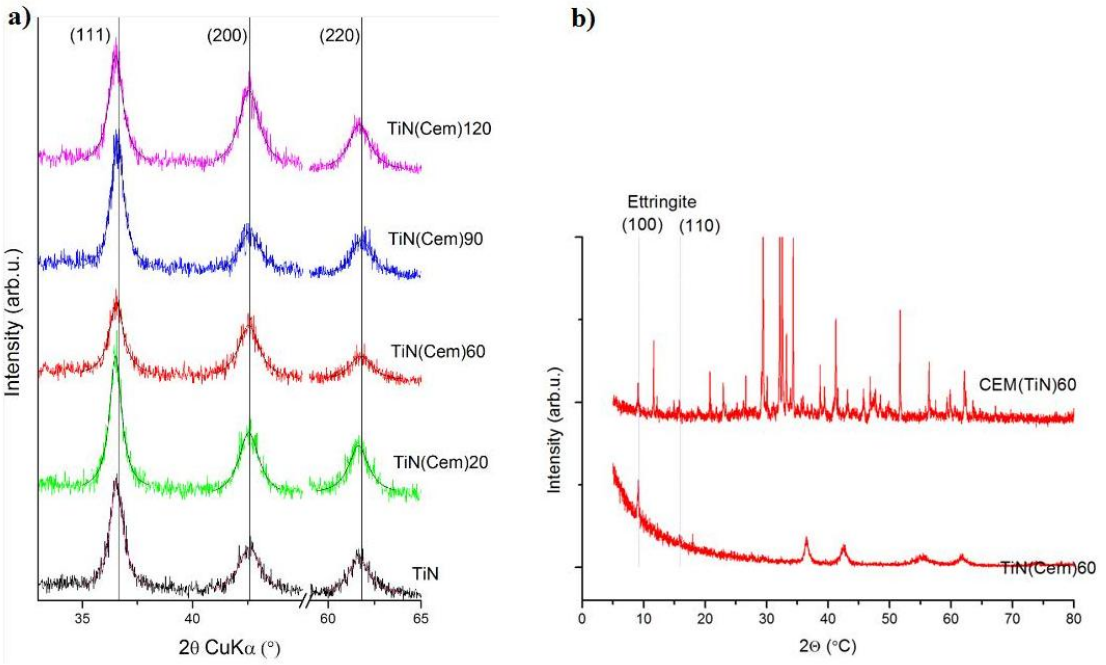

Figure 5.1: (a) XRD spectra of TiN reference and TiN(cem) coatings varying curing temperature, analysed in grazing incidence alignment with incidence angle of the primary X-ray beam of 1.5°. (b) Full spectra of TiN(cem)60 coating and CEM(TiN)60 sample, both featuring crystalline ettringite

5.3.2 XPS analyses

Curve fitting of core level peaks was carried out using the same initial parameters and inter-peak constrains to reduce scattering. The core level envelopes were fitted with Gaussian-Lorentian function (G/L=30) and variable full width half maximum. In the case of $Ti2p$ the peak area of the $2p_{1/2}$ component was constrained to be 0.5 times that of the correspondent $Ti2p_{3/2}$ component, whilst the FWHM parameter was unconstrained. The results of the quantitative analysis are reported in Table 5.2, whilst Figures 5.2-5.5 report the $Ti2p$, $Ca2p$, $O1s$ and $C1s$ core level spectra.

Sample ID	C	O	Ti	N	Ca	Si	S	Other (Sn, Cl)
TiN	41.9(0.9)	27.5(0.6)	11.9(0.3)	14.0(0.3)	0.2(0.03)	3.1(0.3)	0	0
TiN(cem)20	39.1(1.2)	34.6(1.9)	7.6(1.6)	165.68.5(0.5)	1.4(0.2)	2.7(0.2)	0	4
TiN(cem)60	28.2(0.9)	40.1(0.6)	10.6(0.9)	11.2(0.2)	4.8(0.3)	1.6(0.2)	1.4(0.3)	<1
TiN(cem)90	62.2(0.6)	23.6(0.7)	2.3(0.3)	2.6(0.5)	2.1(0.1)	6.6(0.6)	0.5(0.4)	<1
TiN(cem)120	58.6(2.3)	27.3(1.8)	2.7(0.2)	3.1(0.2)	4.3(0.1)	3.5(0.4)	0.5(0.2)	<1

Table 5.2: Chemical composition (at%) of different samples. ($AlK\alpha$ mono source, 90°TOA; Stddev in brackets)

From the quantitative analysis it can be seen that the TiN reference sample is strongly contaminated with carbon. Moreover the presence of a high level of oxygen reveals the formation of Ti oxides and oxynitride. This is confirmed by the analysis of the $Ti2p$ core level spectra (Figure 5.2 (A)). In fact three components are identified at about 455 eV, 456 eV and 458 eV that can be attributed to TiN, $TiOxNy$ and $TiOx$, respectively.

The different treatments induce as most remarkable issue a nucleation of Ca compounds, with a maximum of about 5% in sample TiN(cem)60. The intensity of Ti and N peaks decrease strongly in samples TiN(cem)90 and TiN(cem)120, where a notable increase of C content is also noticed. This may indicate a preferential nucleation of Ca in the form of calcite in these interfaces. It should be also underlined the presence of silicon in all samples (up to a maximum of 7%). The sample TiN(cem)60 contains also sulfur, which may be related to the nucleated ettringite crystals detected by XRD.

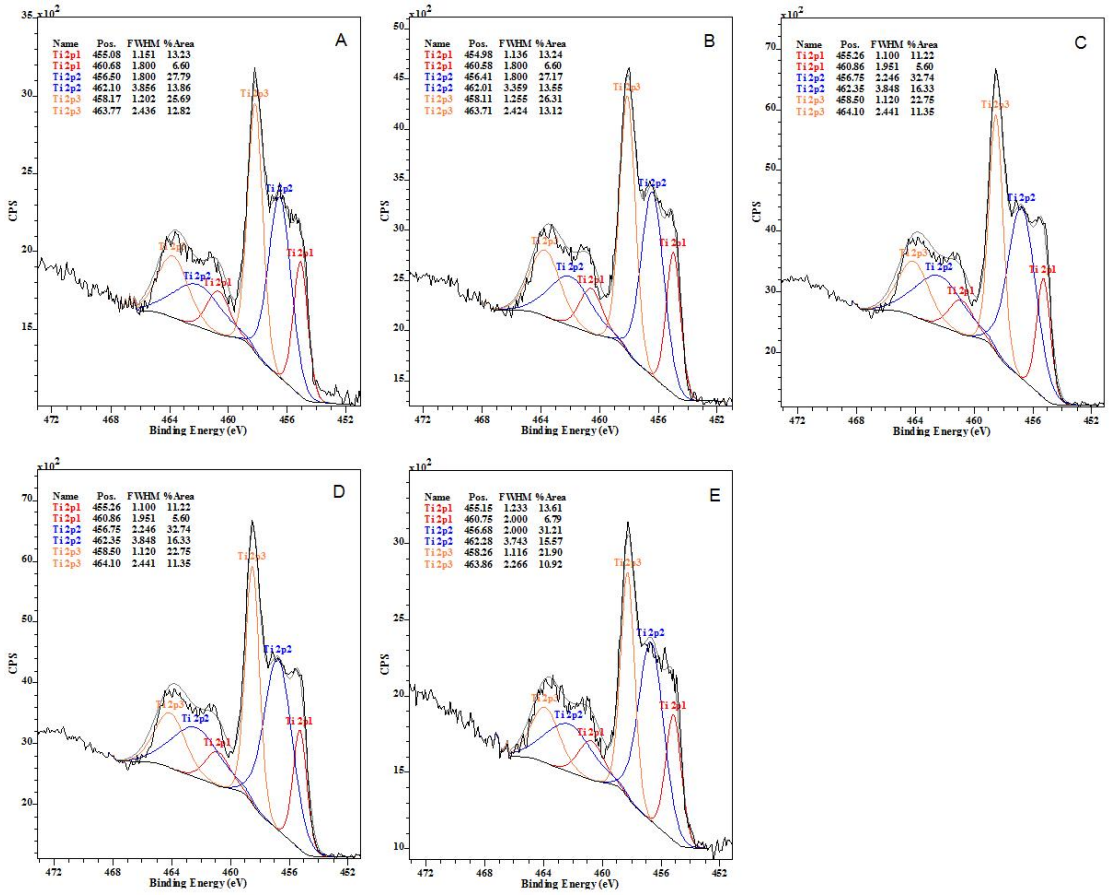

Figure 5.2: $Ti2p$ core level spectra of TiN reference sample (A) and $TiN(cem)20-120$ (B-E)

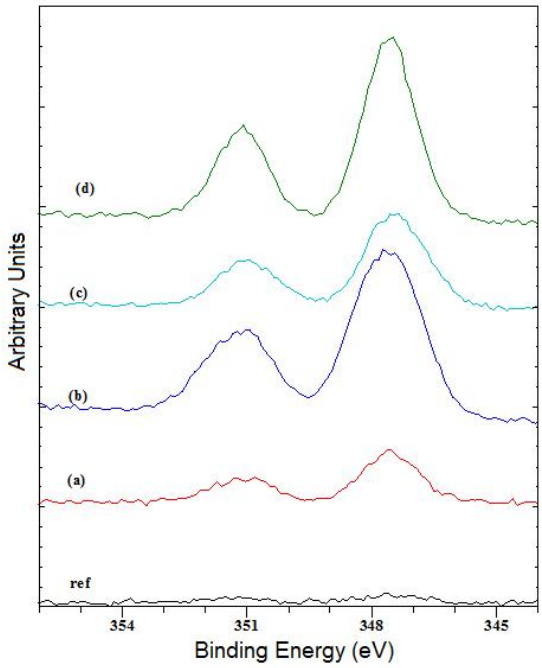

Figure 5.3: $Ca2p$ core level spectra of all samples

For all samples, the $O1s$ core level spectra reveals two components at about 530 eV and 532 eV, attributable to TiN(O,C) and $C-O(N)$, respectively. After the treatment the component at lower binding energy decreases due to the formation of an overlayer rich in Ca and C. The $N1s$ core level spectra (not shown) indicate the presence of a major component at about 398 eV and a minor component at about 396 eV that can be assigned to TiN(O) and TiN, respectively. Moreover, a small component at about 399 eV is also observed in the TiN reference sample indicating the presence of $C-N(O)$ bonds at the surface. The nitrogen content decreases with the treatment (as for the Ti) due to the formation of the overlayer. Regarding the stability of the TiN interface material to the treatments, the $N1s$ peak does not show any additional component after the treatments. However, the Ti component related to TiN decreases with the treatment (Figure 5.2 (B)-(E)) whilst the components related to titanium oxynitride and titanium oxide increase. This may indicate a potential help from the treatment to the conversion of the TiN into oxynitride and oxide. However to obtain a better picture a new study after an Ar ion etching is required.

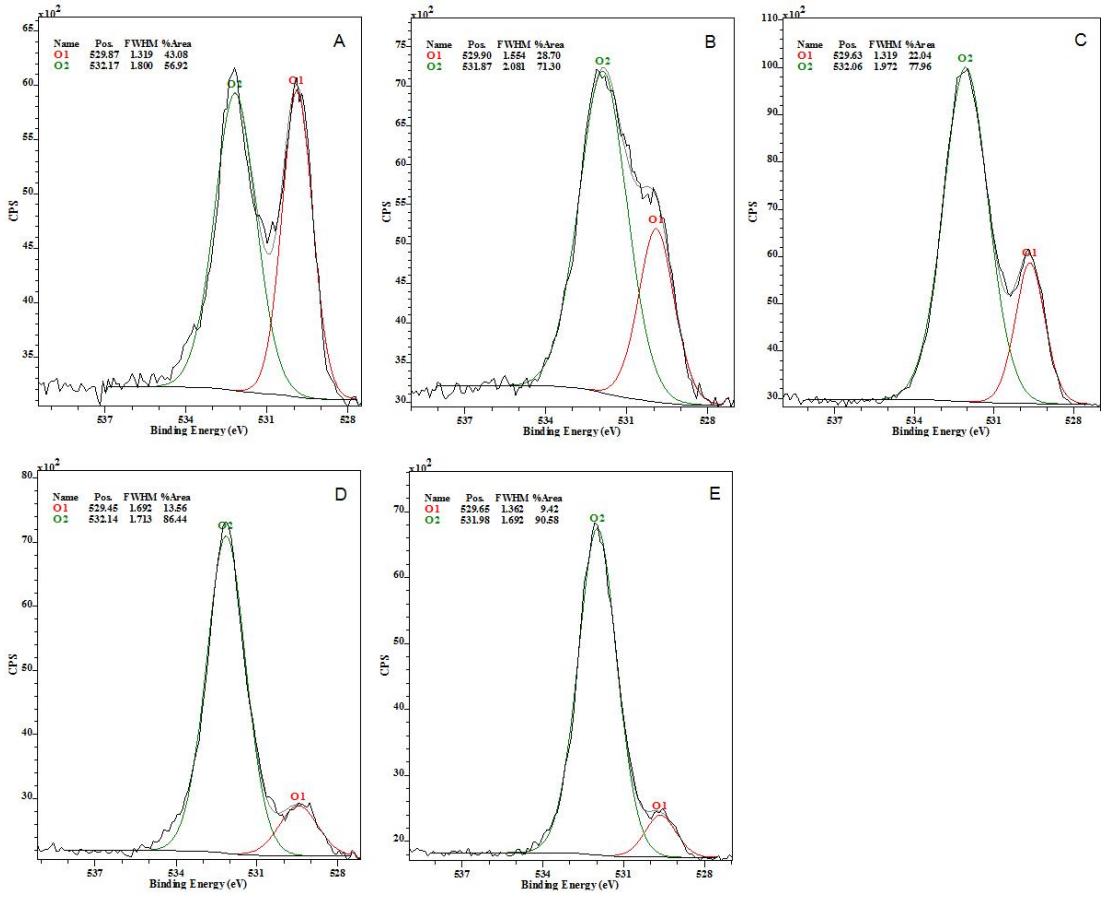

Figure 5.4: $O1s$ core level spectra of TiN reference sample (A) and $TiN(cem)20-120$ (B-E)

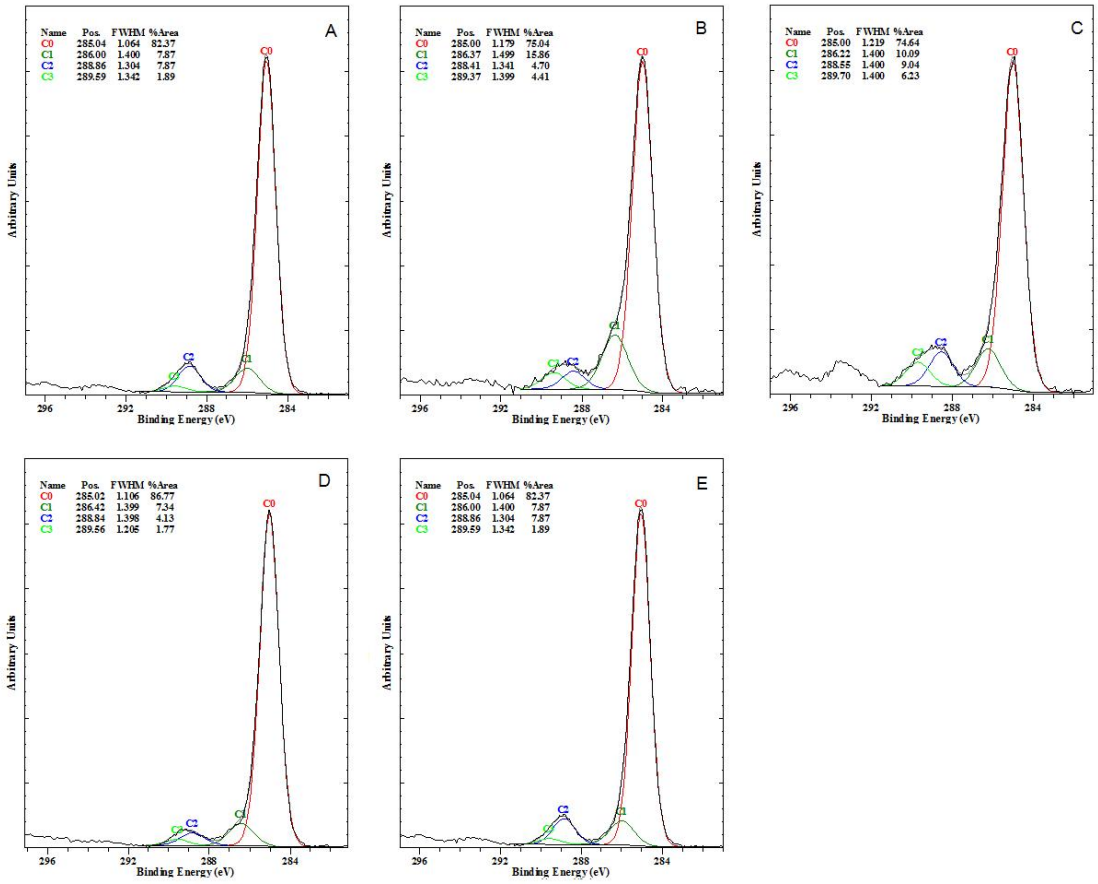

Figure 5.5: $C1s$ core level spectra of TiN reference sample (A) and $TiN(cem)20-120$ (B-E)

Finally, the core level $C1s$ spectra present all similar trends. A particular feature is observed in sample TiN(CEM)60, which consists in a more remarked component at the highest binding energy. This must be correlated with a total C content well below the values for the remaining surfaces and could be linked to a dominant presence of sulfated over carbonated components nucleated on the surface.

5.3.3 SEM observations

Analysing posible reflections for smaller angles, two new peaks where found at 9.090 and 18.065 in the XRD patterns, corresponding to the planes (100) and (110) of

ettringite in samples cured at 60°C, as shown in Figure 5.1 (b). That indicates the presence of ettringite on the TiN coating, the same peaks appear in CEM(TiN)60 sample analysed in previous chapter (Figure 4.3). SEM observations on TiN(cem)60 sample confirmed this fact, as can be seen in Figure 5.6 (a) and (b), where very thin ettringite crystals are arranged on the TiN film. The formation of this primary ettringite looking-like needles on the TiN surface might lead to significant strength improvement of the final solidified material. In this sense, assuming that all the tricalcium aluminate has already reacted to form primary ettringite, it is likely that the formation of secondary ettringite decreases,which reduces the risk of failure.

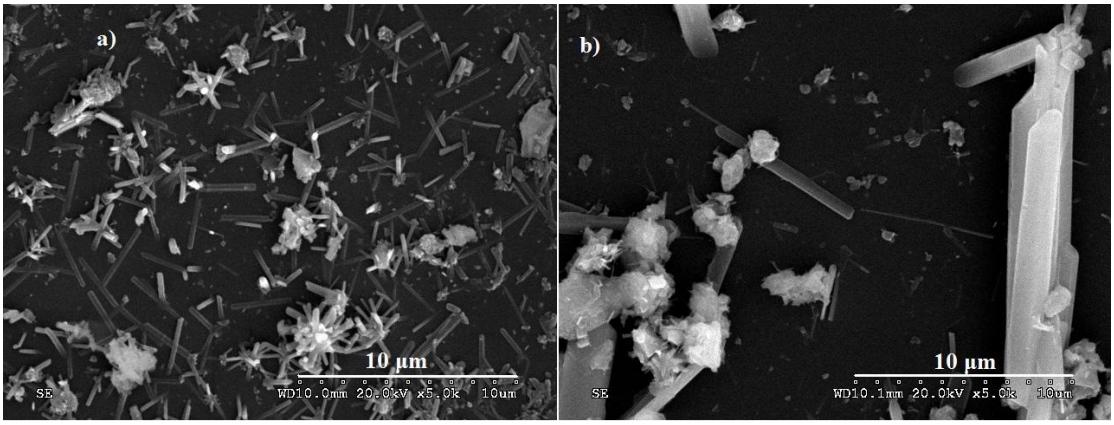

Figure 5.6: (a) and (b) SEM micrograph of TiN(cem)60 sample, showing thin ettrigite crystals on the film

5.3.4 TiN-cement interface microstructure

HRTEM images were obtained from the SiO_2/TiN and SiO_2/TiN/cement interfaces. Figure 5.7(a) shows the interface between the underlying SiO_2 and the TiN coating, with a smooth transition of about 2 nm thickness. Several crystalline structures with different orientations (resolved in 2D or 1D) corresponding to the TiN columnar growth can be clearly identified. The polycrystalline structure is confirmed by the Fourier transformed of the area corresponding to TiN (see inset pattern in Figure 5.7

(a), which shows a multi-domain diffraction pattern of relatively intense dots. Figure 5.7 (b) presents the HRTEM image of the interface SiO_2/TiN/Cement resulting after curing. The image confirms that amorphization does not take place in the TiN surface with respect to the original columnar structures.

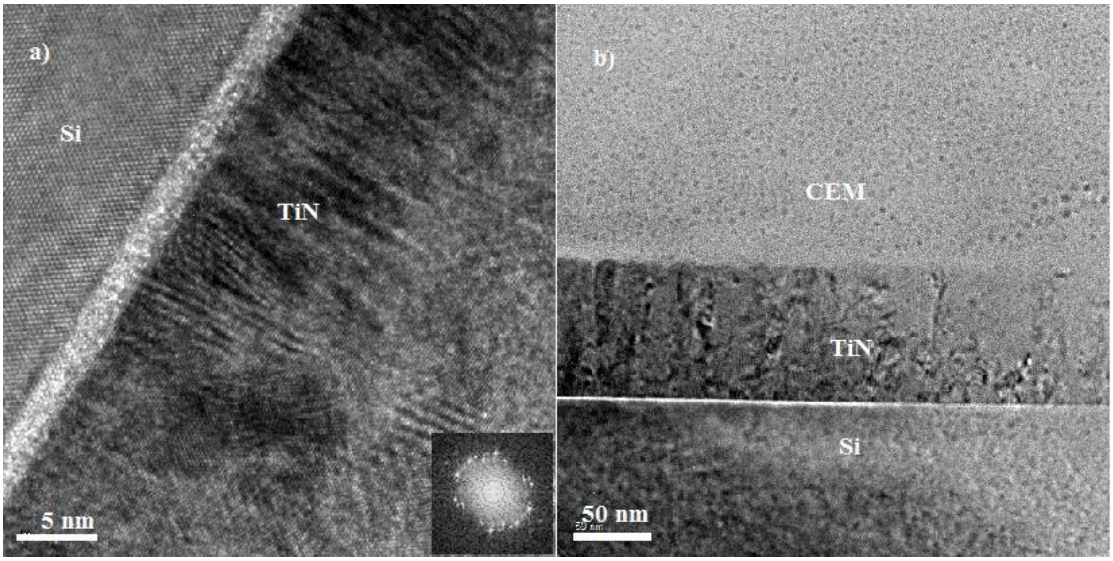

Figure 5.7: HRTEM micrograph of cross sections of TiN(cem)60 sample, featuring (a) a columnar structure of nanosized TiN crystals with preferential growth direction perpendicular to the Si/TiN interface, with inset corresponding to the Fourier transformed from the TiN area. (b) Si/TiN/cement interface displaying crystalline areas within the amorphous matrix

The presence of crystalline areas can be spotted in the cement side, uniformly distributed along with a greatly amorphous structure. To deepen our understanding of the crystalline presence in the cement side, further HRTEM images were taken of the TiN(cem)60 sample, as shown in Figure 5.8. Several nanoparticles with particle sizes varying between 4 and 5 *nm*, are present in the TiN/cement interface. The particles are crystalline and have twin boundaries. Interplanar distances of 2.1 Å were estimated from the FFT of Figure 5.8 (a). The crystallites do not correspond to any of the previous phases described in the XRD diagrams of TiN(CEM) or CEM(TiN) samples. According with the *collodial model* proposed by [Richardson 2008] and discussed in Section 2.1.4.1, a structure comprising highly concentrated "colloidal" CŰSŰH nanoparticles

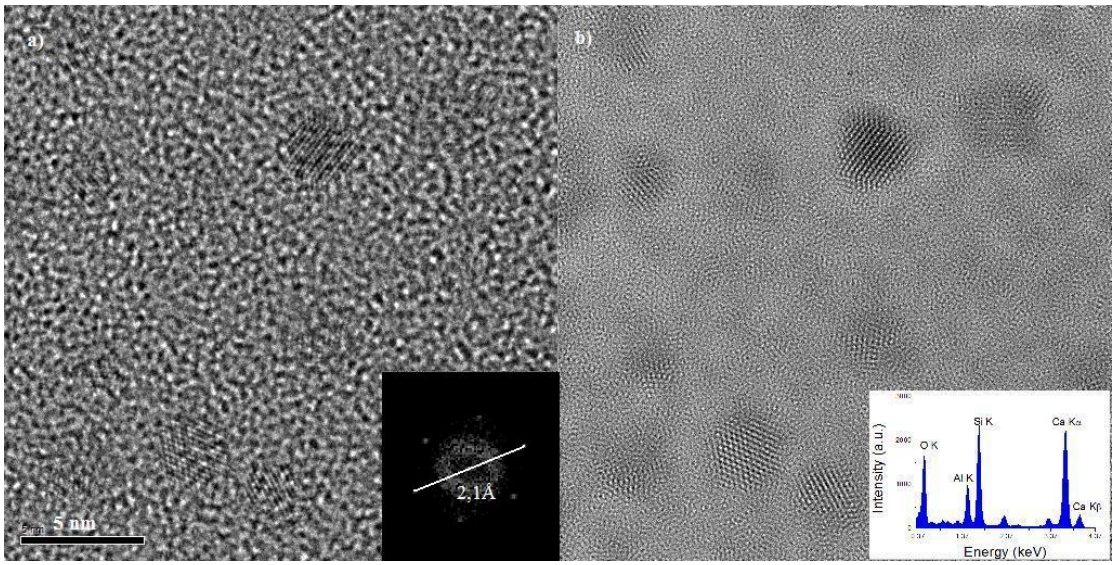

Figure 5.8: HRTEM micrograph of sample TiN(cem)60 at cross-section, showing crystalline clusters of C-S-H along with amorphous C-S-H on the TiN surface. FFT transformed is shown inset. (b) Processed image of (a), highlighting the clusters of a crystalline phase of C-S-H. EDX spectrum inset

dispersed in an amorphous matrix is identified in the TiN/Cement interface analysed hereby. Richardson's model predicts that C-S-H particles have characteristic sizes between 312 nm. From the filtered image 5.8 (b), the identified nanoparticles display a diameter in the range of $\approx 4-5$ nm. It can be considered that the results presented in this work are compatible with Richardson's collodial model for C-S-H nanostructure, and therefore the nanoparticles detected at the interface between TiN and cement paste might correspond to a crystalline phase of C-S-H.

To provide arguments based on the composition of this phase, a EDX spectrum from the selected area is shown in the inset of Figure 5.8 (b). It illustrates that the phase is rich in Ca and Al (Si may also proceed from the substrate) so that the origin may be an ettringite domain having suffered a phase transformation due to the sample preparation. In particular, ion beam milling is prone to inducing the loss of constitutional water in hydrated ceramics.

5.3.5 Potentiodynamic polarization scan

Figure 5.9 shows anodic and cathodic polarization curves for TiN(cem) samples and the reference sample. These polarization curves were determined by the potentiodynamic method as described in Section 5.2.3. Both the anodic and cathodic branches of the polarization curve display Tafel behavior, and the Tafel slopes can be extrapolated to determine the values of E_{corr} and i_{corr}, as listed in Table 5.3.

	Tafel extrapolation				
Sample ID	$E_{corr}mV$	$i_{corr}nA/cm^2$	b_amV	b_cmV	$R_p\Omega \cdot cm^2$
TiN	-284.556	344.691	310.6	437.2	0.229
TiN(cem)20	-494.787	3.252	221.1	165.6	12.642
TiN(cem)60	-492.251	14.358	47.1	40.0	0.654
TiN(cem)90	-496.221	13.942	60.5	52.0	0.871
TiN(cem)120	-519.310	21.965	92.1	73.2	0.806

Table 5.3: Corrosion values, calculated by extrapolation of Tafel slopes, for reference sample and TiN(cement) specimens

Excellent corrosion behaviour has been observed in all the samples, as the corrosion current is only in the range of nA/cm^2, which is in agreement with previous work on magnetron sputtered TiN thin films [Martin-Palma 2003]. All the interface TiN/cement samples feature higher corrosion resistance than TiN bare film. From Table 5.3, the values of E_{corr} in samples TiN(cem) deviate considerably from that of TiN reference sample. It is known that the corrosion at $Ecorr$ for TiN thin films is mostly due to the existence of pinholes in the film as a consequence of its columnar structure of nanosized TiN crystals, as shown in Figure 5.7 (a). These defects are the only paths which the corrosion agent transferred to the substrate can take, therefore they become the main factor that decides the corrosion resistance of the coating. The behaviour of the electrochemical reactions is neccesarily different when there is cement paste on the surface of the TiN film. In addition, for the reference sample the cathodic reaction of hydrogen evolution occurs on the surface of TiN film. For the samples that had been in contact with cement paste, the cathodic reaction, also assumed to be hydrogen evolution, occurs, possibly, on the surface of cement hydration products.

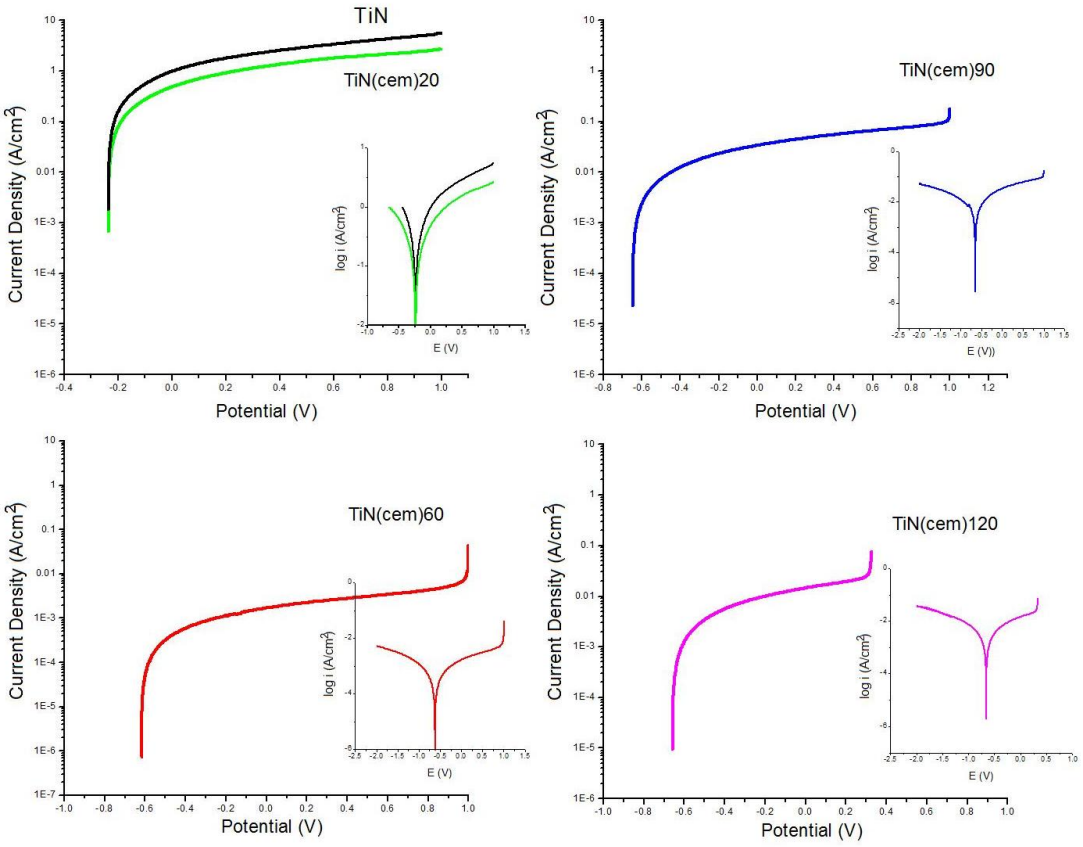

Figure 5.9: Potentiodynamic polarization curves measured for TiN(cem) samples and reference sample

Since E_{corr} is a thermodynamic property, the values of E_{corr} in the samples that were thermally treated were expected to be far away from that of the TiN reference specimen, as is seen in Table 5.3. The density current is also remarkably different for those samples that have undergone thermal treatment. In order to better assess these diferences, the polarization resistance was calculated by using the Stern-Geary equation (3.13), and listed in Table 5.3. From these results, it follows that the corrosion resistance of TiN(cem)20 shows the highest value, coinciding with the fact that this sample presents the highest $Ca(OH)_2$ content, as discussed in section 4.3.3, therefore forming a more compact passive layer at the interface with TiN. In the same way, as sample TiN(cem)60 has less portlandite content than samples TiN(cem)90 and TiN(cem)120,

the polarization resistance is lower, due to the different composition and microstructure of the TiN/cem60 interface, which underwent thermal shock. The columnar structure of TiN thin films includes the existence of numerous inherent pinholes that are detrimental for the purpose of a corrosion protection film. When cement hydration products are developed within this structure, the C-S-H gel is likely to grow in the pinholes of the TiN, provinding a denser structure for better corrosion resistance. In addition, the presence of $Ca(OH)_2$ at the interface forms the desirable passive layer which protects the TiN film against chloride penetration.

5.4 Conclusions

The interface between TiN thin film and cement paste has been reported for the first time. The following remarks can be concluded regarding the TiN side:

- The hydration of cement paste on the surface of TiN thin films does not affect the microstructure and crystalline nature of TiN, as seen in XRD patterns. Only light lattice parameters distorsions can be found in the crystal arragement as a consequence of the different thermal expansion coefficient between cement and TiN.

- Quantitative analyses by XPS along with XRD diffractograms prove evidence of a nucleation of Ca compounds in the TiN/cement interface cured at 60°C. At higher temperatures, the preferential nucleation of Ca turns into the form of calcite. Thermal shocking in the interface cured at 60°C is revealed by the presence of gypsum and sulfur in the XRD and XPS results, respectively.

- HRTEM observations of the TiN thin film confirm columnar structure of nano-sized TiN crystals with preferential growth direction perpendicular to the Si/TiN interface, which is characteristic of magnetron-sputtered TiN thin films. The presence of cement hydration products on the film does not modify this structure.

- Crystalline clusters of C-S-H are found at the interface between TiN/cement, inserted in the greatly amorphous struture of the cement side. Further HRTEM studies on this interface revealed extremely small nanoparticles with particle sizes varying between 3 and 4 *nm*. Interplanar distances of 2.1 Å are identified from the FFT, which might correspond to a crystalline phase of C-S-H. The crystallites do not correspond to any of the previous phases described in the XRD diagrams of TiN(CEM) or CEM(TiN) samples. EDX spectrum from the selected area illustrated that the phase is rich in Si, Ca and Al, which gives some soundness to our hypothesis.

- The potentiodynamic polarization results show that both TiN and the set of TiN(cem) treated under several temperatures, have a high corrosion resistance in chrolide environment. However, the corrosion resistance for sample that underwent thermal shock is slightly lower due to the different microstructure that this specimen developed.Nevertheless, all the interface TiN/cement samples feature higher corrosion resistance than TiN bare film. Hydrating cement paste on the surface of TiN thin film has a possitive effect on the corrosion behaviour of the film, as the hydration products obstruct the corrosion process on the interface between the film and the cement paste.

CHAPTER 6

Addition of Titania Nanoparticles in the Cement Matrix

This chapter presents an investigation on the effects of different additions of TiO_2 nanoparticles on the amorphous C-S-H gel nanostructure. TiO_2 nanoparticles prepared by the sol-gel technique were blended with fresh cement paste in a simple preparation method, in order to enhance its photocatalytic performance. The photocatalytic activity of the TiO_2/cement system was evaluated from the degradation of Methylene Blue (MB) under UV irradiation. The photoreaction was followed by monitoring the absorbance of MB, at a given wavelength, in the presence of TiO_2-doped hardened cement paste, under UV irradiation. For this purpose, a tailor-made photometry system was used. The modification of cement paste nanostructure was analysed by XRD, TGA/TDG and SEM. The results show that TiO_2 nanoparticles embedded in the cement matrix not only provided the system with photocatalytic properties, but also promotes the formation of C-S-H, which may provide improved mechanical performance to the cementitious material.

6.1 Introduction

Nanoscale modification techniques are one of the main specific domains of research in order to enhance the performance of cementitious construction materials. Recent studies in cement systems have focused on providing the cementitious materials

with photocatalytic functionality in order to reduce the levels of urban pollution. As introduced in Section 2.4.1.1, TiO_2 heterogeneous photocatalysis follows the mechanism described in the aforementioned section and subscribed here in more detail:

1. Absorption of photons ($h\nu \geq E_G = 3.2\ eV$) by titania

$$(TiO_2) + h\nu \rightarrow e^-_{CB} + h^+_{VB} \tag{6.1}$$

2. Oxygen ionosorption (first step of oxygen reduction; oxygen's oxidation state goes from 0 to $-1/2$)

$$(O_2)_{ADS} + e^-_{CB} \rightarrow O^-_2 \tag{6.2}$$

3. Neutralization of OH^- groups by photoholes which produces OH° radicals

$$(H_2O \Leftrightarrow H^+OH^-)_{ADS} + h^+_{VB} \rightarrow H^+ + OH^\circ \tag{6.3}$$

4. Neutralization of $O^{\circ-}_2$ by protons

$$O^{\circ-}_2 + H^+ \rightarrow HO^\circ_2 \tag{6.4}$$

5. Transient hydrogen peroxide formation and dismutation of oxygen

$$2HO^\circ_2 \rightarrow H_2O_2 + O_2 \tag{6.5}$$

6. Decomposition of H_2O_2 and second reduction of oxygen

$$H_2O_2 + e^- \rightarrow OH^\circ + OH^- \tag{6.6}$$

7. Oxidation of the organic reactant R via successive attacks by OH° radicals

$$R + OH^{\circ} \rightarrow R^{'} + H_2O \tag{6.7}$$

8. Direct oxidation by reaction with holes

$$R + h^{+} \rightarrow R^{+\circ} + degradation\ products \tag{6.8}$$

A quite-exhaustive list of various families of organic pollutants which can be treated by TiO_2 photocatalysis has been given in [Blake 1997]. In most cases, the degradation is conducted by dissolved compounds in water with UV-illuminated titania. Concerning the development of environmental-friendly construction materials, one of the most investigated and currently used additives, which ultimately produces such desired results, is nanostructured TiO_2 dispersed in the cementitious matrix [Nazari 2010], [Agrios 2005] and [Maury Ramirez 2010]. However, only a limited number of commercial composites based on such substance currently exist in the market, owing to the fact that there is still a lack of research on the effects of TiO_2 additives on the microstructure of the cementitious matrix.

The present chapter has two aims: to set forth a suitable addition of TiO_2 nanoparticles to be added to the cement matrix in order to provide an optimal photocatalytic activity, and to analyse the influence of embedded TiO_2 nanoparticles on C-S-H nanostructure. The experimental results are presented in a way that will stress the close relationship between the objectives.

6.2 Materials and Methods

6.2.1 Specimen preparation

Cement paste was prepared in Section 3.2.1. The TiO_2 nanoparticles were lab-prepared by the sol-gel technique according to the procedure described in 3.1.1.2. The selected concentration of TiO_2 sol-gel nanoparticles was added to the mixing water for preparing the cement paste. The specimens were left to cure during seven and 28 days. After the curing time, the specimen was inserted in 100 mL aqueous solution of Methylene blue previously prepared, as described in section 3.5.1. The suspension was allowed to settle in the dark for 30 min to obtain adsorption-desorption equilibrium, eliminating any error caused by initial adsorption. The suspension was then placed in an outer-irradiation-type reactor.

Sample ID	H_2O/CEM ratio %	Cement paste wt (gr)	TiO_2 loaded wt(gr)%	TiO_2:CEM ratio (in mass)
CONTROL	0.5	1.5	0	–
TiO2/CEM 1:10000	0.5	1.5	0.00015	1:10000
TiO2/CEM 1:1000	0.5	1.5	0.0015	1:1000
TiO2/CEM 1:100	0.5	1.5	0.015	1:100
TiO2/CEM 1:10	0.5	1.5	0.15	1:10

Table 6.1: Experimental conditions for TiO2/CEM samples prepared.

Five series of samples were prepared. The first series (CONTROL) consisted of cement paste prepared with de-ionised water, employing a water-cement ratio (w/c)=0.5, and stored at 20 °C in air, with no TiO_2 addition. The second to fifth series corresponded to cement paste prepared with de-ionised water (w/c=0.5) mixed with sol-gel synthesized TiO_2 nanoparticles. Four different TiO_2/cement paste content ratios were used for each series, labelled TiO_2/CEM (1:10), (1:100), (1:1000) and (1:10000) according with their TiO_2/cement weigth ratio. The conditions for TiO_2 loading are summarized in Table 6.1, together with the sample code.

All samples were 1 $cm \times 1\ cm \times 0.3\ cm$ in size and were cured at 20 °C in air.

The morphology of the samples was analysed by SEM microscopy at two different hydration times: 7 and 28 days. After the curing time, the specimens were inserted in 3 *cm* diameter quartz cuvettes filled with an aqueous solution of Methylene blue previously prepared with de-ionised water with an initial concentration of 18×10^{-6} *M*.

6.2.2 Characterization methods

Crystalline phases in the samples were identified by the diffratometrer X'Pert PRO of Panalytical, with $\theta/2\theta$ geometry, primary $K_{\alpha 1}$, and ultra-fast detector X'Celerator multichannel, under $\Theta/2\Theta$ configuration with 0.02 °scan step and 6 *s* integration time. The phase identification was first obtained by using the Match! Software version 1.10 together with the JCPDS database.

The degree of hydration and the C-S-H content were estimated by using TGA experiments conducted using TA Instruments, Q500 and Q100. Prior to testing, a specimen was immersed in isopropyl alcohol for 1 day to stop hydration at a desired hydration period and it was then dried to air for 1 day to remove the isopropyl alcohol from the system. The temperature was ramped from room temperature to 900°C at 10°C/min with a 100 ml/min nitrogen gas flow. The analysis was conducted by the TA Instruments Universal Analysis V4.2E.

Scanning electron micrographs were acquired using a ZEISS EVO 50 SEM operating at 20 KeV accelerating voltage, and equipped with an energy dispersive X-ray spectrometer, X OXFORD Instruments, INCA Pentafet X3. Cement paste samples were Au/Pd sputter coated with a Emitech K550.

6.2.3 Photocatalysis experiments

The photocatalytic activity of the materials was investigated by studying the photodegradation of Methylene Blue (MB). MB was supplied by Sigma-Aldrich at 0.04% solution in water. The UV-irradiation was provided by a high pressure UV 22 125 *W*

mercury lamp (Optical Engineering) which emits radiation predominantly at 351 *nm*. A SpectraPro 150 spectrophotometer was used to measure the absorption spectra of the MB solution as a function of the 351 *nm* UV irradiation time. The absorbance analysis of the MB solutions was performed using a specially made system comprising a chopped tungsten lamp, a DSP Lock-In amplifier (7225 Signal recovery), a light Chopper Controller (Model 650) and an SPD-M10Avp photodiode detector to measure the transmitted light. This equipment and setup has been described in 3.5.1. Samples were irradiated with the UV lamp during the selected time, and then introduced in the spectrophotometer for measurement. The spectrophotometer is provided with a top optical window whose section area was ca. 11 cm^2, through which the suspension was further irradiated during the absorbance measurement. The visible absorption peaks of the analysed samples were also recorded in the $200 - 800$ *nm* range.

6.3 Results and Discussion

6.3.1 X-ray diffraction

The XRD diffractograms for the specimens after 7 days of hydration are shown in Figure 6.1. All samples present the most characteristic peaks of portlandite $Ca(OH)_2$ (012) (JCPDS 01-076-0571) and calcite $CaCO_3$ (JCPDS 04-012-8072), displaying a diffraction peak intensity distribution that appears slightly modified as a function of the TiO_2 concentration. The formation of calcite within the samples comes either from the CaO content of the anhydrous material or from the reaction between $Ca(OH)_2$ and atmospheric CO_2.

As a matter of interest, at 1:10 TiO_2/Cement weigth ratio, $Ca(OH)_2$ content is lower than in any other sample, whereas the intesity of the peak corresponding to a crystalline forms of C-S-H, according with [Mohan 1981], is highest in this sample. In addition, it can be observed in this sample less intensity in the calcite peaks. As

reported by [Taylor 1997], C-S-H reacts with CO_2 with formation of $CaCO_3$, which might be especially important in laboratory studies when dealing with mixes of high surface to volume ratio. This consideration suggests that the high content of TiO_2 nanoparticles in the 1:10 samples hinders the reaction between C-S-H and CO_2, which therefore decreases the carbonation processes.

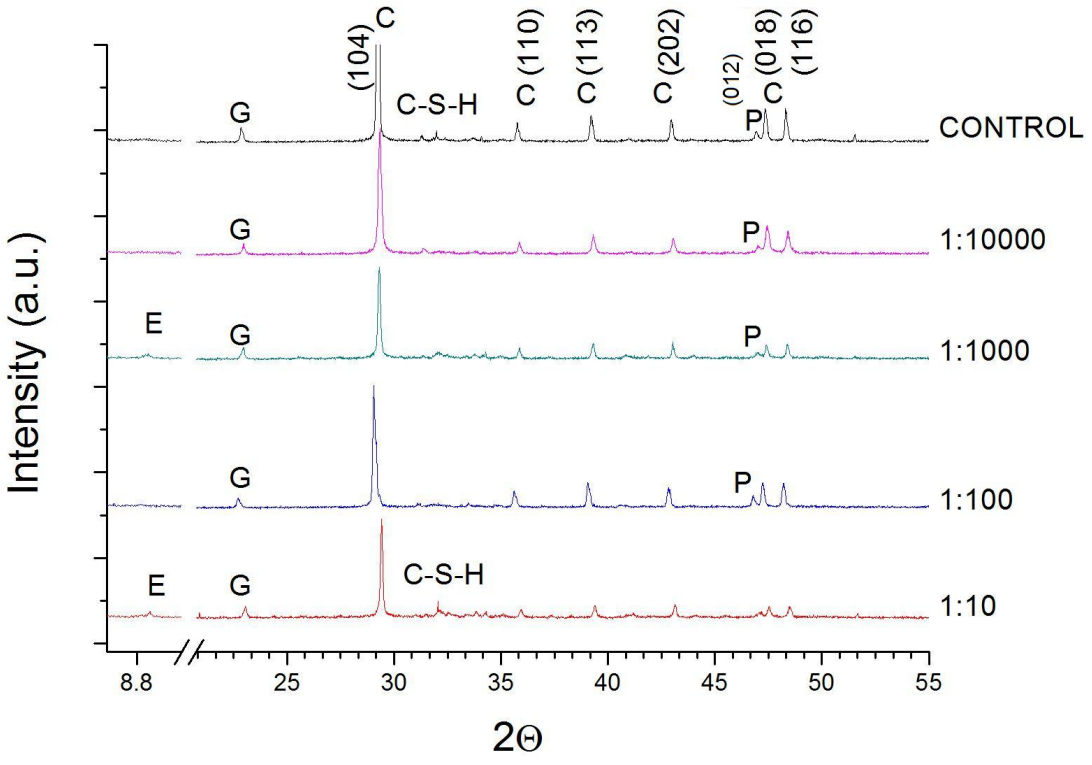

Figure 6.1: XRD diffractograms of the CONTROL and TiO_2/CEM samples hydrated at 20°C for 7 days. P: Portlandite, C: Calcite, E: Ettringite, G: Gypsum

The present of C-S-H in 1:10 samples - higher than in the CONTROL sample - suggests that high addition of TiO_2 promote the formation of this hydration product and reduce the carbonatation process. Furthermore, the main XRD peak of portlandite - (001) which is usually found at 2Θ =18.1°- was not observed for any sample. This fact indicates that the carbonation of portlandite by atmospheric CO_2 was especially intense during the curing period. The absence of $Ca(OH)_2$ cannot be attribuited to the presence of TiO_2 in the sample, as the aforementioned peak does not appear in the CONTROL

sample either. Gypsum is found in all samples. Ettringite crystals - a minor hydration product commonly present in early stages of hydration - seem to be more well defined in samples 1:10 and 1:1000, although their peaks are still weak. Gypsum content is expected to decrease as hydration process progresses, indicating its gradual conversion into hydrations products, C-S-H and portlandite. No other significant differences can be observed between samples. No indication of TiO_2 nanocrystalline phases was found in the XRD patterns, possibly due to the small crystal size and the limited sensitivity of XRD system.

XRD results suggest that the mineralogical composition of hydrated phases in the cement paste has not been altered, nor its crystallographic properties have been significantly affected, by the addition of TiO_2 nanoparticles. This is an important conclusion, because it is an indication that the sol-gel sinthesized TiO_2 nanoparticles embedded in the cement matrix do not deprive the system from progressing normally in every hydration stage.

6.3.2 Thermal analysis

The thermogravimetric analysis are presented in Figure 6.2, TG (A) and DTA (B). As shown in the figure, the following peaks were identified for each sample: an endothermic peak at 100°C due to the decomposition of ettringite and C-S-H, a quite intense peak of calcium hydroxide decomposition occurring at 410°C and a significant peak at 650°C, due to the CO_2 released during calcium carbonate decomposition. The respective weight losses can be obtained from the corresponding TG curves, which in turn allow the quantification of the respective phases. The thermogravimetric analysis of the TiO_2/Cement samples show no significant differences from the curve obtained for the CONTROL sample. Therefore,it can be concluded that the presence of TiO_2 nanoparticles embedded in cement paste, at the studied concentrations, have no influence on the characteristic temperatures of the thermal degradation of cement hydrated phases.

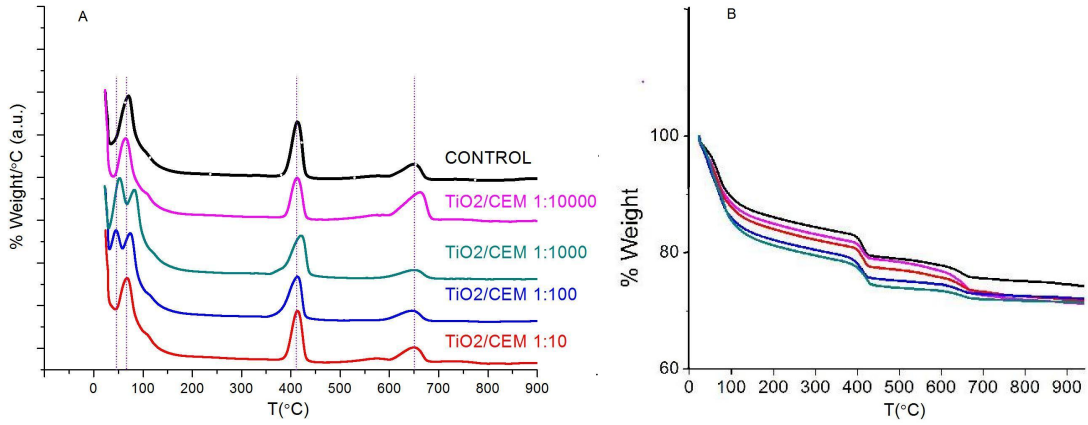

Figure 6.2: Thermogravimetric analysis (TG (A) and DTA (B)) of the CONTROL specimen (initial cement paste) and the TiO_2-doped specimens at various concentrations

Further analysis of the TG/TGA curves allows the determination of C-S-H content and degree of hydration of the samples, as described in Section 4.3.3. The DTA or DTG peaks corresponding to C-S-H gel and ettringite dehydration, usually occur in the temperature range of $100 - 135°C$. As explained in Section 4.3.3, there are also dehydration reactions of other minor hydrated compounds, which result in continuously decreasing TG curves of the hydrated pastes, mainly up to $400 - 450°C$. Therefore, the total TG weight loss from ambient temperature to 400° and the subsequent calcium hydroxide decomposition weight loss (which ends by $500°C$) were used to evaluate the degree of hydration of the paste. As recommended by Taylor [Taylor 1997], for a better evaluation of the hydration process, all the estimated contents and the water released from other hydrates were calculated with reference to the final ignited mass of the pastes at $1000°C$.

Figure 6.3 (A) depicts the calculated degree of hydration values for each specimen. It is observed that the degree of hydration progressively decreases as the concentration of titania nanoparticles in the cement paste increases, until reaching the highest concentration at 1 part of titania : 10 parts of cement, where the degree of hydration sharply increases, reaching even a larger value than that corresponding to the CONTROL sample, with no TiO_2 addition. This fact suggests that there was a significant

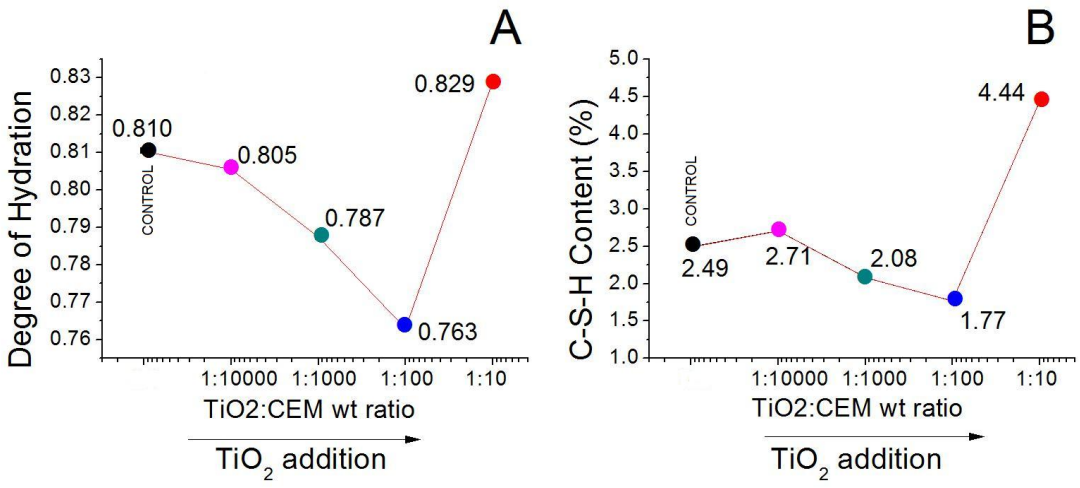

Figure 6.3: Degree of hydration (A) and C-S-H content (B) of the CONTROL specimen (initial cement paste) and the TiO_2 doped specimens at various concentrations. Colour key: red 1:10, blue 1:100, cyan 1:1000, magenta 1:10000, black CONTROL.

effect of the dosage of TiO_2nanoparticles on the degree of hydration. Specifically, relative to the CONTROL sample, at the TiO_2 addition 1:10000, 1:1000 and 1:100 a gradual decrease in the degree of hydration is observed (by -0.6%, -2.8% and -5.8% TiO_2). In contrast, the highest doping of titania nanoparticles in the cement paste, 1:10, resulted in a significant increase in the degree of hydration, by +2.3%. These findings suggest that loadings of TiO_2 nanoparticles has an effect on the hydration process of cement, being only high dosage those that promote the formation of hydration products by consumption of water within the cement paste microstructure. This can be explained by considering the state of water in the hydrating cement paste, as discussed in Section 2.1.2. The porosity of the cement with a high doping level of TiO_2 nanoparticles has to be necessarily lower than those cements with lower TiO_2 additions. In the 1:10 samples, the displacement of capillary water from the micropores now occupied by titania nanoparticles, induces the formation of hydration products that gradually fill up the interspace. Whereas if less titania is added, filling only part of the pore structure, less water is displaced to come into contact with the anhydrous reactants in the cement paste.

Figure 6.3 (B) displays the C-S-H content calculated from the weight loss occurring in the temperature range 100°C-300°C, at which gel C-S-H loses its bound water and descomposes completely[Khoury 1992]. The evolution of the content of C-S-H estimated for each sample, displays similar behaviour than the previously analysed degree of hydration versus TiO_2 doping level. It is observed that the cement paste with the highest TiO_2 doping level contains a substantially higher C-S-H content, by 78%, which suggests an induced formation of this hydration product by the presence of a high doping of TiO_2 nanoparticles in the cement paste. These results are in agreement with reported work on effects of dispersed TiO_2 in cementitious matrix [Nazari 2011]. The present study confirms that TiO_2 nanoparticles, in a high enough concentration, accelerate the formation of cement hydrates: the content of C-S-H in TiO_2/CEM 1:10 sample is significantly higher than that in the CONTROL specimen, as well as the degree of hydration of the corresponding sample.These results match with the analysis of the XRD patterns.

6.3.3 SEM characterization

To obtain detailed information about the morphology of the TiO_2/Cement system, SEM images were taken after 7 and 28 days of hydration for each specimen. Significant contents of microspherulites were detected in all cement pastes doped with titania nanoparticles, as those shown in Figure 6.4 right, not found in the CONTROL sample (left). The EDX technique was used in selected areas, in order to identify the elementary content of the microstructures, as are shown in Table 6.2.

According with [Richardson 2008], a distinction between high density inner product and low density outer product can be stablished. The outer product shows a morphology either fibrillar or foil like, whereas the inner product forms a pack and flocculates into what they term “globule flocs”. These proposed geometries are consistent with the observations of this work. The *spherulitic* morphology found in TiO_2-doped samples, appears to be consisting of bundles of inner C-S-H gel diverging from a single

TiO_2 nucleus. Fibrillar outer C-S-H gel bridges the spheres, developing a network-like morphology. Although such spherulites were present in all TiO_2/CEM samples, C-S-H gel with a foil-like morphology was observed to prevail with decreasing TiO_2 concentration.

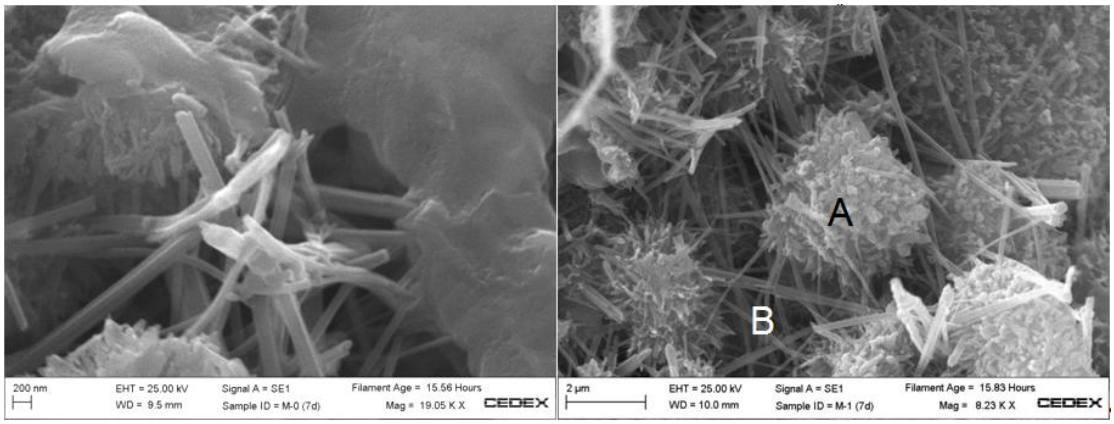

Figure 6.4: Left: Detail of SEM micrograph of the CONTROL sample after 7 days hydration time. Right: Detail of SEM micrograph of 7 days-old TiO_2/CEM 1:10 sample, showing shell microspheres of amorphous inner C-S-H gel formed around a TiO_2 nanoparticle. Fibrillar outer C-S-H bridges the spheres filling the inter-hydrates space

Region	Elementary analysis (% Weigth)	Main phase	Morphology
A	Al(1.85), Si(13.49), Ca(44.74) Ti(3.02), O(36.89)	TiO_2 + C-S-H	Inner Spherulite
B	Al(5.24), Si(8.35) Ca(51.63), O(34.78)	C-S-H	Outer Fibrillar

Table 6.2: EDX analysis of selected regions in SEM micrograph shown in Figure 6.4

Figure 6.5 shows SEM micrographs of the cement paste after loading TiO_2 nanoparticles under identical hydrothermal conditions, obtained after 7 days hydration time for different TiO_2 concentrations. At the lowest loading, 1:10000 TiO_2/CEM ratio, it can be seen in Figure 6.5 (A) that even though the amount of loaded titania was very small, the TiO_2 nanoparticles were covered with inner C-S-H gel. Most of the nanoparticles preferentially clustered at the entrance of the micropores, which may reasonably

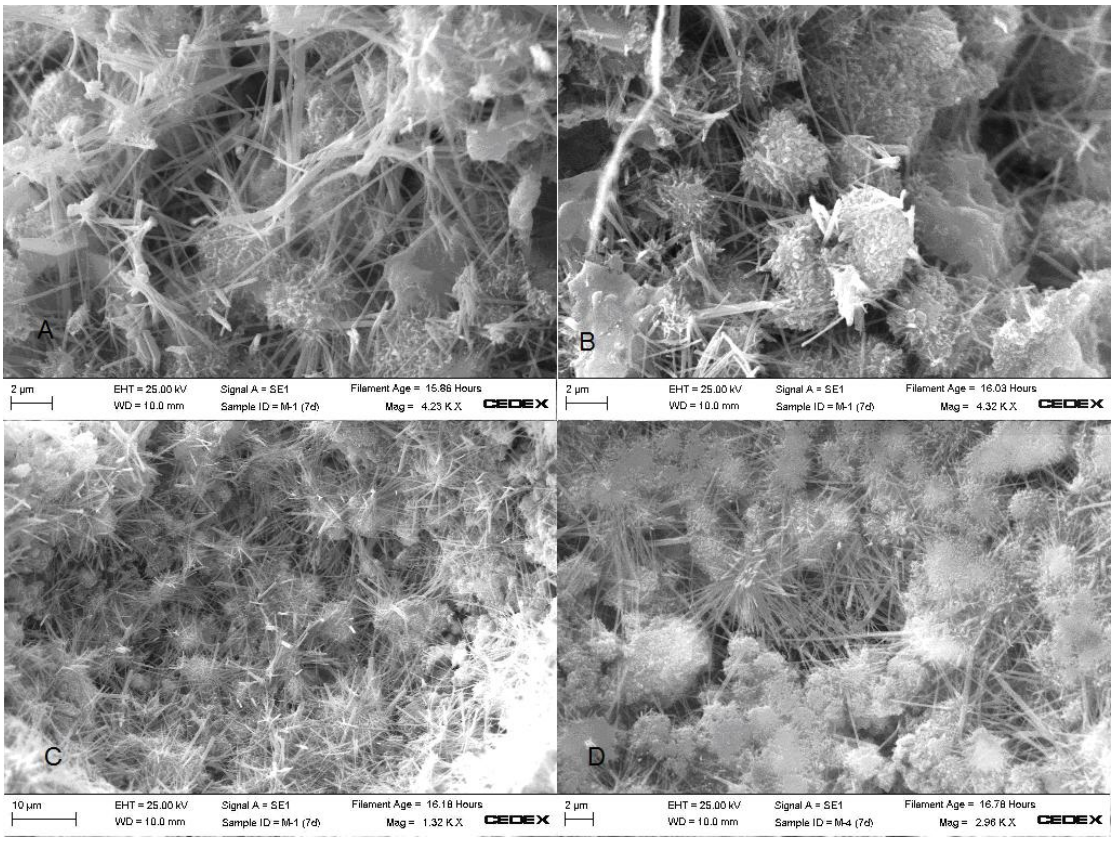

Figure 6.5: SEM micrographs of the cement paste after loading TiO_2 nanoparticles under identical hydrothermal conditions after 7 days hydration time. (A) sample TiO2/CEM 1:10000, (B) sample TiO2/CEM 1:1000, (C) sample TiO2/CEM 1:100, (D) sample TiO2/CEM 1:100.

increase the overall density and promote the formation of C-S-H inside these micropores. Increasing TiO_2 loading seems to extend the coverage of the micropores within the cement paste structure by titania nanoparticles surrounded by C-S-H gel (Figure 6.5. (B), (C) and (D)). No spherulitic structures were found in CONTROL sample (not shown).

The observation of preferential deposition of titania nanoparticles at the entrance of micropores is consistent with a certain decrease in the degree of hydration until the highest loading process (Figure 4.6 (B)), in agreement with the results obtained for the degree of hydration calculated by TGA analyses. According to the C-S-H content estimated in Section 4.6, TiO_2 nanoparticles addition at 1:10 TiO_2:cement paste con-

centration ratio, promotes a rather high C-S-H formation, which is confirmed by the SEM observations of such samples, Figure 6.5 (D), where each titania nanoparticle acts as a nucleation centre for inner C-S-H formation. As mentioned, fibrillar outer C-S-H gel bridging the nucleation sites and therefore developing a network-like morphology, can also be observed in the figure.

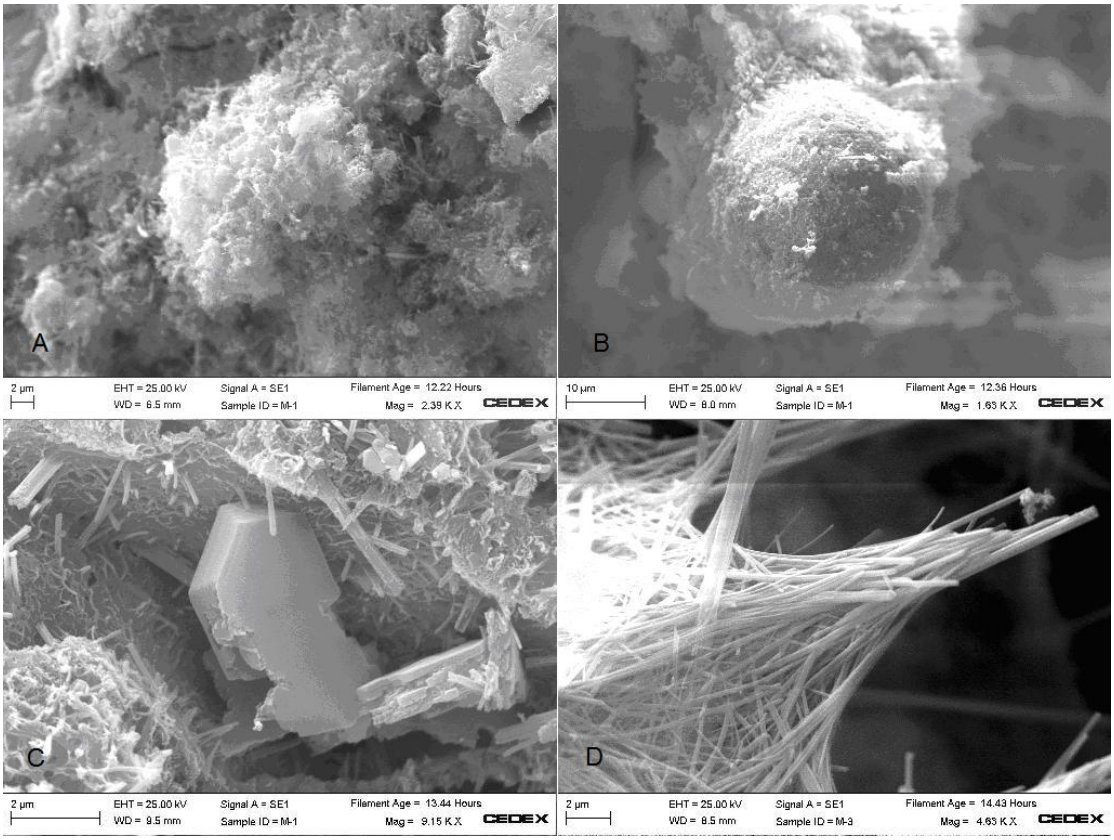

Figure 6.6: SEM micrographs of TiO2/CEM 1:10 sample after 28 days hydration time. (A) area of TiO_2 nanoparticles covered with inner C-S-H, (B) detail of a single TiO_2 nanoparticle in the cement paste structure, (C) a formation of portlandite crystal in the cement paste structure, (D) detail of fibrillar C-S-H bridging the nucleation centres.

Figure 6.6 shows SEM micrographs of the TiO2/CEM 1:10 samples obtained after 28 days hydration time. As titania nanoparticles have a relatively high specific surface area, close to 900 m^2/g, and due to their spherical shape, the physical surface which accommodates the C-S-H seems to be optimal for high C-S-H spherulite-like formation around each particle. Therefore, most of the titania nanospheres were covered

by C-S-H after 28 days of hydration, as shown in Figure 6.6 (A). A detail of one of those titania nanospheres is shown in Figure 6.6 (B), partially convered by C-S-H gel forming a spherulite. The relatively high degree of hydration of these samples was confirmed by the SEM observations of well-formed portlandite crystals and dense formations of fibrillar C-S-H (Figure 6.6 (C) and (D) respectively).

SEM characterization of 1:10 samples can conclude that the preferred location of TiO_2 nanoparticles is inside the micropores of the cement paste microestructure, providing the system with aditional nucleation sites for the formation of C-S-H gel which grows around each nanoparticle forming spherulites. The specific surface area of this morphologically homogeneous TiO_2/Cement system we understand is likely to enhance the photocatalytic activity, as reported in literature about the importance of surface microstructure on the photocatalytic activity of TiO_2 phases [Zhang 2008].

6.3.4 Photocatalytic activity

The absorption spectrum of methylene blue (MB) aqueous solution, measured from 400 to 1000 *nm*, is shown in Figure 6.7. At any wavelength in this range, it is possible to use the optical density or *absorbance* as a measure of methylene blue concentration, since the optical density increases linearly with concentration in accordance with Beer-Lambert's law:

$$A_\lambda = \varepsilon c l \tag{6.9}$$

where ε is the molar absorptivity of the absorber at a given wavelength, which indicates the ability of a molecule to absorb light at that wavelength. The number of molecules that interact with light depends on the pathlength l and the concentration of the molecules c. The absorbance can be determined by measuring the transmission of light through the solution, therefore

$$A_\lambda = -log\frac{I_0}{I} \tag{6.10}$$

where I_0 is the incident light and I is the transmitted light intensity. This mathematical transformation is used to make the relationship between concentration and absorbance linear

$$A_\lambda = -log\frac{I_0}{I} = \varepsilon cl \tag{6.11}$$

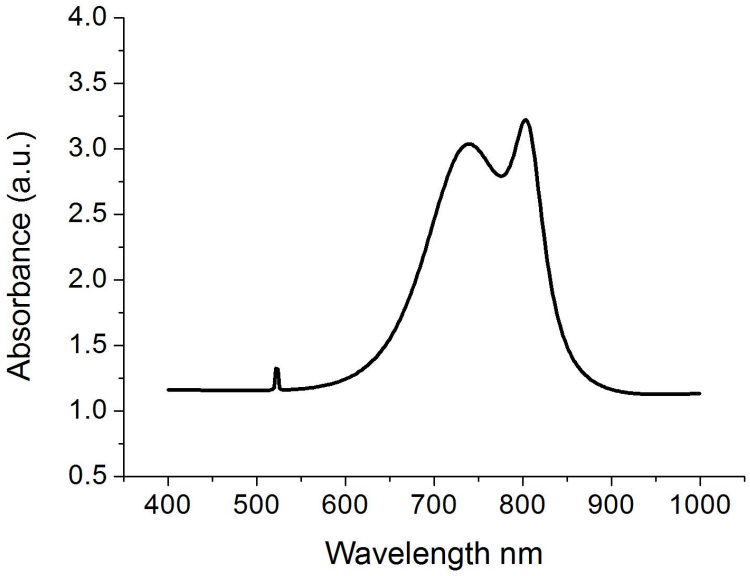

Figure 6.7: Absorption spectrum of MB aqueous solution

Absorbance ranges from 0 for perfectly transparent samples to infinity for perfectly opaque samples. The value of ε depends on the units of c. Typically, c is expressed in molarity ($moles \times liter^{-1}$), l is measured in cm, and therefore ε has units of absorbance ($cm^{-1} \times liters \times mole^{-1}$). Hence, absorbance is a direct measure of the MB concentration in MB aqueous solutions.

Absorbance was measured after UV irradiation intervals of 30 minutes. The photoactivity of each sample was continuously measured in the reactor for 100 seconds, to allow the suspension to settle. This procedure was repeated in order to obtain eleven absorbance versus time readings at successive time intervals for each sample. Table 6.3 sumarizes the results.

The kinetics of MB absorption at 665 nm wavelength, in the presence of ce-

ment paste modified with different TiO_2 dopings levels under UV irradiation, is represented in Figure 6.8. It can be seen that there is a clear concentration decrease for all TiO_2/Cement samples, indicating that some photoreactions were occurring within the TiO_2 doped cement, reactions that appear to be less significant in sample 1:10000, although it still shows certain photocatalytic activity revealed by a decrease of $\approx$ 30% in the MB concentration. Sample 1:10 shows the highest photocatalytic activity, whereas samples 1:100 and 1:1000 display similar MB concentration, with no remarkable differences.

The MB concentration for 1:10 samples decreases from 18 to 8.2 μM after 300 *min* UV irradiation time, exhibing a $\approx$ 52% degradation of MB concentration for 1:10 TiO_2/Cement doping level. As discussed in previous Section 6.3.3, high additions of sol-gel synthesized TiO_2 nanoparticles fill up the porous microstructure by the insertion of microspheres which results in a higher specific surface area. Moreover, high TiO_2 doping levels induce the formation of C-S-H seeding. Chemical shrinkage will then be replaced by TiO_2 nanoparticles and photoexcitation can readily occur.

From comparison of the results obtained for samples 1:10 and samples with lower concentrations of TiO_2, it may be suggested that the surface structure caused by high TiO_2 doping levels is a key factor promoting photoreactivity in TiO_2/cement. In the other hand, the fact that a more aqueous environment - as those in samples 1:10000 to 1:100 which exhibit low degree of hydration - promotes particle aggregation [Grela 1996], prompts that secondary TiO_2 particles of larger size are more likely to be formed when lower additions of titania are added to the cement paste, hence decreasing photocatalytic activity [Lin 2006].

The photocatalytic efficiency can be established by using the basic equation of decay

$$ln(c/c_0) = -Kt \tag{6.12}$$

where c_0 is the initial concentration of MB, c is the MB concentration at a given time t from which a decay constant K was calculated. This allows to estimate a *degrada-*

Sample code	UV Irradiation time (min)										
	0	30	60	90	120	150	180	210	240	270	300
CONTROL	1.755	1.753	1.751	1.750	1.749	1.742	1.738	1.734	1.734	1.733	1.731
TiO2/CEM 1:10000	1.752	1.643	1.500	1.456	1.401	1.364	1.307	1.266	1.166	1.156	1.133
TiO2/CEM 1:1000	1.754	1.687	1.346	1.133	1.098	1.073	1.088	1.070	1.062	1.018	0.994
TiO2/CEM 1:100	1.749	1.601	1.411	1.249	1.198	1.088	1.070	1.070	1.054	1.040	1.022
TiO2/CEM 1:10	1.750	1.568	1.189	0.931	0.924	0.910	0.902	0.868	0.850	0.822	0.802

Table 6.3: Absorbance of MB during the photodegradation progress.

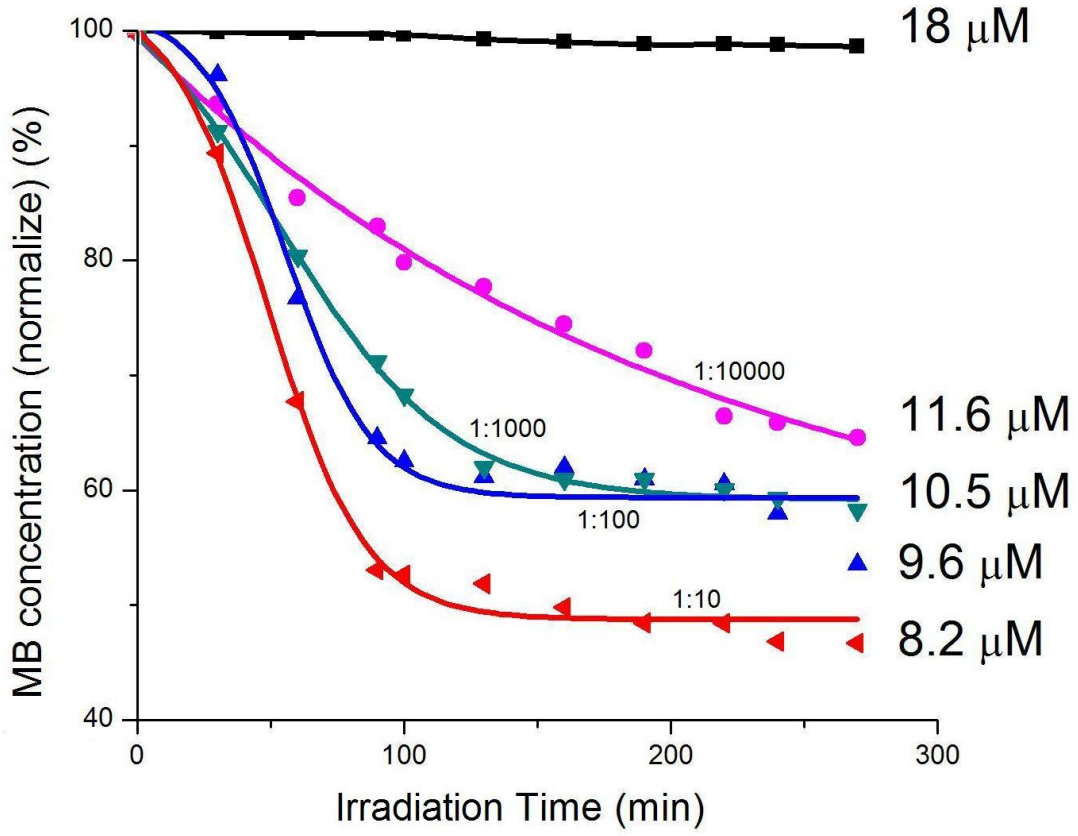

Figure 6.8: Evolution of MB concentration with time for different TiO_2 doping levels. Straight lines represent the exponential decay fitting for each set of values. CONTROL sample, with no TiO_2 addition, represented as black lines-spots.

tion rate calculated from fitting the kinetics of MB absorption to exponential decays, as shown in Figure 6.8. The values of the rate of degradation ($\mu Mmin-1$) were calculated from the kinetic data (Table 6.3) and plotted versus TiO_2 doping level, as shown in Figure 6.9. For the doping levels tested, it is observed that the degradation rate does not reach saturation for TiO_2 nanoparticles loading, suggesting that there are still MB molecules available for degradation if an increased number of TiO_2 nanoparticles was to be added above the highest concentration. Thus, in the work presented herein, the degradation rate of MB increases with amount of photocatalyst without reaching a specific limit.

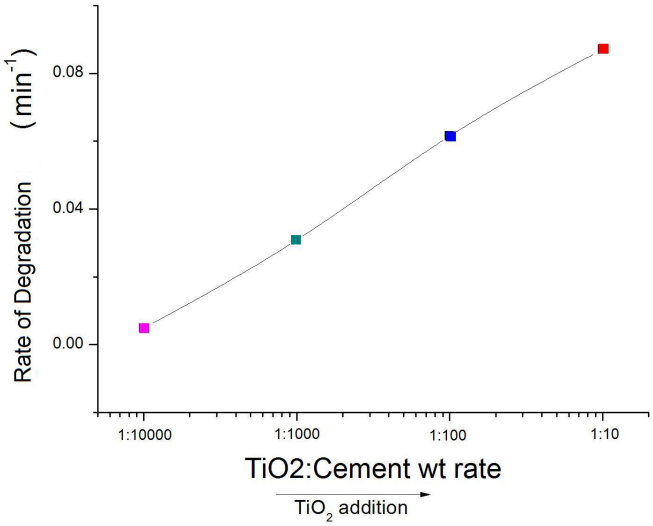

Figure 6.9: Speed of MB degradation versus TiO_2 doping level in TiO_2/Cement samples

In order to examine the controlling mechanism of photodegradation process, the experimental data were also analyzed using the pseudo-first and pseudo-second-order kinetic models, and kinetic constants were calculated in all samples. The pseudo-first-order kinetic model has been widely used to predict dye degradation kinetics. A linear form of pseudo-first-order model was described by Lagergren [Taty-Costodes 2003]:

$$log(q_e - q) = logq_e - (k_1/2.303)t \tag{6.13}$$

where q_e and q are the amounts of photodegraded MB by the TiO_2/Cement system at equilibrium and at time t, respectively (mg/g). and k_1 is the rate constant of first-order kinetics ($1/min$). The amount of photodegraded MB can be calculated from the experimental data by using the following relantionship:

$$q_e = (c_0 - c_e)/M \tag{6.14}$$

where c_0 and c_e are the initial and equilibrium concentrations (mg/L) of MB, respectively, and M is the mass of TiO_2 used.

In order to fit Equation (6.13) to the experimental data, the amount of photodegraded MB at equilibrium, q_e, must be known. In many cases q_e is unknown, degradation tends to become immeasurably slow and the amount of photodegraded dye is still significantly smaller than the equilibrium amount. For this reason, it is necessary to obtain the real equilibrium degradation by extrapolating the experimental data to $t = \infty$. Also, in many cases the first-order equation of Lagergren fits well only when photoreactions occur in liquid phase [Aksu 2003].

Pseudo-first-order		TiO_2:Cement wt ratio			
	0:1	1:10000	1:1000	1:100	1:10
k_1, min^{-1}	-	0.0036	0.0046	0.0043	0.0044
r_l^2	0.9485	0.9348	0.7421	0.8172	0.7073
Pseudo-second-order		TiO_2:Cement wt ratio			
	0:1	1:10000	1:1000	1:100	1:10
k_2, min^{-1}	-	0.00101	0.00140	0.00141	0.00169
$q_e(calculated)$, mg/g	-	63.897	56.915	54.975	45.413
$q_e(experimental)$, mg/g	-	28.733	36.462	47.275	55.713
r_2^2	0.99999	0.98977	0.99657	0.99082	0.99643

Table 6.4: Photodegradation kinetic parameters of MB on nanosized TiO_2 doped cement paste

The values of first-order rate constants and the correlation coefficient r_l^2 values obtained after the linear correlations, are given in Table 6.4. Although there is an initial increase in the k_1 from CONTROL sample to 1:10000 samples, only moderate increases

are observed as the TiO_2 doping level increases, displying even a lower equilibrium rate constant when the TiO_2/Cement weigth rate reaches 1:100 level. It was also observed that correlation coefficients were lower than the CONTROL sample for all doping levels. This shows no applicability of the pseudo-first-order model in predicting the kinetics of the methylene blue absorption in the TiO_2 doped cement paste.

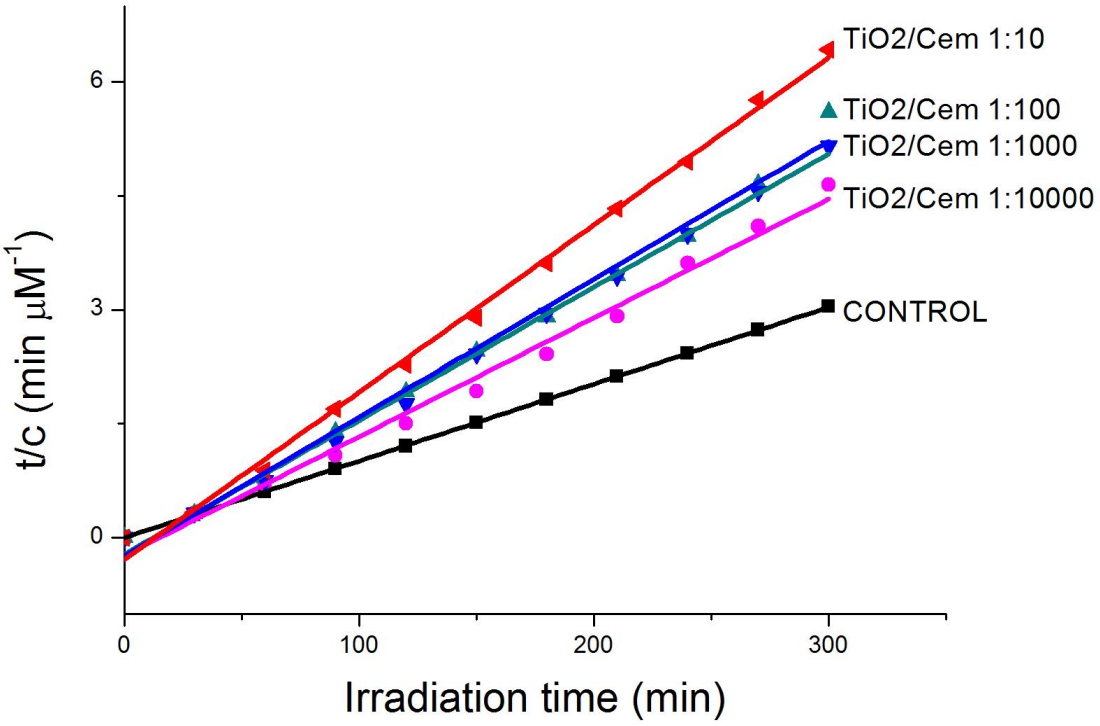

Figure 6.10: Pseudo-second-order kinetics approach for MB degradation in TiO_2/Cement system at different doping levels.

A pseudo-second-order model may also describe the kinetics of degradation. The pseudo second-order equation is based on the degradation capacity of the solid phase. This model predicts that intra-particle diffusion/transport process being the rate controlling step, which may involve valency forces through sharing or exchange of electrons between dye anions and photoreactants. The kinetic data were further analyzed using Ho's pseudo-second-order kinetics, represented by [Vadivelan 2005]

$$t/q = 1/(k_2 q_e^2) + (1/q_e)t \tag{6.15}$$

where k_2 is the rate constant of second-order ($1/min$).

If the second-order kinetic is applied, the plot of t/q against t should give a linear relationship, from which q_e and k_2 can be determined from the slope and intercept of the plot. The values were calculated from the kinetic data (Table 6.3. The fitted plots are given in Figure 6.10 and the calculated q_e, k_2, and the corresponding linear regression correlation coefficient values are summarized in Table 6.4.

The linear plots of t/q versus t show good agreement between experimental and calculated values. The smallest correlation coefficient in this case was 0.98977, which corresponds to 1:10000 TiO_2/Cement weigth ratio. The rest of the samples display correlation coefficients for the second-order kinetics model greater than 0.99, indicating the applicability of this kinetics equation and the second-order nature of the photodegradation process of methylene blue in the TiO_2/Cement system. This fact indicates that the rate controlling step is intraparticle diffusion, which is in fact the kinetic mechanism followed by the hydration of anhydrous particles in the cement paste at the hydration period under examination [Breugel 1991].

6.4 Conclusions

TiO_2 nanoparticles prepared by the sol-gel technique were inserted for first time in fresh cement paste with differing concentrations. The microestructure of the TiO_2/Cement system was studied. The photocatalytic activity of the so-formed system was analysed by means of the degradation of methylene blue aqueous solutions under UV irradiation. The following conclusions can be drawn from the results presented hereby:

- XRD diffractrometry shows that at 1:10 TiO_2/Cement weigth ratio, samples contain high amounts of C-S-H gel. The cabonation process due to atmospheric CO_2 is affected by the presence of high dosage of TiO_2 nanoparticles in the cement paste, as calcite peaks for such samples show lower intensity. Nevertheless,

the mineralogical composition of hydrated phases in the cement paste is not altered by the addition of titania nanoparticles in the cementitious material, nor their crystallographic properties are significantly affected by the addition of TiO_2 nanoparticles. This is an indication that the sol-gel sinthesized TiO_2 nanoparticles embedded in the cement matrix do not impede the system from progressing normally in every hydration stage.

- The thermogravimetric analysis of samples doped with titania nanoparticles show no significant differences from the curve obtained for the cement paste with no TiO_2 addition. This fact implies that the presence of TiO_2 nanoparticles embedded in cement paste has no influence on the characteristic temperatures of the thermal degradation of cement hydrated phases.

- Concerning the hydration rate of the TiO_2/Cement system, estimated by TGA analysis, there is clearly an effect of the dosage of TiO_2nanoparticles on the degree of hydration. Low loadings of titania produce a gradual decrease in the hydration degree, whereas high dosage result in a significant increase in the aforementioned hydration parameter, estimated by 2.3%. These findings suggest that high TiO_2 nanoparticles doping level inserted in the cement matrix decreases the porosity of the cement microstructure and promotes the formation of hydration products by consumption of capillary water displaced out of the pores.

- Extending the preceding point, further analysis of TGA results show that 1:10 TiO_2/Cement systems contain a substantially higher C-S-H content, by 78%, which indicates an induced formation of this hydration product by the presence of a high doping level of TiO_2 nanoparticles in the cement paste.

- Morphology observations reveal preferential deposition of titania nanoparticles inside the micropores of the cement paste microestructure, which explains the observed decrease in the degree of hydration for low doping levels. For high additions of TiO_2 nanoparticles, micrographs reveal that titania nanoparticles act

as nucleation centres for inner C-S-H formation, along with fibrillar outer C-S-H gel bridging the nucleation sites and therefore developing a network-like morphology.

- Photocatalytic studies indicate that some photoreactions take place within the TiO_2 doped cement, reactions that appear to be less significant for low doping levels of titania nanoparticles, although still an enhacenment of $\approx$ 30% in photocatalytic activity is observed at the lowest doping. At the highest, 1:10 TiO_2/Cement weigth ratio, the highest photocatalytic activity is obtained exhibing a $\approx$ 52% degradation of MB concentration. High amounts of titania nanoparticles provide the system with a large specific surface area, which results in a higher photocatalytic efficiency.

- On the basis of the titania nanoparticles doping levels studied hereby, it is observed that the MB degradation rate does not reach saturation for TiO_2 nanoparticles loading, suggesting that there are still MB molecules available for absorption if an increased number of TiO_2 nanoparticles was to be added above the highest concentration.

- A Second-order kinetics model is found to satisfactory describe the observed MB degradation process. The plots indicate that the rate controlling step is intra-particle diffusion, which is in fact the kinetic mechanism follow by the hydrating particles in the cement paste at the studied hydration period.

- We can conclude that the TiO_2/cement system is photoactive and the highest photocatalytic activity was obtained under the proportion: 1 part of TiO_2 over 10 parts of cement paste, in mass. TiO_2 nanoparticles embedded in the cement matrix not only supply the system with photocatalytic properties, but also promote the formation of C-S-H gel.

CHAPTER 7

Conclusions and Future Perspectives

The detailed discussion and specific conclusions for each part of the current thesis were presented in the relevant chapters. The most important achievements are the suitability of TiN thin films for corrosion protection in reinforced concrete, the microstructure characterization of cement paste at the TiN/cement interface, the possibility of providing photocatalytic properties to the cement paste by adding TiO_2 nanoparticles prepared by the sol-gel technique and the characterization of the cement paste microstructure after the addition of TiO_2 nanoparticles. Here, the main findings of the different parts of this study are summarized. Future research lines are proposedin order to advance on the knowledge of the TiN/cement interface and TiO_2 modified cement systems. The final section of this chapter reports some final concluding remarks.

7.1 Conclusions

This thesis project was designed to apply the use of revolutionary nanotechnology techniques in the development of new advanced, 'tailor-made' cement based systems. Some of the main controversial issues in cement science were identified. A comprehensive research study was planned in order to examine the key features of the TiN/cement interface and TiO_2 modified cement systems at the nano level. Several advanced analytical tools were employed in order to corroborate the observations in each section. The fundamental achievements of the current work are mentioned briefly as follows:

Interface between Cement Paste and TiN Thin Film

The interface between cement paste and TiN thin film at different curing temperatures has been studied for the first time. Nanostructural investigations using XRD, TGA/TG and SEM were conducted in the cement side of the interface. Nanostructural characterization by XRD, XPS, SEM and HRTEM were performed on the TiN side of the interface. A laboratory model for the structural formation of cement paste hydration products at the interface with TiN thin film has been presented. This model aims to provide information about the microstructural development of the cement paste in contact with magnetron sputtered TiN thin films, which can be potentially used as physical barriers against chloride ingress into reinforcing steel. In view of experimental results and the analyses carried out at the TiN/cement interface, the following conclusions were drawn:

Cement Side

- XRD diffractograms along with TGA analyses, which provide quantitative information about the content of hydration products, offered evidence of better crystallization of portlandite crystals in the cement paste cured on the TiN thin film. The higher amount of $Ca(OH)_2$ crystals on the surface of the TiN film, features a preferred orientation of the crystallites on the TiN film, being the plane (001) preferential with respect to (101) at the cement/TiN interface. The index of orientation was found to decrease when higher than ambient temperature was applied to cure the cement paste,which suggests that a critical temperature of anchorage release must be reached so that the crystallites can move under a frictional force related to interfacial viscosity. Further increase in temperature results in an increase of the orientation index of portlandite crystals, which seems to imply that thermally activated rotation of portlandite crystallites is possible under further annealing.

- Assuming that a local increase of the water/cement ratio occured at the interface between cement and TiN, a certain number of ions were given off in the aqueous phase after a corresponding amount of cement was dissolved. In the case presented here, the hydration degree of cement in the interface with TiN was measured and found to be clearly larger than that of cement cured without contact with TiN. Thus, it can be assumed that ion concentration is favoured by TiN contact, therefore a favorable migration of Ca^{2+} ions was produced, promoting $Ca(OH)_2$ crystal formation at the interface. It can be concluded that the effect of TiN-coating on reinforced concrete is likely to promote the desirable passive layer formation.

- Curing temperature also affects the hydratio rate of the overall system. Temperature related-changes were observed in both the morphology of the reaction products and the degree of hydration, which increased with higher temperature. SEM analysis showed that needle-shape ettringite crystals of $1 - 2$ μm length were formed in the interface between cement and TiN, rather fewer and smaller than those observed in cement paste cured without TiN contact. This effect can be explained by the large content of $Ca(OH)_2$, which reduces the formation and the size of the ettringite crystals. There is no thermal treatment associated with these observed reduced-sized ettringite crystals, therefore this fact might only be held as a result of the presence of TiN coating.

TiN Side

- The hydration of cement paste on the surface of TiN thin films does not noticeably affect the microstructure and crystalline nature of TiN, as confirmed by XRD diffration patterns. Only slight lattice parameter distorsions were found in the crystal arragement as a consequence of the different thermal expansion coefficients of cement and TiN. HRTEM observations identified columnar structures of nanosized TiN crystals with preferential growth direction perpendicular to the

Si/TiN interface, which is characteristic of magnetron-sputtered TiN thin films. The presence of cement hydration products on the film did not modify the TiN structure.

- Quantitative analyses by XPS along with XRD diffractograms provided evidence of a nucleation of Ca compounds in the TiO/cement interface cured at 60°C. At higher temperatures, the preferential nucleation of Ca turned out to be in the form of calcite. Thermal shocking at the interface of samples cured at 60°C was revealed by the presence of gypsum and sulphur in the XRD and XPS results, respectively.

- Crystalline clusters of C-S-H were found at the interface between TiN/cement, inserted in the mostly amorphous struture of the cement side. The nanoparticles were found to be between 4 and 5 *nm* in size. Interplanar distances of 2.1 Å were measured by FFT, which might correspond to a crystalline phase of C-S-H. EDX spectra from selected areas showed that the phase was rich in Si, Ca and Al, which gives some soundness to our hypothesis. The results showed to be compatible with a crystalline phase of C-S-H, according with the *colloidal model* on C-S-H nanostructure.

- High corrosion resistance in chrolide environment was assessed in TiN/cement interfaces by the potentiodynamic polarization results. The TiN/cement interface featured higher corrosion resistance than TiN bare films. It can be concluded that hydrating cement paste on the surface of TiN thin film has a possitive effect on the corrosion behaviour of the film, as the hydration products obstruct the corrosion process at the interface between the film and the cement paste.

Addition of Titania Nanoparticles in the Cement Matrix

For the first time, TiO_2 nanoparticles prepared by the sol-gel technique were inserted in fresh cement paste with differing concentrations. The microestructure of the TiO_2/Cement system was studied by using XRD, TGA/TG and SEM. The photocatalytic activity of the so-formed system was analysed by means of the degradation of methylene blue aqueous solutions under UV irradiation. The following conclusions were drawn from the results presented hereby:

- The mineralogical composition of hydrated phases in the cement paste was not noticeably altered by the addition of titania nanoparticles in the cementitious material, nor were their crystallographic properties significantly affected by the addition of TiO_2 nanoparticles. Furthermore, no influence on the characteristic temperatures of the thermal degradation of cement hydrated phases was found from the experimental results. This is an indication that the sol-gel sinthesized TiO_2 nanoparticles embedded in the cement matrix did not impede the system from progressing normally in every hydration stage.

- Concerning the hydration rate of the TiO_2/Cement system, an effect due to the dosage of TiO_2nanoparticles on the degree of hydration was observed. Low loadings of titania produced a gradual decrease in the hydration degree, whereas high dosage resulted in a significant increase in the aforementioned hydration parameter. It can be concluded that high TiO_2 nanoparticles doping level inserted in the cement matrix promotes the formation of hydration products by consumption of water within the cement paste microstructure.

- Extending the preceding point, further analysis by XRD and TGA have showed that high doping levels of titania nanoparticles promoted a substantially higher C-S-H content, by 78%, which indicates an induced formation of this hydration product due to the presence of a high doping level of TiO_2 nanoparticles in the cement paste.

- Morphology observations revealed preferential deposition of titania nanoparticles inside the micropores of the cement paste microstructure, which explains the observed decrease in the hydration degree for low doping levels. For high additions levels of TiO_2 nanoparticles, micrographs revealed that titania nanoparticles acted as nucleation centres for inner C-S-H formation, along with fibrillar outer C-S-H gel bridging the nucleation sites and therefore developing a network-like morphology.

- Photocatalytic studies indicated that some photoreactions took place within the TiO_2 doped cement, reactions that appeared to be less significant for lower doping levels of titania nanoparticles, although still an enhacenment of $\approx$ 30% in photocatalytic activity was observed at the lowest doping. At the highest doping level, the highest photocatalytic activity was obtained exhibing a $\approx$ 52% degradation rate increase for MB. Large amounts of titania nanoparticles provide the system with a more homogeneous surface microstructure and hence larger specific surface area, which results in a higher photocatalytic efficiency.

- On the basis of the titania nanoparticles doping levels studied herein, it was observed that the MB degradation rate did not reach saturation for TiO_2 nanoparticle loading, suggesting that there were still MB molecules available for absorption if an increased number of TiO_2 nanoparticles had been added above the highest concentration.

- A Second-order kinetic model was found to satisfactory describe the observed MB degradation process. The linearity of the plots indicated that the rate controlling step is intraparticle diffusion, which is in fact the kinetic mechanism followed by the hydrating particles in the cement paste at the hydration period under examination.

- Evidence of photoactivity in the TiO_2/cement system was found and the highest photocatalytic activity was obtained under the proportion: 1 part of TiO_2 over

10 parts of cement paste, in mass. It can be concluded that TiO_2 nanoparticles embedded in the cement matrix not only supply the system with photocatalytic properties, but also promote the formation of C-S-H gel.

7.2 Future Perspectives

Despite a great deal of research on the nature and properties of cement systems, relatively few are focused on the interactions between the cementitious material and Ti-based nanostructures. Relating to interfaces between cement paste and TiN thin film, to our knowledge, there are no other works reported which may combine the originality of the investigation presented in this doctoral thesis. Nevertheless, various aspects of the characteristics and behavior of TiN/Cement interface still require further study. In the other hand, a number of studies on the addition of TiO_2 particles into cement paste have been compared and shown to be in agreement with the results presented here. However, working with sol-gel sinthesized TiO_2 nanoparticles is a novel technique and this thesis has proven its suitability for providing photocatalytic properties to the cement paste. The advancements in experimental methods provide an opportunity to re-examine and elucidate some of the debated issues in cement and concrete science. A couple of relevant fields that merit detailed investigation in the future are suggested as follows:

1. The methods developed in the current thesis regarding the study of the changes in various nanostructural features of cement paste hydrating products at the interface with TiN at different temperatures can be employed in conjunction with other experimental tools in order to understand new aspects of the behavior of C-S-H and the role of $Ca(OH)_2$ in its nanostructure. For example, high resolution 1H NMR, further HRTEM imaging, Rutherford Backscattering Spectrometry and Raman spectroscopy may be proven useful.

2. An analysis of the TiN/Cement interface after Ar ion etching would allow to

extract suplementary information on the state of the TiN interface and identify possible alteration of the layer during the cement curing.

3. The C-S-H is well known to be an important parameter in the development of the mechanical properties of the cement system. It is proposed that a complete set of interface between TiN and cement paste samples be prepared utilizing various hydration periods and curing temperatures. The engineering performance of C-S-H can thus be studied as this material undergoes ageing using various methods such as nanoindentation. This has important practical implications for the service life design of concrete structures.

4. The addition of sol-gel sinthesized TiO_2 nanoparticles was interpreted as an effective method to induce the formation of hydration products in Portland cement paste, as C-S-H seeding was observed in the microstructure. This has opened up several opportunities for pursing various aspects of TiO_2 modified cement systems. The C-S-H seeding effect can be explored in parallel with the effect of chemical admixtures such as retarders in order to investigate the possibility of controlling the delay of cement hydration and therefore favouring the photocatalytic activity. Also, the durability and mechanical characteristics of TiO_2 modified paste needs to be evaluated.

5. The current doctoral project investigated various nanostructural properties of TiO_2/cement paste systems upon the addition of several concentration of TiO_2 nanoparticles. It could be interesting to conduct similar studies on the hydration of the TiO_2/cement system upon different water/cement ratio and study the change of various properties as water molecules possibly enter the nanostructural locations including the porous region, where the TiO_2 nanoparticles were found to be located. Such investigation should also provide insight into the photocatalytic activity of such cement systems.

7.3 Concluding Remarks

This doctoral thesis has successfully explored the used of nanotecnology on construction materials by the utilization of Ti-based nanostructures for modification of cement paste. TiN thin films effectively provide physical protection to reinforcing steel in concrete against chloride-induced corrosion. The cement paste in contact with TiN develops adhesion phases which enrich the passive layer and therefore provide further protection to the whole structure. Novel environment-friendly cement paste with photocatalytic properties is developed by the addition of sol-gel synthezised TiO_2 nanoparticles into the cement matrix from the first stage of hydration. TiO_2 nanoparticles provide the cement system not only with photocatalytic activity but also promote the formation of C-S-H gel, which is, ultimately, the phase responsible for the mechanical performance of cement-based construction materials.

Bibliography

[Agrios 2005] A. Agrios and P. Pichat. *State of the art and perspectives on materials and applications of photocatalysis over TiO_2;*. Journal of Applied Electrochemistry, vol. 35, pages 655–663, 2005. (Cited on page 88.)

[Aksu 2003] Z. Aksu and D. Dönmez. *A comparative study on the biosorption characteristics of some yeasts for Remazol Blue reactive dye*. Chemosphere, vol. 50, no. 1, pages 1075 – 1083, 2003. (Cited on page 105.)

[Alarcon-Ruiz 2005] Lucia Alarcon-Ruiz, Gerard Platret, Etienne Massieu and Alain Ehrlacher. *The use of thermal analysis in assessing the effect of temperature on a cement paste*. Cement and Concrete Research, vol. 35, no. 3, pages 609–613, March 2005. (Cited on page 61.)

[Allen 2000] A. J. Allen, J. J. Thomas and Jennings H. M. *Composition and density of nanoscale calcium silicate hydrate in cement*. Nature Materials, vol. 6, no. 4, pages 311 – 316, 2000. (Cited on pages 19 and 29.)

[Arin 2011] Melis Arin, Petra Lommens, Nursen Avci, Simon C. Hopkins, Klaartje De Buysser, Ioannis M. Arabatzis, Ioanna Fasaki, Dirk Poelman and Isabel Van Driessche. *Inkjet printing of photocatalytically active TiO2 thin films from water based precursor solutions*. Journal of the European Ceramic Society, vol. 31, no. 6, pages 1067 – 1074, 2011. (Cited on page 29.)

[Asthana 1999] K.K. Asthana, L.K. Aggarwal and Rajni Lakhani. *A novel interpenetrating polymer network coating for the protection of steel reinforcement in concrete*. Cement and Concrete Research, vol. 29, no. 10, pages 1541–1548, October 1999. (Cited on page 24.)

[Łatava 1975] Vladimír Łatava and Otokar Veprek. *Thermal Decomposition of Ettringite Under Hydrothermal Conditions*. Journal of the American Ceramic Society, vol. 58, no. 7-8, pages 357–359, July 1975. (Cited on page 61.)

[Avrami 1939] M. Avrami. *Kinetics of phase change. I.* Journal of Chemical Physics, vol. 7, pages 1103 – 1112, 1939. (Cited on page 20.)

[Beaudoin 2008] J. J. Beaudoin and R. Alizadeh. *Discussion of the paper ŚRefinements to colloid model of C-S-H in cement: CM-II,Š by Jennings H. M.* Cement and Concrete Research, vol. 38, no. 7, pages 1026 – 1027, 2008. (Cited on page 16.)

[Bendavid 2000] A. Bendavid, P.J. Martin and H Takikawa. *Deposition and modification of titanium dioxide thin films by filtered arc deposition*. Thin Solid Films, vol. 360, pages 241–249, 2000. (Cited on page 9.)

[Blake 1997] D.M. Blake. Bibliography of work on the photocatalytic removal of hazardous compounds from water and air. NREL/TP-430-22197, National Renewable Energy Laboratory, Golden Co., 1997. (Cited on page 88.)

[Bland 1990] C.H. Bland and J.H. Sharp. *Chemistry of Portland cement - gasifier slag interactions*. Advances in Cement Research, vol. 3, no. 11, pages 91 – 98, 1990. (Cited on page 61.)

[Bogue 1929] R. H. Bogue. *Calculation of the compounds in Portland cement*. Industrial and Engineering Chemistry, Analytical Edition, no. 1, pages 192–197, 1929. (Cited on pages 3 and 64.)

[Bonaccorsiw 2005] E. Bonaccorsiw and S. Merlino. *The crystal structure of tobermorite 14 Å (Plombierite), a C-S-H phase*. Jounal of the American Ceramic Society, vol. 88, no. 3, pages 505–512, 2005. (Cited on page 17.)

[Breugel 1991] K. Van Breugel. Simulation of hydration and formation of structure in hardening cement-based materials, phd thesis. Technical University of Delft, Netherlands, 1991. (Cited on page 107.)

[Brown 1978] W.D. Brown and W.W. Grannemann. *C-V characteristics of metal-titanium dioxidesilicon capacitors*. Solid-State Electronics, vol. 21, pages 837–846, 1978. (Cited on page 9.)

[Buyle 2005] G. Buyle. Simplifed model for the dc planar magnetron discharge, phd thesis. Ghent University, 2005. (Cited on page 38.)

[Carp 2004] O. Carp, C.L. Huisman and A. Reller. *Photoinduced reactivity of titanium dioxide*. Progress in Solid State Chemistry, vol. 32, no. 1Ű2, pages 33 – 177, 2004. (Cited on page 9.)

[Cassar 2003] L. Cassar, C. Pepe, G. Tognon, G. L. Guerrini and R. Amadelli. *White cement for architectural concrete, possessing photocatalytic properties*. In Proceedings of the 11th International Congress on the Chemistry of Cement. Durban, South Africa, pages 1–11, 2003. (Cited on pages xii, 30 and 31.)

[Castellote 2004] Marta Castellote, Cruz Alonso, Carmen Andrade, Xavier Turrillas and Javier Campo. *Composition and microstructural changes of cement pastes upon heating, as studied by neutron diffraction*. Cement and Concrete Research, vol. 34, no. 9, pages 1633–1644, September 2004. (Cited on page 59.)

[Chatelier 1905] H. Le Chatelier. Experimental researches on the constitution of hydraulic mortars, phd thesis. Mc Graw Publising Company Co. NY, 1905. (Cited on page 3.)

[Chen 2005] X. H. Chen. *Corrosion behavior of carbon nanotubes-Ni composite coating*. Surface and Coatings Technology, vol. 2-3, pages 351–356, 2005. (Cited on page 25.)

[Claisse 2005] P. Claisse. *Transport Properties of Concrete*. Concrete International, vol. 27, no. 1, pages 43–48, 2005. (Cited on page 24.)

[Clark 1968] R.J.H. Clark. The chemistry of titanium and vanadium. Elsevier, Amsterdam, 1968. (Cited on page 9.)

[Cotton 1988] F.A. Cotton and Wilkenson G. Advanced inorganic chemistry, 5th edition. Wiley-Interscience, Chichester, 1988. (Cited on page 10.)

[C.R. 1964] C.R. and Houska. *Thermal expansion and atomic vibration amplitudes for TiC, TiN, ZrC, ZrN, and pure tungsten*. Journal of Physics and Chemistry of Solids, vol. 25, no. 4, pages 359 – 366, 1964. (Cited on page 73.)

[Czernin 1980] W Czernin. Cement chemistry and physics for civil engineers, 2rd english edition. Foreign Publications Inc, New York, 1980. (Cited on page 64.)

[Dalziel 1986] J.A Dalziel and W.A. Gutteridge. *The influence of pulverized-fuel ash upon the hydration characteristics and certain physical properties of a Portland cement paste*. Cement and Concrete Association, Technical Report, vol. 560, 1986. (Cited on page 20.)

[Depla 2008] D Depla and S. Mahieu. Reactive sputter deposition. Springer-Verlag Berlin Heidelberg, 2008. (Cited on page 38.)

[Detwiler 1988] Rachel J. Detwiler, Paulo J.M. Monteiro, Hans-Rudolf Wenk and Zengqiu Zhong. *Texture of calcium hydroxide near the cement paste-aggregate interface*. Cement and Concrete Research, vol. 18, no. 5, pages 823–829, September 1988. (Cited on page 60.)

[Dominguez 1998] C. Dominguez, J. Garcia, M.A. Pedraz, A. Torres and M.A. Galan. *Photocatalytic oxidation of organic pollutants in water*. Catalysis Today, vol. 40, no. 1, pages 85 – 101, 1998. (Cited on page 29.)

[Dweck 2000] Jo Dweck, Pedro Mauricio Buchler, Antonio Carlos Vieira Coelho and Frank K Cartledge. *Hydration of a Portland cement blended with calcium carbonate*. Thermochimica Acta, vol. 346, no. 1-2, pages 105 – 113, 2000. (Cited on page 62.)

[Feldman 1968] R. F. Feldman and P. J. Sereda. *A model for hydrated Portland cement paste as deduced from sorption-length change and mechanical properties*.

Matériaux et Construction, vol. 1, no. 6, pages 509 – 520, 1968. (Cited on page 19.)

[Feldman 1971] R.F. Feldman and V.S. Ramachandran. *Differentiation of interlayer and adsorbed water in hydrated Portland cement by thermal analysis*. Cement and Concrete Research, vol. 16, pages 607 – 620, 1971. (Cited on pages 16 and 19.)

[Frank 1977] S.N. Frank and A.J. Bard. *Heterogeneous photocatalytic oxidation of cyanide ion in aqueous solutions at titanium dioxide powder*. Journal of the American Chemical Society, vol. 99, no. 1, pages 303–304, 1977. (Cited on page 29.)

[Fujishima 1972] A. Fujishima and K. Honda. *Electrochemical photolysis of water at a semiconductor electrode*. Nature, vol. 238, pages 37–38, 1972. (Cited on page 29.)

[Gallucci 2007] E. Gallucci and K. Scrivener. *Crystallisation of calcium hydroxide in early age model and ordinary cementitious systems*. Cement and Concrete Research, vol. 37, no. 4, pages 492–501, April 2007. (Cited on page 6.)

[García-Alonso 2007] M.C. García-Alonso, M.L. Escudero, J.M. Miranda, M.I. Vega, F. Capilla, M.J. Correia, M. Salta, A. Bennani and J.A. González. *Corrosion behaviour of new stainless steels reinforcing bars embedded in concrete*. Cement and Concrete Research, vol. 37, no. 10, pages 1463–1471, October 2007. (Cited on page 24.)

[Gartner 2002] E. M. Gartner, J.F. Young, D.A. Damidot and I. Jawed. Hydration of portland cement. Spon Press, London, 2 édition, 2002. (Cited on page 5.)

[Ge 2008] Z. Ge and Z. Gao. *Applications of Nanotechnology and Nanomaterials in Construction*. In Proceedings of the First International Conference of Construction in Developed Countries, pages 235–240, 2008. (Cited on page 23.)

[Goldstein 2003] J. Goldstein. Scanning electron microscopy and x-ray microanalysis, volumen 1. Springer, 2003, 3 édition, 2003. (Cited on page 47.)

[Gordon 1997] R. Gordon. *Chemical vapor deposition of coatings on glass*. Journal of Non-Crystalline Solids, vol. 218, no. 0, pages 81 – 91, 1997. (Cited on page 26.)

[Greenberg 1954] S.A. Greenberg. *Calcium Silicate Hydrate (I)*. Journal of Physical Chemistry, vol. 58, no. 4, pages 362–367, 1954. (Cited on page 15.)

[Grela 1996] M.A. Grela and A.J. Colussi. *Kinetics of Stochastic Charge Transfer and Recombination Events in Semiconductor Colloids. Relevance to Photocatalysis Efficiency*. The Journal of Physical Chemistry, vol. 100, no. 46, pages 18214–18221, 1996. (Cited on page 102.)

[Guirado 1998] F. Guirado, S. Galiť and J.S. Chinchón. *Thermal Decomposition of Hydrated Alumina Cement (CAH10)*. Cement and Concrete Research, vol. 28, no. 3, pages 381–390, 1998. (Cited on page 62.)

[Hamid 1981] S.A. Hamid. *he crystal structure of the 11 Å natural tobermorite Ca2.25[Si3O7.5(OH)1.5].1H2O*. Zeitschrift für Kristallograohie, vol. 154, pages 189–198, 1981. (Cited on page 16.)

[Hass 1952] G. Hass. *Preparation, properties and optical applications of thin films of titanium dioxide*. Vacuum, vol. 2, no. 4, pages 331–345, 1952. (Cited on page 9.)

[Heinz 1986] D. Heinz and U. Ludwig. *Mechanism of subsequent ettringite formation in mortars and concretes after heat treatment*. Proc. Int. Congr. Chem. Cem., 8th,, vol. 5, no. Rio de Janeiro, pages 189 – 194, 1986. (Cited on page 66.)

[Hester 2007] R.E. Hester, R.M. Harrison and R.S.O.C. Britain. *Nanotechnology: consequences for human health and the environment*. Royal Society of Chemistry, 2007. (Cited on page 25.)

[Howald 2008] T. Howald. *Influence of Carbon Nanotubes on the Micromechanical Properties of a Model System for Ultra-Hight Performance Concrete*. In Proceedings of the Second International Symposium on Ultra High Performance Concrete, Kassel, Germany. kassel university press GmbH, 2008. (Cited on page 27.)

[Jayapalan 2009] A. R. Jayapalan, B. Y. Lee and K. E. Kurtis. *Effect of Nano-sized Titanium Dioxide on Early Age Hydration of Portland Cement*. In Nanotechnology in Construction 3, pages 267–273. Springer Berlin Heidelberg, 2009. (Cited on page 32.)

[Jenkins 1996] R. Jenkins and R.L. Snyder. Introduction to x-ray powder diffractometry. Wiley, New York, 1996. (Cited on page 44.)

[Jennings 2000] Hamlin M. Jennings. *A model for the microstructure of calcium silicate hydrate in cement paste*. Cement and Concrete Research, vol. 30, no. 1, pages 101 – 116, 2000. (Cited on page 18.)

[Jennings 2008a] H. M. Jennings. *Reply to the discussion by J.J. Beaudoin and R. Alizeadab of the paper ŞRefinements to colloid model of CŰSŰH in cement: CM-II*. Cement and Concrete Research, vol. 38, no. 7, pages 1028 – 1030, 2008. (Cited on page 16.)

[Jennings 2008b] Hamlin M. Jennings. *Refinements to colloid model of C-S-H in cement: CM-II*. Cement and Concrete Research, vol. 38, no. 3, pages 275 – 289, 2008. (Cited on pages 16 and 18.)

[J.I 2003] J.I and Escalante-Garcia. *Nonevaporable water from neat OPC and replacement materials in composite cements hydrated at different temperatures*. Cement and Concrete Research, vol. 33, no. 11, pages 1883 – 1888, 2003. (Cited on page 65.)

[Jindal 1999] P.C Jindal, A.T Santhanam, U Schleinkofer and A.F Shuster. *Performance of PVD TiN, TiCN, and TiAlN coated cemented carbide tools in turning*. International Journal of Refractory Metals and Hard Materials, vol. 17, no. 1-3, pages 163–170, May 1999. (Cited on page 26.)

[Keshmiri 2006] M. Keshmiri, T. Troczynski and M. Mohseni. *Oxidation of gas phase trichloroethylene and toluene using composite solŰgel TiO2 photocatalytic coatings*. Journal of Hazardous Materials, vol. 128, no. 2Ű3, pages 130 – 137, 2006. (Cited on page 34.)

[Khoury 1992] G.A. Khoury. *Compressive strength of concrete at high temperatures: a reassessment*. Magazine of Concrete Research, vol. 44, no. 161, pages 291 – 309, 1992. (Cited on page 96.)

[Kim 1999] J.H. Kim, S. Lee and H.-S. Im. *The effect of different ambient gases, pressures, and substrate temperatures on TiO2 thin films grown on Si(100) by laser ablation technique*. Applied Physics A, vol. 69, pages 629–632, 1999. (Cited on page 9.)

[Larbi 1990] J.A. Larbi and J.M.J.M. Bijen. *Orientation of calcium hydroxide at the portland cement paste-aggregate interface in mortars in the presence of silica fume: A contribution*. Cement and Concrete Research, vol. 20, no. 3, pages 461–470, May 1990. (Cited on page 59.)

[Lee 2009] J. Lee, S. Mahendra and P.J.J. Alvarez. *Potential Environmental and Human Health Impacts of Nanomaterials Used in the Construction Industry*. In Proceedings of the 3rd International Symposium on Nanotechnology in Construction (NICOM3), pages 203–210. Springer Verlag, 2009. (Cited on page 22.)

[Lee 2010] B.Y. Lee and K.E. Kurtis. *Influence of TiO2 Nanoparticles on Early C3S Hydration*. Journal of the American Ceramic Society, vol. 93, no. 10, pages 3399–3405, 2010. (Cited on page 32.)

[Li 2004] G.Y. Li. *Properties of high-volume fly ash concrete incorporating nano-SiO_2*. Cement and Concrete Research, vol. 34, no. 6, pages 1043 – 1049, 2004. (Cited on page 23.)

[Lin 2006] H. Lin, C.P. Huang, W. Li, C. Ni, S. Ismat Shah and Y.H. Tseng. *Size dependency of nanocrystalline TiO2 on its optical property and photocatalytic reactivity exemplified by 2-chlorophenol*. Applied Catalysis B: Environmental, vol. 68, no. 1Ű2, pages 1 – 11, 2006. (Cited on page 102.)

[Mahshid 2007] S. Mahshid, M. Askari and M.S. Ghamsari. *Synthesis of TiO2 nanoparticles by hydrolysis and peptization of titanium isopropoxide solution*. Journal of Materials Processing Technology, vol. 189, no. 1Ű3, pages 296 – 300, 2007. (Cited on page 35.)

[Makar 2005] J. Makar, J. Margeson and J. Luh. *Carbon nanotube/cement composites Ű early results and potential applications*. In Proceedings of the 3rd Int. Conf. on Construction Materials: Performance, Innovations, and Structural Implications, Vancouver, B.C., pages 1–10, 2005. (Cited on pages 23 and 27.)

[Mammoliti 1999] L. Mammoliti, C.M. Hansson and B.B. Hope. *Corrosion inhibitors in concrete Part II: Effect on chloride threshold values for corrosion of steel in synthetic pore solutions*. Cement and Concrete Research, vol. 29, no. 10, pages 1583–1589, October 1999. (Cited on page 24.)

[Manso-Silvan 2002] M. Manso-Silvan, J. M. Martinez-Duart, S. Ogueta, P. Garcia-Ruiz and J. Perez-Rigueiro. *Development of human mesenchymal stem cells on DC sputtered titanium nitride thin films*. Journal of Materials Science: Materials in Medicine, vol. 13, pages 289–293, 2002. (Cited on page 26.)

[Manso 2001] M. Manso. Hap/tio$_2$ and hap/tin structures; surface modifications for enhanced biocompatibility. phd thesis. Universidad Autónoma de Madrid, 2001. (Cited on page 38.)

[Martin-Palma 2003] R.J. Martin-Palma, M. Manso, J. M. Martinez-Duart, A. Conde and J.J. Damborenea. *Corrosion behavior of sputter-deposited TiN thin films*. Journal of Vacuum Science and Technology A, vol. 21, pages 1635–1639, 2003. (Cited on pages 26 and 82.)

[Maruyama 2011] I. Maruyama and A. Teramoto. *Impact of time-dependant thermal expansion coefficient on the early-age volume changes in cement pastes*. Cement and Concrete Research, vol. 41, no. 4, pages 380 – 391, 2011. (Cited on page 73.)

[Maury Ramirez 2010] A. Maury Ramirez, K. Demeestere, N. De Belie, T. Mäntylä and E. Levänen. *Titanium dioxide coated cementitious materials for air purifying purposes: Preparation, characterization and toluene removal potential*. Building and Environment, vol. 45, no. 4, pages 832 – 838, 2010. (Cited on page 88.)

[Maury-Ramirez 2011] A. Maury-Ramirez, K. Demeestere and N. De Belie. *Photocatalytic activity of titanium dioxide nanoparticle coatings applied on autoclaved aerated concrete: Effect of weathering on coating physical characteristics and gaseous toluene removal*. Journal of Hazardous Materials, no. 0, pages –, 2011. (Cited on page 30.)

[Maury 2010] A. Maury and N. De Belie. *State of the art of TiO2 containing cementitious materials: self-cleaning properties*. Materiales de Construcción, vol. 60, no. 298, pages 33 – 50, 2010. (Cited on page 30.)

[Megaw 1956] H.D. Megaw and C.H. Kelsey. *Crystal structure of tobermorite*. Nature, vol. 177, pages 390–391, 1956. (Cited on page 16.)

[Mehta 1976] P.K. Mehta. *Scanning electron micrographic studies of ettringite formation*. Cement and Concrete Research, vol. 6, no. 2, pages 169 – 182, 1976. (Cited on page 66.)

[Mehta 2006] P.K. Mehta and Monteiro P.J.M. Concrete; microstructure, properties and materials, 3rd edition. McGraw-Hill, 2006. (Cited on page 15.)

[Mitsuo 2000] Atsushi Mitsuo, Kazutaka Kanda and Tatsuhiko Aizawa. *Friction and wear properties of carbon-ion implanted titanium nitride films*. Surface and Coatings Technology, vol. 128Ű129, no. 0, pages 440 – 445, 2000. (Cited on page 26.)

[Mitsuo 2002] A. Mitsuo and T. Aizawa. *Effect of chlorine distribution profiles on tribological properties for chlorine-implanted titanium nitride films*. Surface and Coatings Technology, vol. 158Ű159, no. 0, pages 694 – 698, 2002. (Cited on page 26.)

[Mohan 1981] K. Mohan and H.F.W. Taylor. *Analytical Electron Microscopy of Cement Pastes: III, Pastes Hydrated for Long Times*. Journal of American Ceramic Sociaty, vol. 64, no. 6, pages 319 – 321, 1981. (Cited on page 91.)

[Monteiro 1985] P.J.M. Monteiro, O.E. Gjorv and P.K. Mehta. *Microstructure of the steel-cement paste interface in the presence of chloride*. Cement and Concrete Research, vol. 15, no. 5, pages 781–784, September 1985. (Cited on page 60.)

[Montes-Hernandez 2010] G. Montes-Hernandez, A. Pommerol, F. Renard, P. Beck, E. Quirico and O. Brissaud. *In situ kinetic measurements of gas?solid carbonation of Ca(OH)2 by using an infrared microscope coupled to a reaction cell*. Chemical Engineering Journal, vol. 161, no. 1-2, pages 250 – 256, 2010. (Cited on page 62.)

[Mounanga 2004] P. Mounanga, A. Khelidj, A. Loukili and V. Baroghel-Bouny. *Predicting Ca(OH)2 content and chemical shrinkage of hydrating cement pastes*

using analytical approach. Cement and Concrete Research, vol. 34, no. 2, pages 255 – 265, 2004. (Cited on page 64.)

[Muggli 1998] D.S. Muggli, J.T. McCue and J.L. Falconer. *Mechanism of the Photocatalytic Oxidation of Ethanol on TiO2*. Journal of Catalysis, vol. 173, no. 2, pages 470 – 483, 1998. (Cited on page 34.)

[Nazari 2010] A. Nazari, S. Riahi, S. Riahi, S.F. Shamekhi and A. Khademno. *Assessment of the effects of the cement paste composite in presence TiO2 nanoparticles*. Journal of American Science, vol. 6, no. 4, pages 43 – 46, 2010. (Cited on pages 32 and 88.)

[Nazari 2011] A. Nazari and Riahi S. *TiO2 nanoparticles effects on physical, thermal and mechani-cal properties of self compacting concrete with ground granulated blast furnace slag as binder*. Energy and Buildings, vol. 43, pages 995 – 1002, 2011. (Cited on page 96.)

[Neville 2000] A. Neville. *Water and Concrete: A Love-Hate Relationship*. Concrete International, vol. 22, no. 12, pages 34 – 38, 2000. (Cited on page 15.)

[Nonat 1994] A. Nonat. *Interactions between chemical evolution (hydration) and physical evolution (setting) in the case of tricalcium silicate*. Materials and Structures, vol. 27, no. 4, pages 187 – 195, 1994. (Cited on page 15.)

[Ormellese 2006] M. Ormellese, M. Berra, F. Bolzoni and T. Pastore. *Corrosion inhibitors for chlorides induced corrosion in reinforced concrete structures*. Cement and Concrete Research, vol. 36, no. 3, pages 536–547, March 2006. (Cited on page 24.)

[Oyama 1996] S.T. Oyama. The chemistry of transition metal carbides and nitrides. Blackie Academic and Professional, New York, 1996. (Cited on page 8.)

[Paulik 1992] F. Paulik, J. Paulik and M. Arnold. *Thermal decomposition of gypsum*. Thermochimica Acta, vol. 200, no. 0, pages 195–204, July 1992. (Cited on page 61.)

[Pellenq 2008] R.J.M. Pellenq, N. Lequeux and H. Van Damme. *Engineering the bonding scheme in CŰSŰH: The iono-covalent framework*. Cement and Concrete Research, vol. 38, pages 159 – 174, 2008. (Cited on page 16.)

[Pierre 1998] A.C. Pierre. Introduction to sol-gel processing. Kluwer Academic Publishers, Boston/Dordrech/London, 1998. (Cited on page 34.)

[Pierson 1996] H.O. Pierson. The handbook of refractory nitrides and carbides. Noyes Publ., New York, 1996. (Cited on pages 8 and 9.)

[Powers 1947] T.C. Powers and T. L. Brownyard. *Studies of the physical properties of hardened Portland cement paste*. ACI Journal Proc., vol. 43, pages 101 – 933, 1947. (Cited on page 19.)

[Pruden 1983] A.L. Pruden and D.F. Ollis. *Photoassisted heterogeneous catalysis: The degradation of trichloroethylene in water*. Journal of Catalysis, vol. 82, no. 2, pages 404 – 417, 1983. (Cited on page 29.)

[Punzon-Quijorna 2011] E. Punzon-Quijorna, V. Torres-Costa, F. Agullo-Rueda, P. Herrero-Fernandez, A. Climent, F. Rossi and M. Manso-Silvan. *TiNxOy/TiN dielectric contrasts obtained by ion implantation of O2+; structural, optical and electrical properties*. Journal of Physics D: Applied Physics, vol. 44, no. 23, 2011. (Cited on page 73.)

[Ramachandran 1969] V. S. Ramachandran. Applications of differential thermal analysis in cement chemistry. Chemical Publishing Co., NY, 1969. (Cited on page 41.)

[Ramachandran 1979] V.S. Ramachandran. *Differential thermal method of estimating calcium hydroxide in calcium silicate and cement pastes*. Cement and Concrete Research, vol. 9, no. 6, pages 677 – 684, 1979. (Cited on page 15.)

[Rayment 1982] D.L. Rayment and A.J. Majumdar. *The composition of the C-S-H phases in portland cement pastes*. Cement and Concrete Research, vol. 12, no. 6, pages 753–764, November 1982. (Cited on page 6.)

[Richardson 1999] I.G. Richardson. *The nature of C-S-H in hardened cements*. Cement and Concrete Research, vol. 29, pages 1131 – 1147, 1999. (Cited on page 15.)

[Richardson 2008] I.G. Richardson. *The calcium silicate hydrates*. Cement and Concrete Research, vol. 38, no. 2, pages 137 – 158, 2008. (Cited on pages 16, 17, 18, 80 and 96.)

[RILEM 1987] RILEM. *Mathematical modelling of hydration of cement: Hydration of dicalcium silicate*. Materials and Structures, vol. 20, pages 377–382, 1987. (Cited on page 6.)

[Sanchez 2000] F. Sanchez and K. Sobolev. *Nanotechnology in concrete - A review*. Construction and Building Materials, vol. 24, no. 11, pages 2060 – 2071, 2000. (Cited on page 22.)

[Shamsad 2003] A. Shamsad. *Reinforcement corrosion in concrete structures, its monitoring and service life predictionŰŰa review*. Cement and Concrete Composites, vol. 25, no. 4-5, pages 459–471, May 2003. (Cited on page 24.)

[Sobolev 2005] K. Sobolev and M.F. Gutierrez. *How nanotechnology can change the concrete world*. Journal of American Ceramic Society, vol. 84, pages 16 – 20, 2005. (Cited on page 23.)

[Soylev 2007] T.A. Soylev, C. McNally and M. Richardson. *Effectiveness of amino alcohol-based surface-applied corrosion inhibitors in chloride-contaminated*

concrete. Cement and Concrete Research, vol. 37, no. 6, pages 972–977, June 2007. (Cited on page 24.)

[Sugimoto 2002a] T. Sugimoto and X. Zhou. *Synthesis of Uniform Anatase TiO2 Nanoparticles by the GelŰSol Method: 2. Adsorption of OH- Ions to Ti(OH)4 Gel and TiO2 Particles*. Journal of Colloid and Interface Science, vol. 252, no. 2, pages 347 – 353, 2002. (Cited on page 35.)

[Sugimoto 2002b] T. Sugimoto, X. Zhou and A. Muramatsu. *Synthesis of Uniform Anatase TiO2 Nanoparticles by GelŰSol Method: 1. Solution Chemistry of Ti(OH)n(4-n)+ Complexes*. Journal of Colloid and Interface Science, vol. 252, no. 2, pages 339 – 346, 2002. (Cited on page 35.)

[Suni 1985] I. Suni, M. Blomberg and J. Saarilahti. *Performance of titanium nitride diffusion barriers in aluminum #x2013;titanium metallization schemes for integrated circuits*. Journal of Vacuum Science Technology A: Vacuum, Surfaces, and Films, vol. 3, no. 6, pages 2233 –2236, 1985. (Cited on page 26.)

[Tanaka 1991] K. Tanaka, M.F.V. Capule and T. Hisanaga. *Effect of Crystallinity of TiO_2 on its photocatalytic action*. Chemistry Physics Letters, vol. 187, no. 1-2, pages 73 – 76, 1991. (Cited on page 31.)

[Taty-Costodes 2003] V.C. Taty-Costodes, H. Fauduet, C. Porte and A. Delacroixs. *Removal of Cd(II) and Pb(II) ions, from aqueous solutions, by adsorption onto sawdust of Pinus sylvestris*. Journal of Hazardous Materials, vol. 105, no. 1-3, pages 121 – 142, 2003. (Cited on page 104.)

[Taylor 1950] H.F.W. Taylor. *Hydrated calcium silicates: part I. Compound formation at ordinary temperatures*. Journal of the Chemical Society, pages 3682–3690, 1950. (Cited on page 15.)

[Taylor 1987] H.F.W. Taylor. *A method for predicting alkali ion concentration in cement pore solutions*. Advanced Cement Research, vol. 1, no. 1, pages 5–17, 1987. (Cited on page 20.)

[Taylor 1992] H.F.W. Taylor. *Tobermorite, jennite and cement gel*. Zeitschrift für Kristallograohie, vol. 202, pages 41–50, 1992. (Cited on page 16.)

[Taylor 1993] H.F.W. Taylor. *Nanostructure of C-S-H: Current status*. Advanced Cement Based Materials, vol. 1, no. 1, pages 38–46, October 1993. (Cited on page 6.)

[Taylor 1997] H.F.W. Taylor. Cement chemistry. Thomas Telford, 2nd edition, 1997. (Cited on pages 15, 16, 61, 64, 92 and 94.)

[Tennis 2000] P. D. Tennis and H. M. Jennings. *A Model for Two Types of C-S-H in the Microstructure of Portland Cement Pastes*. Cement and Concrete Research, vol. 30, no. 6, pages 855 – 863, 2000. (Cited on pages 19 and 20.)

[Toth 1971] L.E. Toth. Transition metal carbides and nitrides. Academic, New York, 1971. (Cited on page 8.)

[Tritthart 2003] J. Tritthart. *Transport of a surface-applied corrosion inhibitor in cement paste and concrete*. Cement and Concrete Research, vol. 33, no. 6, pages 829–834, June 2003. (Cited on page 24.)

[Trung 2003] T. Trung, W.J. Cho and C.S. Ha. *Preparation of TiO2 nanoparticles in glycerol-containing solutions*. Materials Letters, vol. 57, no. 18, pages 2746 – 2750, 2003. (Cited on page 35.)

[Vadivelan 2005] V. Vadivelan and K. Vasanth Kumar. *Equilibrium, kinetics, mechanism, and process design for the sorption of methylene blue onto rice husk*. Journal of Colloid and Interface Science, vol. 286, no. 1, pages 90 – 100, 2005. (Cited on page 106.)

[Vaquero 2010] Vanessa Sánchez Vaquero, Alvaro Muñoz Noval, Nuria Tejera Sánchez, María Jesus Pérez Roldán, Andrea Valsesia, Giaccomo Ceccone, Josefa Predestinación García Ruiz, Miguel Manso Silván and Francois Rossi. *Preparation, modification and cellular evaluation of PEGŰPEGd supports with titania nanoparticle loads*. Surface and Interface Analysis, vol. 42, no. 6-7, pages 481–485, 2010. (Cited on pages xii and 36.)

[Vedalakshmi 2003] R Vedalakshmi, A Sundara Raj, S Srinivasan and K Ganesh Babu. *Quantification of hydrated cement products of blended cements in low and medium strength concrete using TG and DTA technique*. Thermochimica Acta, vol. 407, no. 1-2, pages 49–60, December 2003. (Cited on page 62.)

[Vera-Agullo 2009] J. Vera-Agullo. *Mortar and Concrete Reinforced with Nanomaterials*. In 3rd International Symposium on Nanotechnology in Construction (NICOM3, 2009), Prague, Czech Republic. Berlin Heidelberg: Springer-Verlag, 2009. (Cited on page 27.)

[Waits 1978] R K. Waits. *Planar magnetron sputtering*. Journal of Vacuum Science and Technology, vol. 15, no. 2, pages 179 – 189, 1978. (Cited on page 37.)

[Walker 1995] S.A. Walker, P.A. Christensen, K.E. Shaw and G.M. Walker. *Photoelectrochemical oxidation of aqueous phenol using titanium dioxide aerogel*. Journal of Electroanalytical Chemistry, vol. 393, no. 1Ű2, pages 137 – 140, 1995. (Cited on page 34.)

[Wang 2006] J Wang. Analytical electrochemistry, 3rd edition. Wiley-VCH, New Jersey, 2006. (Cited on pages 50 and 52.)

[Weir 2012] A. Weir, P. Westerhoff, L. Fabricius and N. von Götz. *Titanium Dioxide Nanoparticles in Food and Personal Care Products*. Environmental Science and Technology, 2012. (Cited on page 29.)

[Williams 2009] D.B. Williams and C.B. Carter. Transmission electron microscopy. second edition. Springer Science+Bussiness Media, 2009. (Cited on page 47.)

[Xiaoxuan 2010] L. Xiaoxuan, Z. Gaoling, W. Liqing, D. Gangfeng and H. Gaorong. *TiNx thin films for energy-saving application prepared by atmospheric pressure chemical vapor deposition*. Journal of Alloys and Compounds, vol. 502, no. 1, pages 195 – 198, 2010. (Cited on page 26.)

[Yue 2001] Li Yue and Hu Shuguang. *The microstructure of the interfacial transition zone between steel and cement paste*. Cement and Concrete Research, vol. 31, no. 3, pages 385 – 388, 2001. (Cited on page 60.)

[Yuste 2011] M. Yuste, R. Galindo Escobar, S. Carvalho, J.M. Albella and O. Sánchez. *Improving the visible transmittance of low-e titanium nitride based coatings for solar thermal applications*. Applied Surface Science, vol. 258, no. 5, pages 1784 – 1788, 2011. (Cited on page 26.)

[Zayed 1992] Abla M Zayed. *Nature of the concrete-steel rebar interface in plain and silica fume [SF] concrete*. Materials Research Society Symposium Proceedings, vol. 245, pages 341 – 347, 1992. (Cited on page 66.)

[Zelic 2002] J. Zelic, D. Ru?ic and R. Krstulovic. *Kinetic Analysis of Thermal Decomposition of $Ca(OH)_2$ Formed During Hydration of Commercial Portland Cement by DSC*. Journal of Thermal Analysis and Calorimetry, vol. 67, pages 613–622, 2002. (Cited on page 62.)

[Zhang 2008] Jing Zhang, Qian Xu, Zhaochi Feng, Meijun Li and Can Li. *Importance of the Relationship between Surface Phases and Photocatalytic Activity of TiO2*. Angewandte Chemie International Edition, vol. 47, no. 9, pages 1766–1769, 2008. (Cited on page 100.)